HIGH RESOLUTION TIMING AND STYLE OF COSEISMIC DEFORMATION: PALEOSEISMIC STUDIES ON THE NORTHERN AND SOUTHERN SAN ANDREAS FAULT

by

ASHLEY REBECCA STREIG

A DISSERTATION

Presented to the Department of Geological Sciences
and the Graduate School of the University of Oregon
in partial fulfillment of the requirements
for the degree of
Doctor of Philosophy

June 2014

DISSERTATION APPROVAL PAGE

Student: Ashley Rebecca Streig

Title: High Resolution Timing and Style of Coseismic Deformation: Paleoseismic Studies on the Northern and Southern San Andreas Fault

This dissertation has been accepted and approved in partial fulfillment of the requirements for the Doctor of Philosophy degree in the Department of Geological Sciences by:

Ray J. Weldon, II	Chairperson
David A. Schmidt	Core Member
Joshua J. Roering	Core Member
Daniel G. Gavin	Institutional Representative

and

Kimberly Andrews Espy	Vice President for Research and Innovation; Dean of the Graduate School

Original approval signatures are on file with the University of Oregon Graduate School.

Degree awarded June 2014

DISSERTATION ABSTRACT

Ashley Rebecca Streig

Doctor of Philosophy

Department of Geological Sciences

June 2014

Title: High Resolution Timing and Style of Coseismic Deformation: Paleoseismic Studies on the Northern and Southern San Andreas Fault

Critical inputs to evaluate fault behavior models include the frequency of large earthquakes on plate boundary faults, amount of displacement, style of deformation in these events, and how these earthquakes are associated with adjacent sites and broader segments. Paleoseismic data provide these inputs and allow the characterization of hazard posed by individual faults. This dissertation presents results from paleoseismic studies at Hazel Dell and Frazier Mountain that provide new earthquake chronologies and slip estimates for the San Andreas Fault (SAF). These data provide new insights into the recurrence and style of coseismic deformation for surface rupturing earthquakes on the SAF.

The Hazel Dell site provides the first definitive paleoseismic evidence of two pre-1906, 19th century earthquakes on the Santa Cruz Mountains section of the SAF. I correlate these paleoseismic findings with the historic record of ground shaking associated with earthquakes in that period and combine the style of deformation in the last 3 events at the site with results from nearby paleoseismic sites to estimate earthquake rupture lengths and magnitudes for these early historic events. These findings increase the frequency of historic surface rupturing earthquakes on the northern SAF three-fold.

At the Frazier Mountain site, on the southern SAF, I mapped deformation across a releasing step on the fault for the last five surface rupturing earthquakes to estimate deformation per-event. I compare the geometry and amount of vertical relief generated across the step-over by retrodeforming 3D surfaces interpolated from paleoseismic data step-wise for stratigraphic units deformed by each of those earthquakes. I find that structural relief is similar in four of the last five events, so slip on the fault must be within the same range for these earthquakes to generate approximately equivalent structural relief across the step-over. These results suggest displacement on the fault is comparable at the Frazier Mountain site for the last 4 events, including deformation resulting from 4-5 m lateral displacements in the historic M 7.9 1857 earthquake.

This dissertation includes previously published and unpublished coauthored material. Supplemental file Plate A includes additional trench logs for the Hazel Dell site, presented in Chapters II and III.

CURRICULUM VITAE

NAME OF AUTHOR: Ashley Rebecca Streig

GRADUATE AND UNDERGRADUATE SCHOOLS ATTENDED:

University of Oregon, Eugene
Central Washington University, Ellensburg
Occidental College, Eagle Rock, California

DEGREES AWARDED:

Doctor of Philosophy, Geological Sciences, 2014, University of Oregon
Master of Science, Geological Sciences, 2003, Central Washington University
Bachelor of Arts, Geological Sciences, 2000, Occidental College

AREAS OF SPECIAL INTEREST:

Active Tectonics

Paleoseismology

PROFESSIONAL EXPERIENCE:

Graduate Research Assistant, University of Oregon, 2009-2014

Graduate Teaching Fellow, University of Oregon, 2009-2014

Project Geologist, Fugro William Lettis & Associates, 2006-2009

Senior Staff Geologist, William Lettis & Associates, Inc., 2002-2004

Graduate Research Assistant, Central Washington University, 2001-2002

Teaching Assistant, Central Washington University, 2000-2001

GRANTS, AWARDS, AND HONORS:

National Science Foundation Earth Sciences Postdoctoral Fellow, National Science Foundation, 2014

Johnston Scholarship in Geophysics and Structural Geology, Department of Geological Sciences, University of Oregon, 2014

Smith Scholarship, Department of Geological Sciences, University of Oregon, 2014

Johnston Scholarship in Geophysics and Structural Geology, Department of Geological Sciences, University of Oregon, 2012

Graduate Student Research Grant, Geological Society of America, 2010

Outstanding Student Paper Award, American Geophysical Union, 2002

Summer Graduate Research Fellowship, National Science Foundation, 2002

PUBLICATIONS:

Streig, A.R., Dawson, T.E., and Weldon, R.J., 2014, Paleoseismic Evidence of the 1890 and 1838 Earthquakes on the Santa Cruz Mountains Section of the San Andreas Fault, near Corralitos, California, Bulletin of the Seismological Society of America, v. 104, p. 285-300, doi: 10.1785/0120130009

Scharer, K.M., Fumal, T.E., Weldon, R.J., **Streig, A.R.**, 2014, Photomosaics and event evidence from the Frazier Mountain paleoseismic site, Trench 1, Cuts 1–4, San Andreas Fault Zone, Southern California (2007-2009), U.S. Geological Survey Open-File Report 2014-1002, 4 sheets, various scales, pamphlet 23 p., http://pubs.usgs.gov/of/2014/1002/.

Weldon, R.J., Dawson, T.E., Biasi, G., Madden, C., and **A.R. Streig**, 2013, Appendix G, Paleoseismic Sites Recurrence Database, in Uniform California earthquake rupture forecast, version 3 (UCERF3)—The time-independent model: U.S. Geological Survey Open-File Report 2013–1165, 97 p., http://pubs.usgs.gov/of/2013/1165/.

Streig, A.R., Rubin, C. M., Chen, W., Chen, Y., Lee, L., Thompson, S. C., Madden, C., and Lu, S., 2007, Evidence for prehistoric coseismic folding along the Tsaotun segment of the Chelungpu fault near Nan-Tou, Taiwan, Journal of Geophysical Research, 112, B03S06, doi:10.1029/2006JB004493.

Kelson, K., **Streig, A.R.**, Koehler, R.D., and Kang, K.H., 2006, Timing of Late Holocene Paleoearthquakes on the Northern San Andreas Fault at the Fort Ross Orchard Site, Sonoma County, California, Bulletin of Seismological Society of America, v. 96, p. 1012-1028.

ACKNOWLEDGMENTS

I would like to thank my advisor Ray J. Weldon, II for being a great mentor, for teaching me to never turn away from a problem and to embrace controversy, for pushing me to become a better scientist, and for leading by example. I would like to thank Tim Dawson, a coauthor on the projects presented in this thesis, for being a great friend who's encouraged me every step of the way from graduate school application to defense. I'd like to thank Kate Scharer, a wonderful colleague and great field geologist, working with you has been a pleasure and your friendship has been invaluable.

I would like to thank my parents, Jan and Dave Streig, for always encouraging me, for being my sanity, and for providing a home-base to our field crew while working in Watsonville. Returning to school was a tough decision, and a difficult journey, I could not have done this without you. My sister, Courtney, helped me immensely in the field and was enthusiastic and encouraging every step of the way, you are my greatest critic and my best friend. My grandmother, Edie Stene, pushed me to stop talking about returning to school and to see the dream to fruition. I needed her not-so-subtle nudges, I miss them dearly and wonder every day what words of wisdom she would share to guide me in my next life adventures.

I could not have succeeded without the support and strength of an amazing network of friends who have helped me work through problems, have volunteered to help me in the field, and have critically reviewed my work. The work presented in this dissertation would not have been possible without; Lili Weldon, Courtney Streig, Chris Madden-Madugo, Danielle Verdugo-Madugo, Rachel Lippoldt, Nyle Weldon, Spencer

Kendall, Andy Jerrett, Adam Arce, Andy Lutz, Steve Thompson, Justin Pearce, Dave Trench, Darlene Ishigo, Daniel Mayeri, Dan Contreras, Michael Strane and my WLA family. I would like to thank officemates in the Weldon lab and friends; Sequoia Alba, Amberlee Darold, Sean Bemis, Reed Burgette, Gordon Seitz, Lauren Austin, James McNabb, Kristin Sweeny, Katie Paulson, and the UO DoGS graduate student cohort.

I have to thank the heart and soul of the department, Dennis Fletcher, Dave Stemple, Shari Douglas and Vicki Arbeiter, for being good friends and helping me navigate the inner workings of UO. I would like to acknowledge my committee, Joshua Roering, Daniel Gavin, David Schmidt and Marli Miller for supporting my work and providing insightful reviews and conversations as I progressed with my research. I would also like to thank Tom Guilderson at LLNL-CAMS for teaching and mentoring me as I learned ^{14}C pretreatment and age dating methodology.

I would like to thank David Dent for allowing us unrestricted access to his property, and for his enthusiastic interest and help with the project in Santa Cruz.

Significant funding for work presented in Chapters II and III was provided by the U.S. Geological Survey (USGS) National Earthquake Hazards Reduction Program (08-HQ-GR-0071, 08-HQ-GR-0072, G10AP00064, G10AP00065 and G13AP00054). A Geological Society of America Student Research Grant supported age-dating work at LLNL-CAMS. Funding for work presented in Chapter IV came from the National Science Foundation (0838294), Southern California Earthquake Center (Y80786), and the USGS National Earthquake Hazards Reduction Program (05HQGR0071, 09AP00012, and 11AP20123).

For my family.

TABLE OF CONTENTS

Chapter Page

Chapter Page

Chapter Page

LIST OF FIGURES

Figure Page

CHAPTER IV

CHAPTER V

Figure Page

APPENDIX B

APPENDIX D

APPENDIX F

APPENDIX H

LIST OF TABLES

Table Page

CHAPTER I

INTRODUCTION

Globally, large magnitude earthquakes pose great hazard to populations living on active plate margins. The timing and frequency of prehistoric earthquakes are important inputs to seismic hazard models. To characterize the hazard posed by individual faults geologist seek to characterize fault slip rates, rupture frequency, timing of the most recent event and rupture length. With this information we can build and improve seismic hazard models like those in California (Uniform California Earthquake Rupture Forecast). The frequency of surface rupture on a fault can span anywhere from a few decades to thousands of years. Paleoseismology and tectonic geomorphologic studies are the only tools in our arsenal that give us insight into the rupture behavior of a fault for this portion of the geologic record; the last several decades to thousands of years past. In this dissertation I present results from two paleoseismic studies on the San Andreas Fault (SAF). This work refines earthquake recurrence in the last 650 years, and finds the first definitive evidence of two large earthquakes in the late 1800's within 68 years of the great 1906 earthquake on the Santa Cruz Mountains section of the northern SAF. I present both a careful review of historical documents and past work and employ new measures to achieve such high age-dating resolution for these historic earthquakes. On the southern SAF, near Lebec, CA, I explore new 3D techniques to evaluate both vertical deformation and lateral slip in an earthquake across a releasing step on the SAF. I provide a brief summary of my dissertation chapters below.

Chapter II was co-authored with Timothy E. Dawson (California Geological Survey) and my advisor Ray J. Weldon, II, and was published in the Bulletin of the Seismological Society of America, volume 104 in February 2014.

Paleoseismic investigations at the Hazel Dell site on the Santa Cruz Mountains section of the San Andreas Fault (SAF) provide the first definitive geologic evidence of two pre-1906 19th century earthquakes based on the presence of anthropogenic artifacts at the ante-penultimate earthquake (E3) horizon. I review historic accounts of candidate events and interpret the penultimate earthquake and E3 to be the April 1890 and June 1838 earthquakes. These new data suggest more frequent surface-rupturing earthquakes within historical time than previously recognized, and highlight variability of interseismic intervals on the Santa Cruz Mountain section of the SAF.

I correlate earthquakes between Hazel Dell and nearby paleoseismic sites based on revised timing, similarity of stratigraphy, style and size of displacement, and build a composite paleoseismic record. The composite record requires at least two modes of behavior in strain release on the Santa Cruz Mountains section through time. One mode is through great multi-segment earthquakes, like 1906. Historic records and geologic studies suggest that prior to 1906 the Santa Cruz Mountains region was characterized by a second mode of moderate seismicity, with three $M \geq 6$ earthquakes between 1838 and 1890, including two that caused surface rupture at Hazel Dell. In the 700 years before 1800 individual sites have evidence ranging from 1-5 events, suggesting that the longer record remains unresolved.

Chapter III was co-authored with Ray J., Weldon, II, Timothy Dawson (California Geological Survey), Daniel G. Gavin (University of Oregon) and Tom Guilderson

(Lawrence Livermore National Laboratories), this article is prepared for submission to the journal Geology.

This investigation carefully evaluates age dating techniques used in Chapter II, and improves earthquake age models with new ^{14}C age dating results. Paleoseismic studies aim to determine the age and size of surface rupturing earthquakes for the past several thousand years to characterize the spatial and temporal behavior of fault rupture. Robust earthquake chronologies are critical to evaluate the frequency of surface rupturing earthquakes and to test fault behavior models. However, at these short time scales (~10^3 yrs), uncertainties on age estimates of earthquake timing can have a very large effect on the signal to noise ratio, and hamper our understanding of the earthquake cycle. As a result, minimizing uncertainty contributing to prehistoric earthquake age estimates is of utmost importance. In this chapter I apply high-precision dating techniques (wiggle-matching) to push the limit on dating recent earthquakes on the SAF at Hazel Dell in the southern San Francisco Bay Area, CA. I demonstrate that 3 surface rupturing earthquakes occurred in the historic period since ~1800 (with less than a decade uncertainty). These findings increase the number of surface rupturing earthquakes on the SAF during early European settlement three-fold.

Chapter IV, was co-authored by my advisor Ray J. Weldon, II and Katherine M. Scharer (U.S. Geological Survey). In this chapter I use a 3D database of stratigraphic and structural data collected from paleoseismic trenches and Cone Penetrometer Tests to investigate the relationship between slip on a strike-slip fault and fold deformation across a releasing step-over.

Chapter IV presents the first attempt to combine earthquake chronology and slip per-event estimates by evaluating structural relationships across a step-over at the Frazier Mountain paleoseismic site on the SAF. Transtensive step-overs, known as sags, are ubiquitous features of strike slip faults. At the Frazier Mountain site, the main trace of the southern San Andreas Fault steps to the right 40 m over 150 m along strike. Within the step are two adjoining synclines ~30 m x 70 m and ~10 m x 40 m in size. 34 paleoseismic trenches and 35 cone penetrometer tests spanning the step-overs show stratigraphic and structural relationships that demonstrate incremental coseismic fold and fault deformation. Rapid sedimentation generally buries the sag produced in an earthquake flattening the ground surface before the subsequent event.

I quantify structural relief in individual ruptures across the step-overs using surveyed 3D point data for five key stratigraphic surfaces. 3D analysis suggests that three of four prehistoric events are similar in size to event FM1, the 1857 M 7.9 earthquake. Event FM4 is difficult to separate from the stratigraphic proximal FM5 but appears to be smaller than average. FM5 is slightly larger than other earthquakes, but is within typical along strike variability of displacement for surface rupture, or there is a previously unrecognized event between FM5 and 6 that is only recorded by folding in the investigation area excavated to date. Offset channels near the site suggest the 1857 earthquake (event FM1) generated ~5 m of lateral slip, and we document ~ 0.8 m of folding across the larger sag. We use the relationship between lateral slip on the fault and incremental sag deformation and find that 4 of the last 5 events produced ~ 4 – 5 m of lateral slip at the site.

CHAPTER II

PALEOSEISMIC EVIDENCE OF THE 1890 AND 1838 EARTHQUAKES ON THE SANTA CRUZ MOUNTAINS SECTION OF THE SAN ANDREAS FAULT, NEAR CORRALITOS, CALIFORNIA

This work was published in the Bulletin of the Seismological Society of America, volume 104, in February of 2014. Work presented in this chapter reflects findings from joint field efforts over the course of three years by me, Weldon and Dawson. I performed laboratory pretreatment for Accelerator Mass Spectrometry radiocarbon analysis for samples submitted to Lawrence Livermore National Laboratories and ran all age determination models. Dawson and I both compiled trench logs, I produced all other figures. I am the primary author of the manuscript, with editorial assistance from Ray Weldon and Tim Dawson.

Introduction

The Santa Cruz Mountains section (SAS) of the San Andreas fault is a 62-km long zone between Los Gatos and San Juan Bautista (WGCEP 1990, 2002, 2007), and is defined by a broad restraining bend through the Santa Cruz Mountains (Figure 1). This section of the fault is located between the locked Peninsula section to the north, and the creeping San Juan Bautista section to the south. The loading rate on the northern SJB is similar to that in Parkfield, but historically the creeping SJB has not experienced frequent

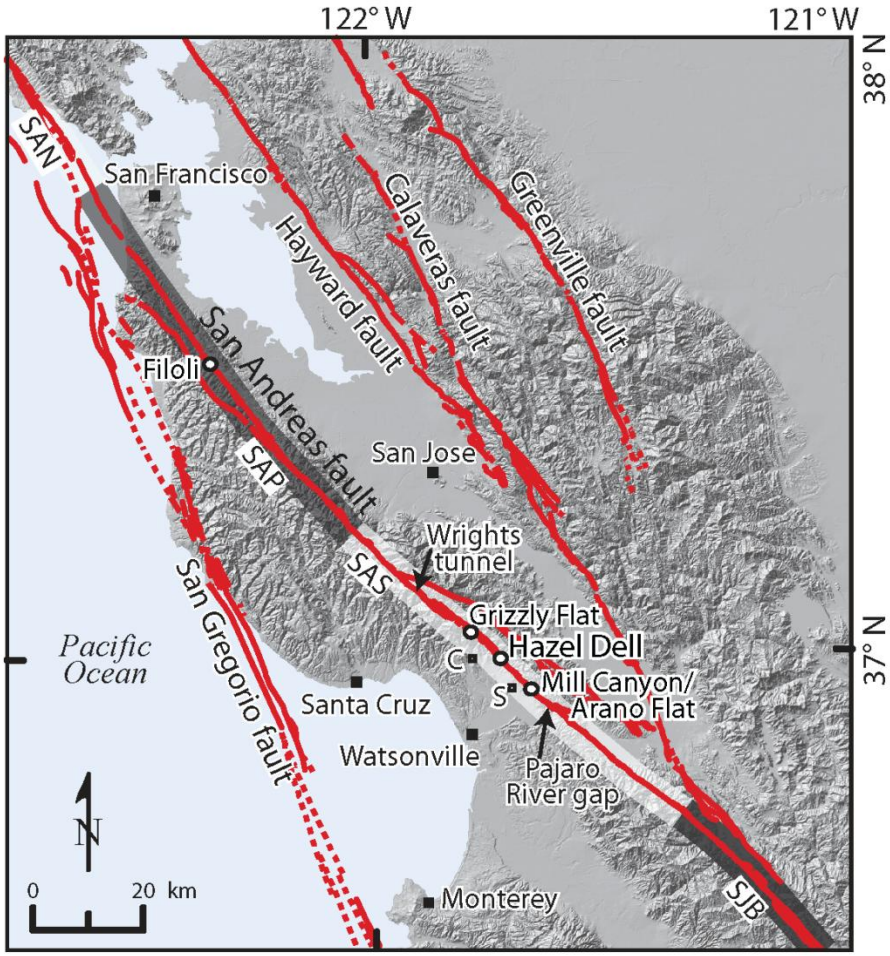

Figure 1. Location map of active faults in the San Francisco Bay Region showing the Santa Cruz Mountains section (SAS) relative to San Andreas Fault sections to the north and south. North Coast section (SAN), Peninsula section (SAP) and the creeping section (SJB) shown as alternating gray and white shaded sections along the San Andreas fault; other principal Bay Area faults are labeled accordingly. Faults are shown as bold lines. Open circles on the SAS are paleoseismic study sites, including Hazel Dell (this study). Solid black arrow shows where the Pajaro River crosses the SAS. Fault traces are from the Quaternary fault and fold database (see Data and Resources). Cities are shown as black squares, open black squares are present day: S - Salsipuedes, and C - Corralitos.

M 6 earthquakes, as Parkfield did in the 20th century (Johanson and Bürgmann, 2005). Johanson and Bürgmann (2005) find, based on the current distribution of creep, that the SJB section is accumulating a moment deficit at the rate of one M_w 6.3 to 6.7 earthquake per century, and propose that the SJB releases centuries of strain accumulation in clusters

of earthquakes spanning a few decades. It has been proposed that, like Parkfield, earthquakes initiate on the southern portion of the SAS and extend to the north, essentially acting as a transition zone between the locked Peninsula section to the north and creeping section to the south (Johanson and Bürgmann, 2005).

The SAS last experienced surface rupture during the M_w 7.9 1906 earthquake that produced about 470 km of rupture from Point Arena to San Juan Bautista (Lawson, 1908; Thatcher *et al*., 1997; Prentice *et al*., 1999). The reported paleoseismic recurrence interval for surface rupturing earthquakes ranges from ~125 years at the southern end of the SAS (Fumal, 2012) to 300+ years along the central portion of the SAS (Schwartz *et al.*, 1998). Schwartz *et al.* (1998) report that the Grizzly Flat site, on the central SAS, records 1906 and one 17th century earthquake. Two historic earthquakes were observed at Mill Canyon and Arano Flat sites on the southern SAS (Fumal, 2012; Fumal *et al*., 2003a, 2003b). We present a new paleoseismic record from Hazel Dell, located between these earlier studies, with evidence of four surface rupturing earthquakes. This study provides the first conclusive paleoseismic evidence for three historic earthquakes in the Santa Cruz Mountains, and provides slip and magnitude estimates for these historic events. We also re-evaluate event evidence for the Grizzly Flat, Mill Canyon and Arano Flat studies and conclude that all three sites experienced three earthquakes that occurred in the historic period, within a 70 year period of heightened seismic activity. The SAS has ruptured both with and independently of the Peninsula section to the north, and may be a transition zone with more frequent ruptures between the creeping section to the south and the Peninsula section to the north.

The Hazel Dell Site

The Hazel Dell site is located at the north end of a fault-bounded valley and sag pond, where a small ephemeral creek drains the basin; the San Andreas fault bounds the western edge of the valley and trends N30°W to N40°W (Figure 2). Locally, the fault juxtaposes sandstone and shale of the Pliocene and upper Miocene Purisma Formation on the west against Miocene to Oligocene Shale of Mt. Pajaro Formation on the east (Brabb, 1989). While, local fault traces were previously mapped at a scale of 1:24,000 (Quaternary fault database; Bryant *et al.*, 2002; Sarna-Wojcicki, *et al.*, 1975), we mapped small scale (<1m relief) fault features projecting to the investigation site on shaded relief, contour and slope maps generated from 0.5 meter resolution LiDAR data (Figure 2). The fault is geomorphically well expressed as well-defined linear breaks in slope along east-facing hillslopes bounding the valley, and aligned linear drainages and topographic escarpments north and south of the site (along Green Valley Road and Old Mt. Madonna Roads respectively, Figure 2). The 1906 rupture is interpreted to have occurred along

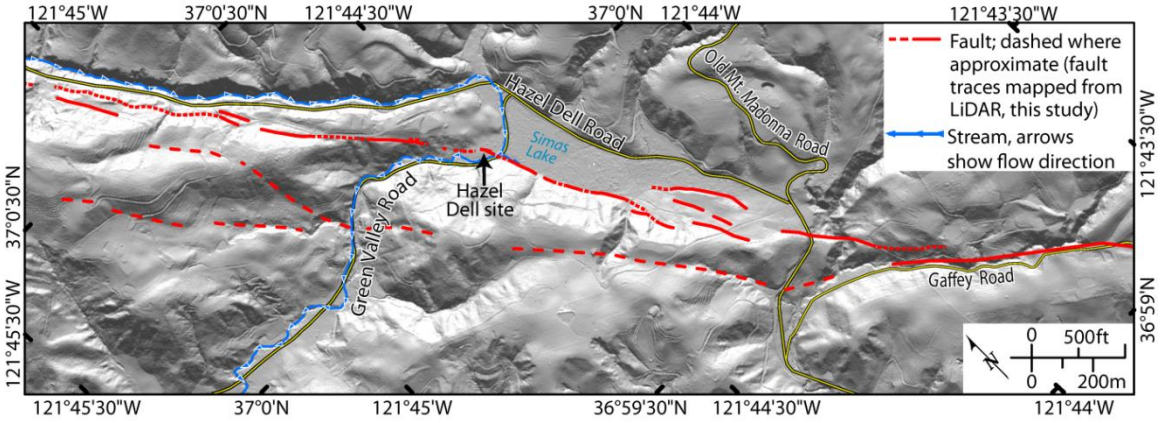

Figure 2. Detailed fault map of geomorphic lineaments in the Hazel Dell area (central SAS). Locally, the fault is expressed as a series of aligned drainages, linear range fronts, aligned topographic escarpments and a sharp base of slope along east-facing hillslopes. The Hazel Dell investigation site is located in the northwest corner of the fault-bounded valley, associated with a transtensive (right) bend in the fault zone. Basemap: shaded relief from bare earth GeoEarthScope 0.5 meter resolution LiDAR data (Prentice *et al.*, 2009).

the main trace of the San Andreas fault in this valley; however, at that time roads and bridges leading to this area were impassable, and the stretch between Grizzly Flat and Hazel Dell was not visited during the post earthquake investigation (Figure 1; Lawson, 1908; Prentice and Schwartz, 1991). Prentice & Schwartz (1991) reconstruct the route taken by G.A. Waring, who mapped this area (reported in Lawson, 1908), and find he returned to the main rupture trace just southeast of Hazel Dell along Gaffey Road (Figure 2). Roughly 24 miles northwest of Hazel Dell Prentice and Ponti (1997) estimate 1.7 - 1.8 m of 1906 surface slip at Wright's tunnel (Figure 1).

The Hazel Dell trench site is located within an area characterized by overbank deposits on the north side of Green Valley Road, is flanked by Green Valley Creek to the south and west, and hillslopes of Miocene to Oligocene sandstone bound the site to the north and east. Green Valley Creek crosses the fault at the southwest corner of the site (Figure 2). The Hazel Dell site is within the floodplain and has been inundated by flood waters in recent high rainfall years (personal communication, property owner, D. Dent, 2008). In these flood events the site was blanketed by fine-grained alluvial overbank deposits. The investigation site was an apple orchard between roughly 1950 and 1980 (personal communication property owner, D. Dent, 2008), and the ground surface was tilled, disturbing 20 to 50 cm below the ground surface as observed in trenches. These farming activities combined with historic overbank deposits obscure the surface expression of 1906 surface rupture across the site. In trench exposures, however, the 1906 rupture clearly offsets the youngest alluvial deposits above the penultimate earthquake horizon and extends to the tilled soil layer.

Methodology

We excavated a combination of slot and benched trenches across the site during summer and fall of 2008, 2010 and 2011 (Figure 3). Trench exposures were cleaned, gridded with a 1 m x 0.5 m string and nail grid, and photographed. All trench exposures were logged on a printed photo mosaic of high-resolution digital photographs at a scale of roughly 1:10. Stratigraphic units and structural relationships were documented and described on photo logs (see Appendix A and Plate A [supplemental file] for supplemental trench logs and unit descriptions). Both walls were documented in trenches that crossed the fault and in fault-parallel trenches adjacent to the fault. Only the north wall was documented in trenches 1, 2 and 6 that did not cross a fault trace and were located to span the site to explore for other possible fault traces. We collected detrital charcoal, wood chips, and block samples of key stratigraphic units for macrofossil analysis in the lab, and used all three sample types to constrain the ages of the deposits using ^{14}C dating. We surveyed trench outlines, faults, string grids and key stratigraphic units using a total station, and used a network of base stations and a differential GPS unit to tie together each survey and incorporate these data in an ArcGIS database (Figure 3).

Stratigraphy

Trenches across the site exposed mud-flow, and water-lain alluvial, slope-derived colluvial, fissure and scarp deposits. Coarse-grained gravel and medium to fine-grained alluvial stream deposits interfinger with colluvium proximal to bedrock hillslopes. Alluvial deposits were broken into nine major units, 100 to 900 (youngest to oldest) (Figure 4; see Appendix A for detailed unit descriptions).

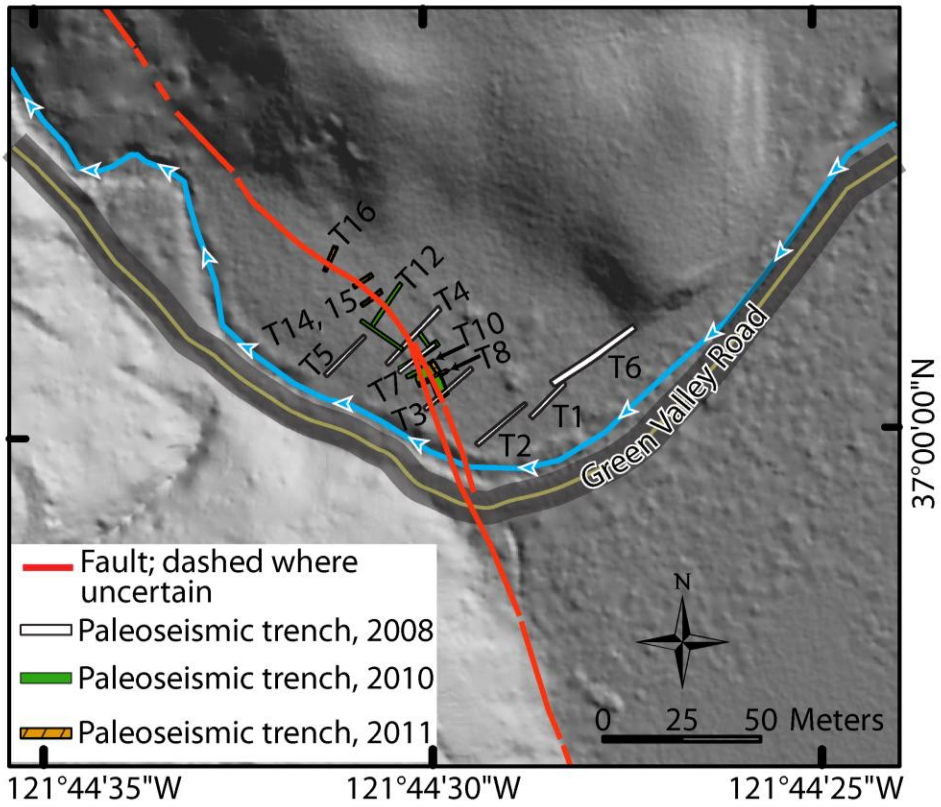

Figure 3. Hazel Dell site map showing the fault trace across the investigation site and the locations of 2008, 2010 and 2011 trenches. Note the bend in the fault across the trench site, from north to south the fault jogs to the right (east) near trenches T7, 8, 10 and 3, and jogs back to the left (west) in the northwestern portion of the site. The investigation site is located in a flood plain setting sourced by the creek flowing adjacent to Green Valley Road and Simas Lake to the south. Basemap: shaded relief compiled from GeoEarthScope 0.5 meter resolution LiDAR data.

The oldest stratigraphic unit, 900, is light gray silty clay, and is observed only in trench 4. Unit 700 is massive greenish gray clay and is the oldest and deepest unit correlated between trenches. Units 600 and 700 are only observed west of the fault, and are correlated between trenches that expose them (Figure 4). Unit 600 consists of silty clay and subunit 600a fines downward to 600b, silty sand. Unit 600a is discontinuous, eroded in places, and directly underlies the characteristic and widespread gravel unit 500. Unit 500b is a sandy gravel, with cobbles and is the deepest and oldest stratigraphic unit observed both east and west of the fault (Figures 4, 5), and unconformably overlies unit

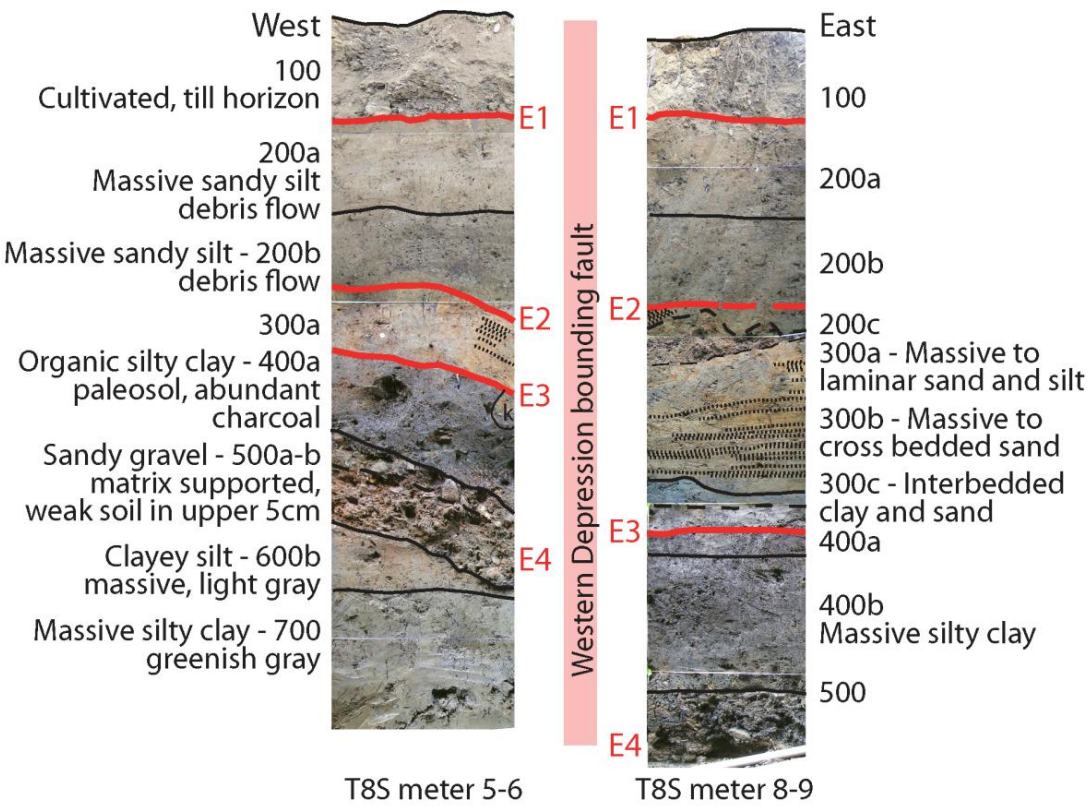

Figure 4. Stratigraphic columns, unit descriptions and correlations west of the depression bounding fault, and stratigraphy within the depression on a photo-mosiac base. The photo-mosaic is overlain with linework, black lines are unit contacts, shaded lines labeled E1 through E3 are earthquake horizons. Units 800 and 900 are not shown, these units are the deepest and oldest section and were only encountered in one trench, T4.

600 on the west side. Unit 500a is a sandy gravel and has a weak soil developed in the upper 10 cm of the deposit that overprints the matrix.

Unit 400 consists of massive clayey silt. Subunit 400a is a buried soil, that indicates a stable ground surface that led to soil development, and shows a period of marsh stability prior to deposition of the overlying sandy alluvial unit 300. 400a has abundant detrital charcoal and is defined by a distinct dark gray to black color that grades downward to medium gray of unit 400b (Figure 4). The dark color of unit 400a suggests that the unit was on the surface long enough to develop a significant organic A horizon. Units 300a, b and c are water-lain overbank deposits ranging from crossbedded sand and

silt to interbeds of fine sand, silt and layers of redwood needle hash. Subunit 300c consists of interbeds of very fine sand, silt and organic layers, with some angular axe-cut wood chips at the base of the unit. Trench T6 crossed the bedrock hillslope bounding the east side of the site and exposed unit 300f, a moderately coarse-grained slope-derived colluvium that interfingers with units 300a, b and c.

Unit 200 consists of light gray to grayish brown massive clayey silt with layers of sand to coarse sand and consists of subunits 200a-f. A depositional change from well-sorted laminated sands and interbedded silts, clays and organic layers of units 300a, 300b and 300c occurred before higher energy, coarse-grained, massive mud flow deposits of unit 200 was deposited. The uppermost unit, 100, is light grayish brown massive clayey silt, heavily bioturbated and represents agriculturally modified stratigraphy immediately below the ground surface including the till-zone and roots from former apple trees.

Earthquake Evidence

We find evidence of four earthquakes, and enough exposure to suggest that there is a complete record since the formation of a buried soil on unit 400a, recording the last three earthquakes (E1, E2 and E3). The exceptional stratigraphic resolution between events E1 and E3 is largely attributed to deformation caused by E3 that created a structural depression subsequently filled in with deposits, leading to a thickened stratigraphic section not seen elsewhere at the site. While the evidence for E4 is clear, the lack of stratigraphic section and the long time between E3 and E4 makes it impossible to rule out the possibility that "E4" combines evidence for more than one event. Or, alternatively it represents a longer earthquake recurrence interval in which a soil

developed. We compile earthquake evidence as trench logs and label event horizons E1 – E4 (Figure 5). Details on the location and quality of each observation of event evidence are summarized in Table A1 in Appendix A (following the methodologies outlined by Scharer *et al.*, 2007).

Event E1 – 1906

Evidence for the most recent event, E1, the 1906 rupture, is expressed in trenches 7 and 8 as one to two fault strands that extend upward to the base of unit 100, and also terminate within unit 200a the upper mudflow unit. Units 200b and 300a are vertically displaced across the E1 fault (Figure 5; for additional earthquake evidence see Appendix A and Plate A). Vertical separation of unit 300a across these strands range from 25 to 50 cm across the 1906 trace (Figure 5).

Event E2

The penultimate earthquake places unit 200c and 200d in vertical fault contact with unit 300a and b; this relationship was exposed in multiple cuts of trench 10 (Figure 5, 6, Appendix A, Plate A). E2 fault traces do not extend upward into 200a, and do not clearly extend up into 200b. Unit 200b has no vertical separation or change in thickness across the projected E2 fault traces, while unit 200c and 200d are truncated by the fault and placed in vertical contact against unit 300b (Figure 5b). This event generated 26 cm of vertical separation of a gravel lens within unit 300b across the eastern trace, and completely truncates units 200d and 200c; overlying units are continuous across the fault, and are unfaulted. This earthquake occurred sometime after the depression formed by E3

was filled with units 300, 200d and 200c (see below), and probably happened while 200c was at the ground surface, as shown in the cartoon reconstruction (Figure 6). After E2, this horizon was probably modified by the high energy deposition of 200b, a mud flow, making upward terminations unclear. Evidence of E2 was clearest in trench T10-A, and in subsequent T10 cuts D, E, F and G (cut incrementally 10 to 20 cm northward into the wall; Appendix A, Plate A). Cuts T10-B and C were excavated in 2010 and were small hand dug trenches to the south of T10-A.

Event E3

Earthquake E3 occurred when the top of unit 400a was the ground surface. Axe-cut wood chips are incorporated in the upper few centimeters of unit 400a and at the base of the overlying sequence 300c. E3 formed a roughly 7 meter long and 1.5 meter wide, 1.5 meter deep oblong structural depression, or fissure (Figure 5). The depression extends between trenches 7 and 8. At the north end, in trench 7, the depression is 20 cm deep. At its center in trench 10 the depression is as much as 1.6 meters deep (Figure 5), and decreases to 20 centimeters of down on the east relief to the south in trench 8 (Figure 5). The E3 depression is in-filled by stratigraphic units 200b and c and 300. In Trench 8 the depression formed by E3 is associated with folding of unit 400, with units 300b and 300c deposited as an on-lap sequence against the fold scarp (Figure 5a; Appendix A, Plate A). Unit 300c in-fills a depression formed on the unit 400a surface. 300c is 20 – 25 cm thick in trenches T7 and T8, and thickens substantially within the depression;

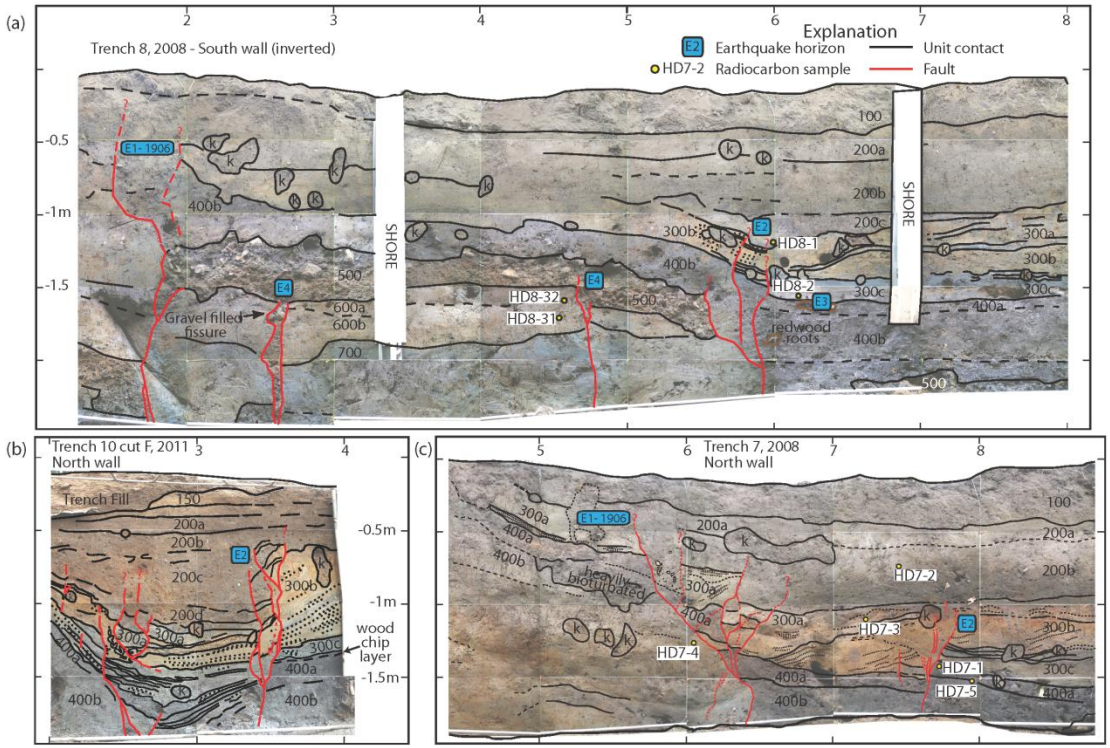

Figure 5. Portions of photomosaiced trench logs for Hazel Dell trenches T8, T7 and T10F. Stratigraphic units are labeled with numbers; radiocarbon samples are shown as open dots. Faults are shown as bold sub-vertical shaded lines. K symbols are krotovina (burrows). (a) Portion of Trench 8 - 2008 log, south wall (reversed). (b) Trench 10 - 2011, cut F photo-mosaic log. (c) Portion of Trench 7 - 2008 log, north wall. Evidence for the most recent event, E1, the 1906 rupture is expressed in trenches 7 and 8 (c and a) as one to two fault strands that extend upward toward the basal contact of unit 100. The penultimate event, E2 places unit 200b in vertical fault contact with unit 300b in trench T10 (b), this relationship was exposed in multiple cuts into the original wall of trench 10. Event E3 occurred while unit 400a was at the ground surface and formed the depression in T10-2011, and smaller east down displacements of the 400a surface in T8 and T7. Event E4 is expressed as upward fault terminations within the oldest gravel unit 500, and as fissures which incorporated gravels from unit 500, and was observed in trench T8. Refer to Appendix A and Plate A for additional trench logs and evidence.

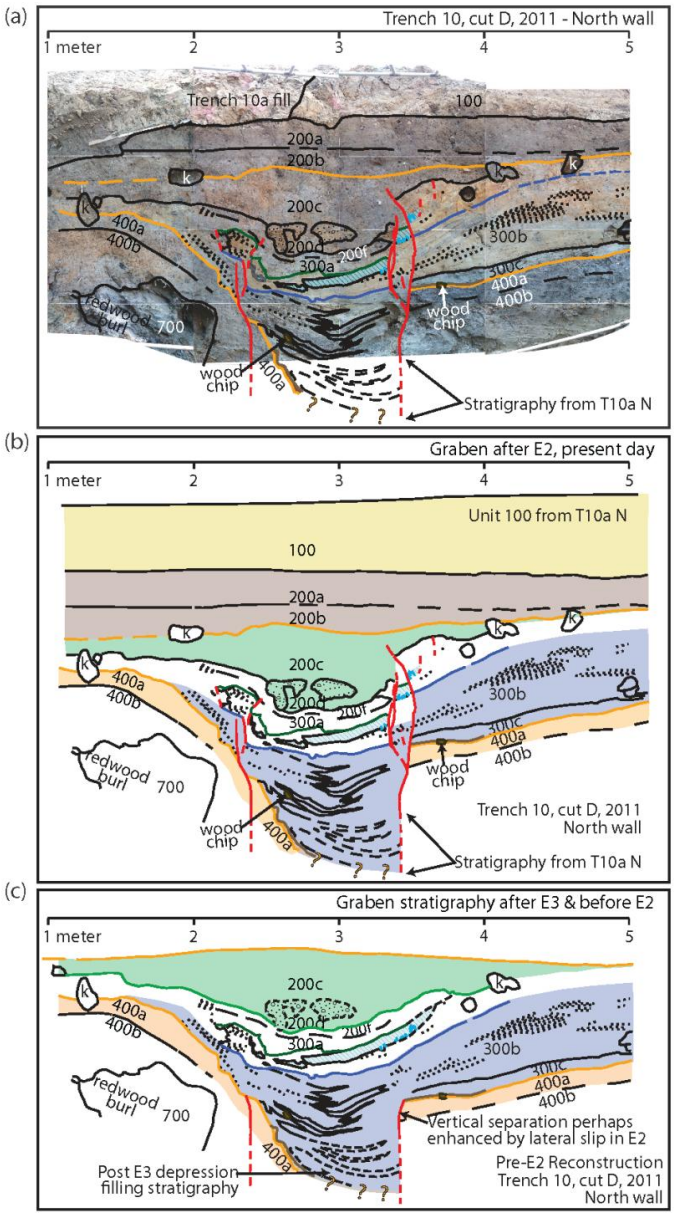

Figure 6. Trench T10 log showing evidence of events E2, E3, and schematic reconstruction of E2 deformation highlighting the magnitude of E3 deformation. (a) Photo-mosaic log of T10 – 2011, cut D, overlain with linework, bold sub-vertical shaded lines are faults, black and all other sub-horizontal lines are unit horizons. (b) Simplified linework for T10 – 2011 cut D, showing E2 and E3 deformation. E2 completely truncates 200 d and c, overlying units are continuous across the fault, and are unfaulted. We add the deeper depression-filling stratigraphy logged in the previous cut, T10a-2010. (c) Schematic reconstruction of E2, showing the E3 depression prior to the E2 event. The hatch-mark lenticular polygon is a gravel lens within unit 300b (shown as a faulted polygon in (a) and (b)) has over 26 cm vertical separation across the eastern trace. E2 deformation is removed by reconstructing the shaded polygon shown in (a) and (b) and reconstructed in (c). Vertical separation of unit 400a across the eastern depression-bounding-fault is enhanced by lateral slip in E2.

at its thickest it is 70 cm in T10-A. Unit thickness decreases in subsequent cuts northward to 50 cm in cut T10-F (Figure 5). Additional evidence for E3 includes a small fissure filled with sediment derived from unit 400 in trench T7.

Event E4

Evidence for the oldest event (or possibly events; in either case we refer to all evidence at this horizon as E4) was identified in trenches T8 and T4. E4 is expressed as upward fault terminations within the oldest gravel unit 500b, and as upward terminating fissures which incorporated gravels from the overlying unit, 500b, in the fissure fill. Gravel filled fissures were observed in trench T8 near meters 2, 3 and 4.5 (Figure 5c; Appendix A, Plate A). Event E4 occurred after deposition of the gravel, unit 500b and before a soil formed in the upper 10 to 20 cm of the gravel unit 500a. The soil is not displaced, and does not change in thickness or follow vertical separations of the lower part of the unit, 500b, but is instead continuous across the fissures. Because the soil is continuous and not warped downward into the fissures, the E4 earthquake(s) probably occurred before the soil formed, or early in its development (Figure 5a).

Deposit Age Estimates

Age constraints at the site are provided by historical artifacts and an abundance of organic material, including redwood needles, redwood cone fragments, wood, and detrital charcoal. These materials were sampled from key stratigraphic units and used for accelerator mass spectrometry (AMS) ^{14}C age determination. Wood, needles and some charcoal samples were analyzed at the Center for Accelerator Mass Spectrometry

(CAMS) at Lawrence Livermore National Laboratory (LLNL). Detrital charcoal samples collected in the first year of the study (2008) were submitted to Beta Analytic Inc., Florida. Each sample was pretreated with acid-alkali-acid washes and results are reported as conventional radiocarbon ages (years B.P.) in the Appendix. We use these and other data to build an age model and estimate age distributions for the earthquakes using OxCal v. 4.1.7 (Data and Resources; Bronk Ramsey, 2009), discussed below.

The fourth earthquake (E4) is relatively poorly constrained, in part, because the radiocarbon dating for this event relies on charcoal samples largely derived from redwood trees, which are long lived and also have a long residence time in the environment, leading to larger contextual dating uncertainties. This is an issue endemic to the Santa Cruz Mountains, as it is heavily forested and successful dating of earthquakes relies on large numbers of radiocarbon samples in order to constrain the range of ages within a deposit (Fumal, 2012; Fumal *et al.*, 2003b).

Historical woodchips, and historical accounts of settlement in the area provide additional age constraints that are not possible using radiocarbon dating alone. Embedded into and at the top of unit 400a, we found hundreds of pieces of cut wood, ranging from small pieces a few centimeters long to >30 centimeters long. Ends of the wood chips are characterized by smooth, angled cuts transverse to the wood grain (Figure 7), indicating they were cut by a sharp metal tool, likely an axe. On one piece (Figure 7b), the cut shows where the edge of the tool was embedded, in the form of a narrow, sharp incision in the wood, indicating the sharpness of the tool used to make the cut, consistent with the taper of an iron or steel blade. Some pieces also have remnants of bark on the outer perimeter. Given the preserved sharpness of the cuts, we hypothesize that 1) The

woodchips were not transported very far, otherwise the sharp edges would be degraded from transport, and 2) They were embedded into the top of unit 400a very soon (within a few years, and probably less) after they were cut, otherwise the cut edges would also be degraded from weathering and decay, particularly the smaller sharply angular pieces. The extent of the woodchips residing at the 300/400 interface appears limited to the area of T10, within the localized depression created by E3. Woodchips were also found in unit 300; most abundantly near the base of 300c, with fewer and smaller woodchips found stratigraphically higher in the upper part of 300c, and none found in 300b or above. Given the location, it appears the woodchips were on the ground when unit 400a was at the surface, and subsequently buried as well as incorporated into the lower part of unit 300. If these chips were deposited at the same time as unit 300c, then we might expect to see the wood chips more uniformly distributed throughout the deposit, and not concentrated at the 300/400 contact. A cut and burnt redwood burl rooted in unit 400 was exposed in T10 within a couple of meters of the wood chips (Figure 6a), and although it is somewhat speculative that the chips came from the cutting of that redwood tree, it does show that redwood trees were very near where we found the redwood chips, and other cut redwood stumps were found in other trenches. Given that the woodchips were embedded in the top of unit 400a, and below the post-E3 fill sequence, the wood chips were deposited before E3. It is possible the wood chips were cut after E3, and deposited on the ground surface immediately after the earthquake before the E3-generated depression was filled by unit 300. However, the time between E3 and the filling of the depression appears short given the rapid filling of the E3 depression with interbedded sands and organic-debris. There is no indication that the depression persisted

at the surface long enough to either, accumulate *in situ* organic material, or become significantly degraded or eroded, evidenced by the steeper western side of the depression (Figure 5, 6).

Figure 7. Examples of wood chips collected from unit 400a. (a) Larger sample, 10 cm wide by 20 cm long. Transverse cut across wood grain. (b) Smaller wood chip with very fine ~1 to 2 mm wide cuts at opposing angles suggests narrow bladed steel axe. (c) Wood chip with bark, 180 growth rings, inner and outer rings were sampled and used in 14C analysis, sample HD-2011-WC1 samples A (inner ring) and B (outer ring). (d) Wood chip with bark, 24 growth rings, inner and outer rings were sampled and used in 14C analysis, sample HD-2011-WC2 samples A (inner ring) and B (outer ring).

There are no known ethnographic or historical accounts of pre-contact native people chopping down large trees in the way that European colonists would have. Local indigenous populations didn't make large hafted axes needed to cut large trees (Anderson, 2005; Lightfoot *et al*., 2009). In 1769 the Portola expedition crossed what later became Rancho de Los Corralitos, and provides the first written record of the size and abundance of redwood trees in the area. The Portola expedition observed that many of the redwood

trees measured from 3.4 to 4 meters in diameter (Pybrum-Malmin, 1998). We exposed shallowly buried redwood stumps at the intersection of trenches T1-T2, and T1-T6 that were 1.75 m wide and were chopped off. Between 1803 and 1807 the Branciforte Villenos unsuccessfully attempted to settle the Corralitos area and by 1807 the Presidio at Monterey pastured 500 cattle and horses in the Salsipuedes and Corralitos Ranchos (Figure 1; Pybrum-Malmin, 1998). The Hazel Dell site is within the original Spanish land grant to Don Jose Amesti, granted in 1827 (Pybrum-Malmin, 1998). Large scale redwood lumber harvest began in this area sometime around or before 1832, "Amesti is said to have had a whipsaw lumber mill in 1832 on the upper Corralitos." (Pybrum-Malmin in Data and Resources). Amesti was making and selling shingles in the Corralitos canyon area in 1832 – 1836 (Ellison and Price, 1953). These early records of local redwood harvesting, combined with the knowledge that local native populations did not chop down large trees indicates that unit 400 was at the surface at the time of European settlement, and earthquakes E2 and E3 post date European settlement, and are historical.

To confirm this age range we sampled growth rings on two of the wood chips, and obtained AMS ^{14}C radiocarbon ages. These wood chips were selected based on the presence of preserved bark on the sample, meaning that we were able to sample the outer rings, as well as sample the inner-most ring preserved on the sample, providing a growth period of 180 years for sample HD-2011-WC-1 and 24 years for sample HD-2011-WC-2. The radiocarbon dates were "wiggle matched" with the intercepts for the radiocarbon age and error with the known interval between growth rings on the INTCAL04 terrestrial ^{14}C calibration curve (Reimer *et al.*, 2004). A Bayesian approach combining the ^{14}C dates

with the relative age between samples (years determined by counting the number of growth rings) was employed to wiggle-match the results using OxCal v.4.1.7 (Bronk Ramsey *et al*., 2001; see also Data and Resources). Using their wiggle-matching technique OxCal yields a 2σ modeled outer growth ring/chopping age range between 1698 and 1850 for sample HD_2011_WC1 (Appendix B for full results and sample HD_2011_WC2). Based on this modeled age range and the historical record, the death of the woodchips could have occurred as early as 1803, the earliest possible date from the historic record of land use once the region was inhabited by the Spanish to 1850, the youngest possible age for the woodchips. We infer a chopping date around 1827 most likely, when the property became a Spanish land grant and soon after which redwood logging is documented to have begun in the upper Corralitos area (Pybrum-Malmin, 1998; see also Data and Resources). We use these values, 1827 + 23/-24 years, in our OxCal age model (Figure 8).

We used OxCal v. 4.1.7 (Data and Resources; Bronk Ramsey, 2009) to construct a calibrated age model for earthquakes identified at Hazel Dell, and included boxcar dates for historic information, such as the 1906 San Francisco earthquake, and an age range of 1827 +23/-24 years as a constraint on the timing of the chopping of the tree and wood chips at the contact between units 300c and 400a. Calibrated probability distribution functions for the remaining samples are shown in stratigraphic order in Figure 8, along with estimated probability distribution functions for the timing of the four earthquake horizons identified at the site.

We have exceptional stratigraphy in the period of time since the redwood chips were deposited to the early 19th century. However, we recognize that we may be missing

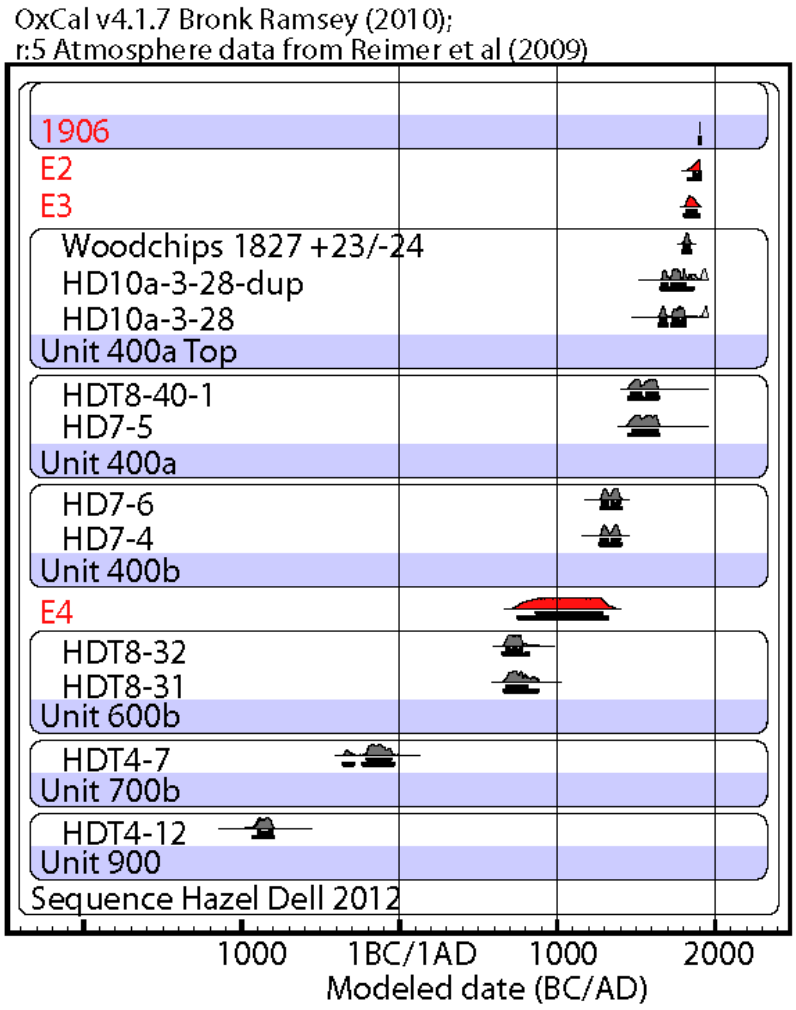

Figure 8. OxCal model of stratigraphic ages constraining the timing of earthquake horizons at the Hazel Dell site. Prior Probability distribution functions (pdf's) for radiocarbon samples shown in light gray, posterior pdf's shown in dark gray. Unit numbers shown on the shaded bars. Modeled earthquake ages are labeled by event name. Note – inconsistent samples removed, see Appendix C for complete list of samples.

events in what appears to be a depositional hiatus between E3 and E4. Unit 400a is a mature buried soil, which had old growth redwood trees rooted in it at the site. Based on the soil development and the size of stumps seen in other exposures at the site, this was a long-lived surface, likely spanning hundreds of years. Other events could have occurred in the time after deposition of unit 500 gravel and earthquake E4, but before the soil developed on unit 400a had formed. Our trenches exposed the top of the gravel unit in the

E3 depression, but the water table prevented us from safely exposing the base of the gravel in this area, and looking for additional evidence of events prior to E3. We infer much older material west of the fault, in T4 and T7, unit 700 yielded a modeled age of B.C. 40 – 350, and unit 900 ranged from B.C. 800 – 900 (see Appendix C).

Event Ages and Correlation to Historical Earthquakes

We interpret E1, the most recent event at Hazel Dell, to be the 1906 rupture, based on historical accounts of the earthquake rupturing through the Santa Cruz Mountains to the vicinity of San Juan Bautista (Prentice and Schwartz, 1991). Based on the historical constraints from the cut wood chips, we have two additional historical earthquakes that occurred in the 19th century and with these constraints, the OxCal modeled age for E2 is 1840 to 1906 (2σ uncertainty, Figure 8), and the OxCal modeled age for E3 is between A.D. 1815 and 1895. E4, our oldest paleoearthquake is prehistoric with a modeled age with 2σ uncertainties between A.D. 760 – 1318. In this section, we examine the historical record of moderate to large earthquakes in the Santa Cruz Mountains in order to correlate historical earthquakes to events E2 and E3 observed in the trenches at Hazel Dell.

Historical records indicate three local M > 6 earthquakes in this time period; the earliest a June 1838 event which had high intensities extending from the Peninsula to the Santa Cruz and Monterey Bay region and is interpreted to have ruptured part of the Peninsula and a portion of the Santa Cruz Mountains section of the San Andreas fault (Bakun, 1999; Hall *et al.*, 1999; Toppozada and Borchardt, 1998; Toppozada *et al.*, 2002). An 8 October 1865 earthquake caused ground cracking in the Santa Cruz Mountains

(Bakun, 1999), and a 24 April 1890 earthquake in the Pajaro region that caused significant damage, from Corralitos south to San Juan Bautista and cracking in places along the same trace as the 1906 rupture (Bakun, 1999; Tuttle and Sykes, 1992).

1838

The June 1838 M_w ~ 7.2 earthquake was the first major earthquake since the founding of Mission San Francisco Dolores in 1776 (Toppozada *et al.*, 2002; Tuttle and Sykes 1992). On the Peninsula section at Filoli (Figure 1), Hall *et al.* (1999) observe channel deposits offset 4.1 m (±0.5) and interpret this to be combined 1906 and 1838 displacements. They infer approximately 2.5 m (±0.2) displacement at their site in 1906 from an average of nearby offset measurements reported in Lawson (1908), and estimate that the difference, 1.6 m (±0.7), of the total measured displacement occurred in 1838. Hall *et al.* (1999) estimate that this displacement is consistent with an M_w 7.0 - 7.4 earthquake. Tuttle and Sykes (1992) estimated that the 1838 rupture extended about 100 km from San Francisco to Hughes Creek, roughly 3 km south of the Hazel Dell Site, and 5 km north of the Mill Canyon Site (Fumal, 2012), and estimated an M_w 7.2 earthquake based on this length and intensity data. Topozzada and Borchardt (1998) conclude that 1838 ruptured from near San Francisco to San Juan Bautista, a rupture length totaling ~140 km indicating a M_w ~7.4 earthquake, and also caused at least two notable large aftershocks in 1840 and 1841 (Topozzada and Borchardt, 1998; Toppozada *et al.*, 2002). Toppozada and Borchardt (1998) compile damage reports of the extent of faulting in this event as reported by Louderback (1947), and report strong intensities in Woodside where solid adobe houses were cracked severely, and redwoods were "broken off and hurled". We interpret this to be

the best candidate event for the earliest historic earthquake, E3, at the Hazel Dell site.

1865

The 8 October 1865 earthquake was most destructive in the Watsonville–Santa Cruz– San Jose area (Toppozada *et al.*, 2002). McNutt and Toppozada (1990) and Tuttle and Sykes (1992) found that the 1865 earthquake was smaller than the 1989 Loma Prieta earthquake, which occurred along a 70° southwest-dipping blind oblique reverse fault in the SAF zone (Wald *et al.*, 1991). Tuttle and Sykes (1992) reviewed felt reports for the 1865 event and found greater damage northeast of the SAF than in 1989, and concluded that the event occurred on a reverse fault northeast of the SAF and assigned the event M_w M ~6.5. This result is consistent with later analysis by Bakun (1999). Triangulation data collected between 1853 – 1860 and 1876 – 1891 record northeastward displacement of station Loma Prieta, which Yu and Segall (1996) conclude is a result of the 1865 earthquake. Yu and Segall (1996) find that the displacement is consistent with a M_w 6.75 thrust earthquake northeast of the San Andreas fault in the Santa Cruz Mountains thrust belt. Based on triangulation and intensity data that suggests this earthquake was northeast of the San Andreas fault, we find it unlikely that 1865 is a candidate for one of the historical earthquakes on the main trace of the San Andreas fault and observed in the paleoseismic record at Hazel Dell.

1890

The 24 April 1890 earthquake has an estimated M 6 by Toppozada *et al*. (1981) and M_w ~6.3 by Bakun (1999) and Tuttle and Sykes (1992). This event caused significant

damage at Corralitos, Green Valley, Pajaro, San Juan Bautista and Sargents (Bakun, 1999). Surface cracks observed in 1890 were located on the trace of the SAF where offset was observed in 1906, south of the Pajaro River (Lawson, 1908; Prentice and Schwartz, 1991; Bakun, 1999), and was felt as far away as Carson City, Nevada (Holden, 1892). Holden (1892) reports duplex seismograph readings from Mount Hamilton, Mills College and other Bay Area institutions for the 24 April 1890 earthquake. Holden also catalogues local reports of a series of earthquakes, or aftershocks, in the months following the April 1890 earthquake,

> Santa Cruz, May 14. – Ever since the big earthquake of 24th of April there have been seismic disturbances along the line between Pajaro and San Juan, where the earthquake was heaviest. Each day three or four small shocks occur, and yesterday six quite pronounced ones were felt… (Holden, 1892 pg. 17 of 31)

These earthquake and aftershock observations described by Holden suggest that the 24 April 1890 earthquake was substantial, and caused aftershocks on the main trace of the San Andreas fault. This suggests that the San Andreas is the source area for the main shock. We find that this is the best candidate historical earthquake for E2, given reports of possible rupture along the SAF, and the intensity reports which appear to be centered in the vicinity of the Hazel Dell site (e.g. Bakun, 1999).

Event Evidence from Nearby Paleoseismic Sites

We review event evidence and dating methods employed at Grizzly Flat, Arano

Flat and Mill Canyon paleoseismic sites. Mill Canyon and Arano Flat are located 1.5 km apart, and a hiatus in sediment accumulation is observed at both sites between 1906 and 1838 (Fumal 2012; Fumal *et al.*, 2003a, b). While the authors interpret no event in the intervening time, we point out that a hiatus in deposition occurred at the critical time to record the 1890 event. Although they do discuss the possibility that it may have occurred at their sites but was not distinguishable from the 1906 event. Lack of sedimentation does not preclude an earthquake between 1906 and 1838, but we review the assumptions made in these papers and argue that the authors missed the 1890 event.

Mill Canyon

Mill Canyon is located 8 km south of Hazel Dell. Fumal (2012) finds evidence of the 1906 earthquake rupture, and a penultimate earthquake that falls within the early to mid-19th century. Fumal (2012) found that the ground surface of the 1906 rupture was initially unclear with 12 separate exposures of the fault zone, and identified the 1906 ground surface using three-dimensional excavations. Fumal's unit 4 is the top of an organic rich layer that contains historic artifacts including weathered fence posts from a fence erected in 1854 by the property owner. The top of unit 4 was the ground surface throughout the second half of the 19th century. Little to no sediment was deposited at the Mill Canyon site in the intervening time between 1838 and 1906 (Fumal, 2012). Fine sands (his units 2 and 3) deposited soon after 1906 bury and preserve the fissures and scarps formed during the 1906 earthquake. Although Fumal (2012) did not identify evidence for the 1890 earthquake at Mill Canyon, because of the depositional hiatus during the nineteenth century, it is possible the earthquake is not stratigraphically distinguishable

from the 1906 earthquake. Lawson (1908) reports cracks that occurred along the fault in the same location in 1906 as the earthquake 16 years earlier (1890), south of the Pajaro River. If this was surface rupture related to 1890 that extended between Hazel Dell and past Mill Canyon, it is likely that paleoseismic evidence for 1890 would be indistinguishable from the 1906 earthquake.

Fumal (2012) presents two OxCal age models for timing of the penultimate (MC-2) at Mill Canyon. In Fumal's model 1 the lower age limit of key stratigraphic units were constrained by the lack of non-native pollen (Fumal, 2012). Based on our own experience at Hazel Dell, 8 km away, we have found that historic sediments lack the non-native pollen commonly associated with Spanish cattle migration, although invasion of these non-native plants is widely thought to precede Spanish settlement (Mensing and Byrne, 1998). The presence of non-native pollen is informative of the age of a deposit; however, the lack of pollen does not unambiguously represent the period prior to Spanish settlement. The lack of non-native pollen can represent poor pollen preservation in coarse-grained sediment, an ecological niche where these invasive species, such as *Erodium Cicutarium*, would not grow (i.e. a shady redwood grove is an unlikely environment for sun-loving *Erodium*), or that the sediments pre-date introduction of the non-native species to the area. The buried pollen samples should be compared with a modern environment analogous to the regional vegetation (Calcote, 1995). We prefer model 2 in Fumal (2012) because it does not use the lack of non-native pollen to constrain the timing of event MC-2 (Fumal, 2012).

Arano Flat

At the Arano Flat site 9.5 km south of Hazel Dell (Figure 1), and 1.5 km south of

Mill Canyon, Fumal *et al.* (2003a) report a partially-buried channel that contains bottles from 1870 - 1890 that is offset 3.5 m across the fault, and interpret this to be offset by one event, 1906. They state that the 3.5 meter displacement is unexpectedly high compared to the geodetic estimate of 2.3 - 3.1 m for the slip at depth (Thatcher *et al.*, 1997), or the geologic estimate of 1.7 - 1.8 m of surface slip at Wright's Tunnel (Prentice and Ponti, 1997), about 33 km northwest of Arano Flat. The bottles in the channel deposit were produced from 1870 to 1890, suggesting they could have been deposited prior to the 1890 earthquake (identified bottle: Dr. A. Boschee's German Syrup, L.M. Green proprietor, circa 1870's; Fumal *et al.*, 2003a). Given this, and the anonymously high 3.5 meter displacement of the channel containing the bottles, we propose that the 3.5 meter offset is the cumulative displacement from both 1890 and 1906 earthquakes. We argue that within the dating constraints provided by the bottles, one can't preclude that the channel was only offset in 1906, and that the 3.5 meter displacement could be the sum of 1890 and 1906 offsets, that are not distinguishable due to the lack of stratigraphy at this time.

The event, AF-2, identified by Fumal *et al.* (2003b) occurred while their unit 19, a very dark gray silty clay was at the ground surface. This unit has some organic soil development, suggesting it was a stable ground surface at the time of the earthquake. This event generated a roughly 1 meter wide, 1 meter deep fissure at the Arano Flat site (Figure 9). In Appendix D, we provide an OxCal model for Arano Flat using the accelerator mass spectrometry ^{14}C age determinations from detrital charcoal samples collected from their trenches and presented in a table in Fumal *et al.*, 2003b (see Appendix D, Table D1 and Figure D1). No model was included in their Open File Report (Fumal *et al.*, 2003b). Using their dates we find that AF-2 has a 2σ modeled age range of A.D. 1760 to 1861.

Given the beginning of the historical period at 1769 this was almost certainly a historical event.

Grizzly Flat

Schwartz *et al.* (1998) present evidence for 1906 and one earlier event at Grizzly Flat. Fumal (2012) reviewed trench logs for Grizzly Flat, reinterprets logs for possibly two additional earthquakes that post date the "penultimate" event identified by Schwartz *et al.* (1998). Fumal renumbers the events; GF-1 is 1906, GF-2* and GF-3* are added, and GF-4* is the "penultimate" event identified by Schwartz *et al.* (1998). Trench log evidence for GF-2* is the weakest with only one line of evidence; upward decreasing vertical separation of units 4a and 6c on the north wall of the north trench (Fumal, 2012). GF-3* occurred while their unit 6c was at the ground surface. Evidence of GF-3* includes upward fault terminations within unit 6c, and absence of the unit between two fault strands suggest lateral slip that is not reflected in overlying stratigraphy (Schwartz *et al.* 1998; Fumal, 2012).

Fumal also addresses two possible problems with age constraints for GF-4* used in the original model. Schwartz *et al.* (1998) use dendrochronologic constraints from redwood growth rings from a single nearby tree as a maximum age for the oldest earthquake at the site. Dendroseismology is the study of perturbations in annual growth rings as a result of seismic disturbance. At Grizzly Flat abrupt decrease in growth ring width from one redwood stump was interpreted as earthquake evidence. Trees can be individualistic in response to disturbance, typically multiple trees should be sampled to ensure the disturbance in growth ring width is not unique to one tree (Jacoby, 2000).

Other disturbances may force change in annual ring growth including; climate change (i.e. drought), disease or infestation, landslide, rockfall (Jacoby, 2000; Kozaci, 2012). To preclude these possibilities the stump should be cross-correlated with other local redwoods near and far from the fault to both confirm the observed stunted growth pattern near the fault, and to exclude the possibility that the change in ring width was not a result of some other regional disturbance. The authors dated only the wider growth rings, and used a preferred age that excluded low probability ranges with no explanation for the excluded data. Fumal provides an alternative age model for Grizzly flat that incorporates the reinterpreted event evidence, and does not use the dendrochronologic age constraint used by Schwartz *et al.* (1998). In Fumal's model GF-1 is 1906, GF-2* has a modeled age range of 1828 – 1906, and could be 1890, though the geologic evidence for this event is the weakest. GF-3* has a modeled age range of 1733-1872, and is probably 1838, and GF-4* has a modeled age range of A.D. 1105-1545 (Fumal, 2012).

Summary of Earthquakes

Here, we summarize and correlate event evidence outlined in the section above for all paleoseismic sites on the Santa Cruz Mountains section of the San Andreas fault. At Hazel Dell, our E3 formed an approximately 7 meter long, 1.5 meter wide, and 1.5 meter deep fault-bounded depression (Figure 9). The E3 earthquake horizon and overlying units incorporate historical artifacts (axe-cut wood chips) which place this event in the post-European time period. At the Mill Canyon site event MC-2 forms a large fissure 1 meter wide and 1.5 meters deep. This event occurred while unit 5, a sand and gravel with some soil development was at the ground surface, and falls within the range A.D. 1789-1904

(using Fumal's OxCal model 2; Fumal, 2012), Fumal identifies 1838 as a candidate historical earthquake for this event (Fumal, 2012). The MC-2 earthquake produced a much larger fissure (Figure 9), than those associated with the 1906 event horizon at the site. At Arano Flat, event AF-2 forms a fissure 1 meter wide and 1 meter deep, similar size and depth as the fissures associated with this event at both Mill Canyon and Hazel Dell (Figure 9). Event 3 at all three sites occurred in a window of time while the landscape was stable and soils were developing at all three sites (Figure 9). 1838 is the largest event reported in historic time for the Santa Cruz and Watsonville areas, and best explains the amount of deformation associated with the fissures observed at Hazel Dell, Mill Canyon and Arano Flat, and falls within the timing constraints from all three sites. Grizzly Flat also has event evidence that falls within this time period, GF-3* (Fumal, 2012), so 1838 may have ruptured the full 14 km between these sites (Figure 10).

The penultimate earthquake at Hazel Dell is also historic, examining the historic record reveals that the 24 April 1890 earthquake generated surface rupture along the same trace that ruptured 16 years later, in 1906, south of the Pajaro River (Lawson, 1908). An offset channel deposit at Arano Flat contained bottles dating from 1870 to 1890, and has 3.5 m cumulative displacement from 1906 and 1890. If the observed Arano Flat displacement of 3.5 meters is a combined displacement for 1890 and 1906, and at least 0.5 meters of the 3.5 meters occurred in 1890 (and the remaining 3 m occurred in 1906), then there is a greater than 95% chance that a rupture would extend the 1.5 km between Arano Flat and Mill Canyon, using the methodology of Biasi and Weldon (2006, 2009). There is a depositional hiatus in this time period at the Mill Canyon site, because of this it is probable that the 1890 and 1906 earthquakes ruptured the same stratigraphic horizon and

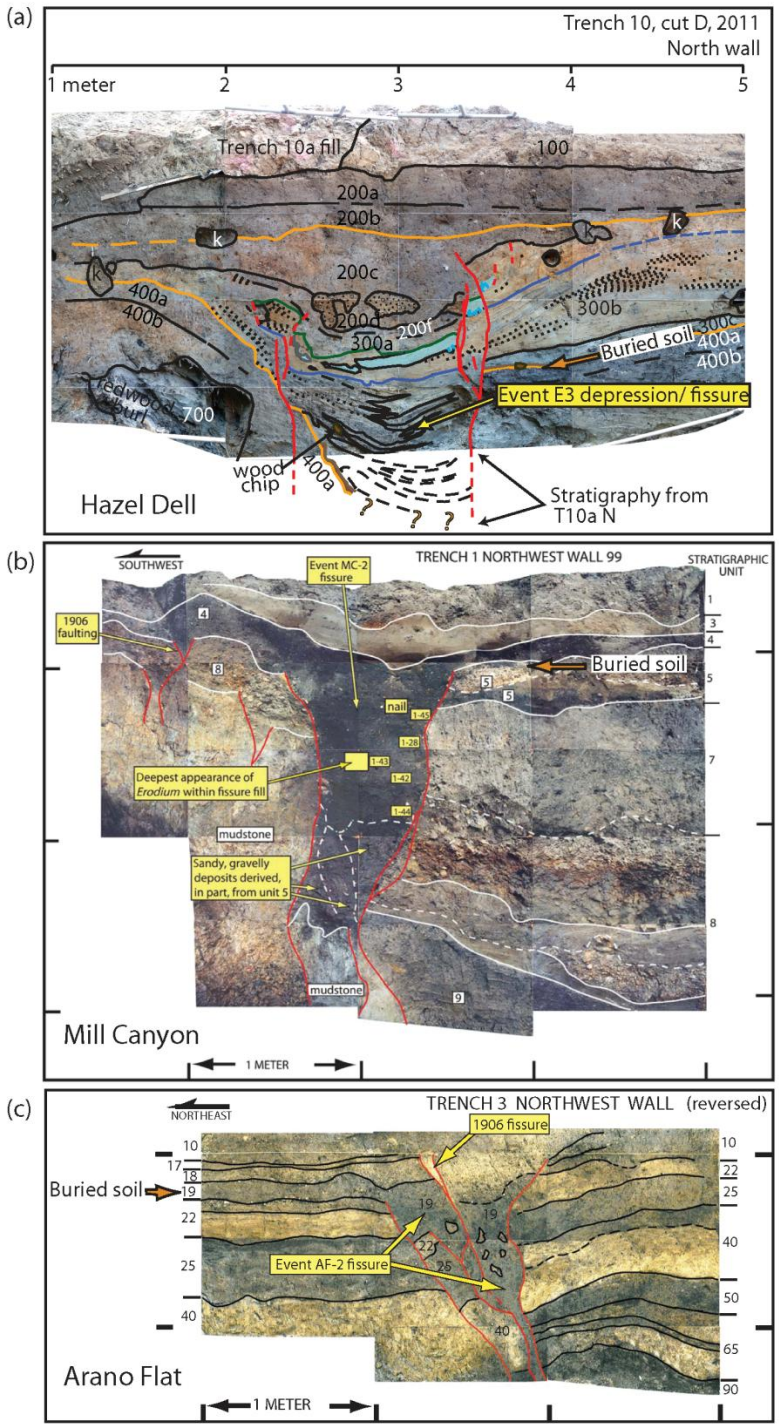

Figure 9. Photomosaic logs showing evidence for 1838, (a) event E3 at Hazel Dell, (b) event MC-2 at Mill Canyon (log from Fumal, 2012; reprinted with permission from T. Dawson) and (c) event AF-2 at Arano Flat (log from Fumal *et al.*, 2003b). This earthquake forms large fissures of comparable size and depth at all three sites, and occurs while organic soils are at the surface at all three sites. This earthquake generated a depression 1.5 meters wide and 1.5 meters deep at Hazel Dell, a fissure 1 meter wide and 1.5 meters deep at Mill Canyon, and a fissure 1 meter wide and 1 meter deep at Arano Flat.

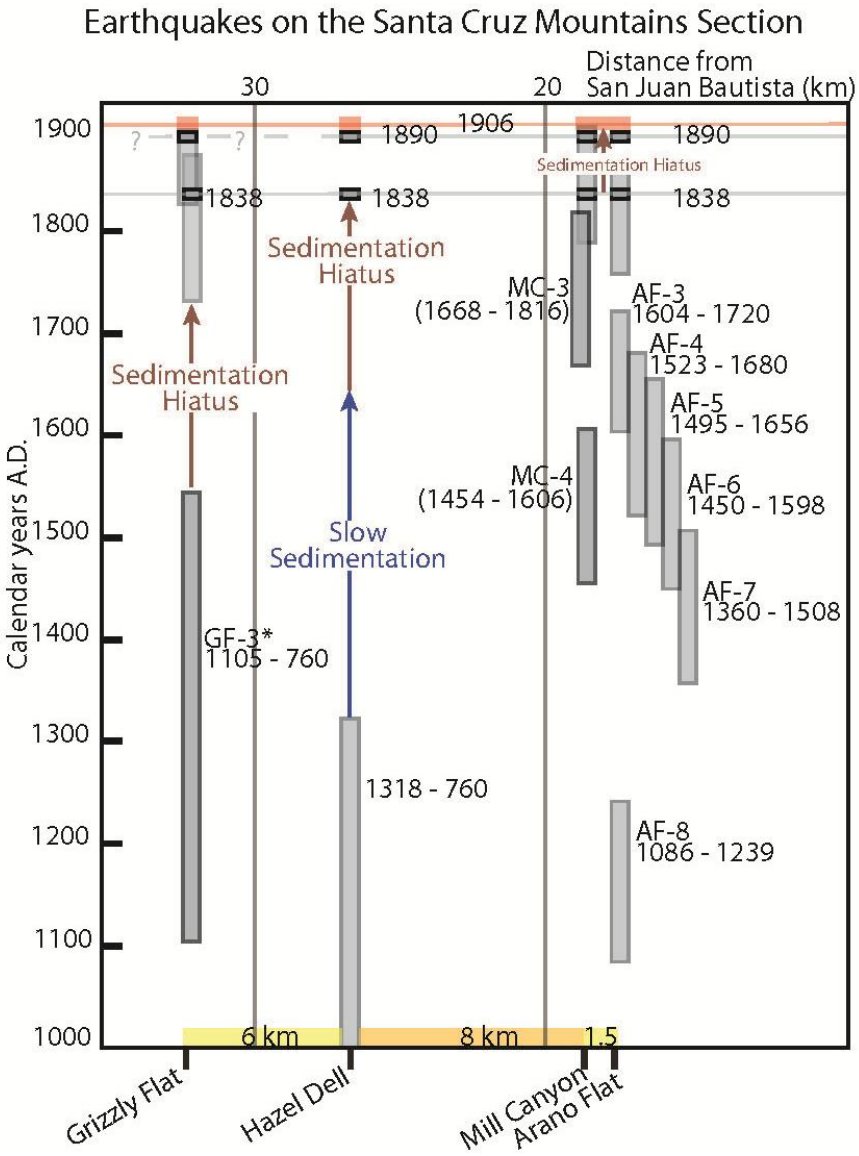

Figure 10. Time space diagram for the SAS showing the distribution of paleoseismic investigation sites. Distance north of SJB shown at the top of the figure. Sites from north to south are; Grizzly Flat (Schwartz *et al.*, 1998; Fumal 2012), Hazel Dell (this study), Arano Flat (Fumal *et al.*, 2003a, 2003b), and Mill Canyon (Fumal, 2012). Distance from Hazel Dell to neighboring sites shown at the bottom of the figure. Modeled event age ranges are shown as rectangles for all four sites, horizontal lines are event correlations between sites.

are not paleoseismically distinguishable as separate events. We infer that 1890 did occur at Mill Canyon based on reinterpreted surface rupture evidence from Arano Flat, and given the high probability that surface rupture extended the short distance between these two sites

(Biasi and Weldon, 2006, 2009). Similarly, given an observed displacement of at least 0.5 meters at Arano Flat, using Biasi and Weldon (2006, 2009) there is ~90% probability the rupture would extend the 9.5 km distance between Arano Flat and Hazel Dell. There is weak evidence of an earthquake at Grizzly Flat in this time period (Fumal, 2012); however it is possible that the 1890 earthquake did not extend this far north (Figure 10).

Earthquake Length and Magnitude Estimates

A 14 km long surface rupture could be generated by a M_w 6.4 earthquake based on scaling relationships such as Hanks and Bakun (2002). This would be a minimum estimate for the 1838 earthquake, if the rupture spanned all four sites, as we argue. The geologic evidence combined with the historic record suggests that 1838 was a much larger magnitude than this, so had a longer rupture and likely spanned much of both the Peninsula and Santa Cruz Mountains sections, if not the full 140 km length (Tuttle and Sykes, 1992; Toppozada *et al.*, 2002). This earthquake generated fissures 1.5 to 1 m wide and deep at Hazel Dell, Mill Canyon, and Arano Flat. We propose that at least 1.5 to 1 m of slip occurred in this event to open fissures of equivalent width and depth. Using the empirical relationship between maximum displacement and magnitude (Wells and Coppersmith, 1994) we estimate that the 1838 earthquake was at least moment magnitude M_w 7.0, for a maximum displacement of 1.5 m at Hazel Dell. For this magnitude we estimate a minimum rupture length of 62 km, assuming a seismogenic depth of 13-15 km, and using the small earthquake (up to M_w 7) scaling relationship of Hanks and Bakun (2002). This rupture length estimate, based on our geologic estimate of slip in this event, agrees well with rupture length estimates by earlier researchers (Topozzada and Borchardt, 1998;

Toppozada *et al.*, 2002; Tuttle and Sykes 1992) and suggests that the 1838 event ruptured most of the Santa Cruz Mountains section, and some portion of the Peninsula section, but not necessarily the full 140 km length of both sections. Additionally, using a technique that correlates point measurements of displacement along a fault with the empirical relationship between surface rupture length and moment magnitude (Hemphill-Haley and Weldon, 1999) we estimate these displacements were generated by an ~ M_w 7.0, with a range of M_w 6.8 to 7.2 within the 95% confidence interval. For this estimate we use four displacement measurements from Hazel Dell, Mill Canyon, Arano Flat and Filoli, (1.5 m, 1 m, 1 m, 1.6 m ± 0.7, respectively), and assume 83 percent of the fault is sampled (for the 83 km distance between sites) for a 100 km rupture length (Tuttle and Sykes, 1992). We prefer this method and range of estimated magnitudes for the 1838 earthquake.

The 1890 earthquake and its aftershocks were widely felt from Santa Cruz to San Juan Bautista (Holden, 1892). Based on geologic evidence this rupture extended at least the 10 km from Hazel Dell to Arano Flat, and probably extended south of the Pajaro River (Lawson, 1908) totaling at least ~14 km. Using the scaling relationships of Hanks and Bakun (2002) we estimate a moment magnitude range of M_w 6.2 to 6.4, for these rupture lengths. In light of new paleoseismic data and earthquake and aftershock descriptions from S. Holden (1892) the 1890 earthquake was greater than earlier magnitude estimates based on the historic record alone (Toppozada *et al.*, 1981; Bakun, 1999; Tuttle and Sykes, 1992). We propose a range of displacements of 0.5 to 1.7 meters in the 1890 event, based on the combined 1906 + 1890 displacement of 3.5 m at Arano Flat. If 1906 generated 1.8 m displacement (the upper limit from Wright's tunnel; Prentice and Ponti, 1997), then we assign the remaining difference of the cumulative displacement to 1890, an upper value of

1.7 meters of slip. The lower slip estimate, 0.5 m, is based on the high probability the rupture extended between Arano Flat and Hazel Dell (explained above). Scaling relationships between maximum displacement and magnitude for strike-slip earthquakes by Wells and Coppersmith (1994) yield a moment magnitude range of M_w 6.6 to 7.0 for this range of displacements. Additionally, the empirical relationship between average displacement and magnitude for strike-slip earthquakes (Wells and Coppersmith, 1994) yields a moment magnitude range of M_w 6.8 to 7.2 for the range of displacements outlined above. Regardless of the method used to estimate moment magnitude we find that the 1890 earthquake was > M_w 6.2. We note that the moment magnitude estimates using empirical regressions for strike-slip earthquakes (Wells and Coppersmith, 1994) and the upper range displacement value of 1.7 m are high relative to magnitude estimates from historical intensity observations (e.g. Bakun, 1999). This suggests that perhaps our upper range estimate of displacement for this event, 1.7 m, is high. For this reason we favor the lower magnitude range for these empirical estimates (Wells and Coppersmith, 1994) for a 0.5 m displacement.

We observe that ground rupturing historic earthquakes on the San Andreas fault are clustered in the 19th to early 20th centuries and are followed by 8 decades of seismic quiescence for earthquakes greater than M_w 6 (prior to the M_w 6.9 1989 Loma Prieta earthquake). Our composite paleoseismic record shows that in the 68 years before the 1906 earthquake the San Andreas fault ruptured at least a 14 km length of the Santa Cruz mountains section twice, with recurrence intervals of 52 and 16 years (1838-1890 and 1890-1906, respectively), and strain released in those events is two to three times greater than the strain that would have accumulated in that length of time (assuming a long term 17

mm/yr slip rate; WGCEP, 2002, 2007). A 3,000 year earthquake record on the Southern San Andreas fault reveals that there is no relationship between recurrence interval and offset (Scharer et al., 2010), and that earthquake recurrence fits neither time nor slip predictable fault behavior models (Weldon et al., 2004). Other plate boundaries with long geologic records also reveal clustered earthquake sequences that terminate with a great earthquake or outsized event, (e.g. Goldfinger *et al.,* 2013). These broad periods of strain accumulation and relief are called supercycles, a cumulative cluster of multiple earthquakes that relieve the accumulated strain over a longer supercycle interval (Sieh *et al.*, 2008). Relative seismic quiescence along the northern San Andreas fault in the last century has also been explained by a stress shadow cast by the 1906 earthquake (negative Coulomb failure stress change, e.g. Stein, 1999; Freed, 2005), with the prediction that seismic activity in a region picks up again as a region steps out of stress shadow from a previous great earthquake. Another model is that the SAS is a transition zone between creeping and fully locked sections of the SAF, and may rupture more frequently in moderate sized earthquakes, like Parkfield, but less regularly. The 1906 earthquake propagated from the locked SAF in the north to the south and rupture ended near San Juan Bautista (Lawson, 1908). We suggest that 1906 displacements on the SAS were large enough that the earthquake essentially shut off the fault and affected how the fault usually behaves in the absence of great 1906-type events, such as the relatively smaller earthquakes observed during the 19th century. We prefer this last model, but until we refine the long recurrence behavior on this section of the fault we can only speculate.

The Arano Flat site has a long earthquake record (Fumal *et al*., 2003b), and identifies multiple events in the 500 year period prior to 1838 (Figure 10). Either the record

at Hazel Dell is incomplete, as suggested by the lack of stratigraphy in the older section, or Arano Flat experiences more surface rupturing earthquakes than Hazel Dell located a mere 9.5 km to the north. If there are more frequent events at Arano Flat than neighboring sites, it would suggest there is a transition zone within the southernmost Santa Cruz section and the creeping San Juan Bautista section to the south. In this scenario some ruptures do not fill the whole SAS section. This scenario only fits the earthquake chronology at one site and does not fit scaling relationships we have discussed in this article (i.e. Biasi and Weldon, 2006, 2009). We find it more likely that the longer earthquake record at all other sites on the Santa Cruz section are incomplete.

Conclusions

We present a new paleoseismic record from Hazel Dell and combine it with three nearby paleoseismic records along the Santa Cruz Mountains section of the San Andreas fault. The Hazel Dell site provides the first definitive paleoseismic evidence of two 19th century ground rupturing events on the Santa Cruz Mountains section. We find that sediment accumulation and the preservation of earthquake evidence varied at all four sites, making it difficult to determine a complete record of earthquakes from just one site. Hazel Dell and Grizzly Flat each have a long multi-century sedimentation hiatus in the older stratigraphic record, while Arano Flat, Mill Canyon and Grizzly Flat all have a sedimentation hiatus spanning multiple decades in the nineteenth century (Figure 10). An incomplete stratigraphic section leaves time unaccounted for; time in which earthquakes could occur, and generate a paleoseismic earthquake record indistinguishable from subsequent earthquakes. By combining earthquake evidence from all four sites we are able

to compare similarities in event deformation, identify depositional hiatus at individual sites, and more confidently assess age distributions for the events.

Based on our interpretation of paleoseismic and historical accounts, the Santa Cruz Mountains section of the San Andreas fault ruptured in 1838, 1890 and 1906. This section ruptured in three earthquakes closely spaced in time, culminating in the largest, 1906 earthquake. If present results from Grizzly Flat and Hazel Dell are complete they suggest that there was a ~500 year period of seismic quiescence prior to the flurry of surface-rupturing earthquakes in the nineteenth and early twentieth centuries. However, Arano Flat and Mill Canyon have longer earthquake records, and have greater stratigraphic resolution and identify likely earthquakes in the 500 year period prior to 1838. More paleoseismic work needs to be done on the SAS to resolve the surface rupturing earthquake chronology in the period prior to the 19th century.

Data and Resources

Fault traces for a regional fault map (Figure 1) are from: U.S. Geological Survey and California Geological Survey, 2006, Quaternary fault and fold database for the United States, last accessed December 2012, from USGS web site: http//earthquakes.usgs.gov/regional/qfaults/ (last accessed 28 August, 2013).

Supplemental historical information for Corralitos, the book by Pybrum-Malmin (1998) is available at http://www.corralitoshistory.com/additions.html (last accessed 30 September, 2013). The site is updated and maintained by Pybrum-Malmin.

The OxCal program by Bronk Ramsey is available online at https://c14.arch.ox.ac.uk/oxcal.html. Bronk Ramsey, C., (2013). OxCal Program, v.4.2,

Radiocarbon Accelerator Unit, University of Oxford, Oxford, United Kingdom, https://c14.arch.ox.ac.uk/oxcal.html (last accessed 2 October, 2013).

EarthScope Northern California LiDAR project 0.5 meter resolution data, http://opentopo.sdsc.edu/gridsphere/gridsphere?gs_action=raster&cid=geonlidarframeportlet&opentopoID=OTSDEM.052008.32610.1 (last accessed 30 December, 2012). LiDAR data and material used in this study is based on services provided to the Plate Boundary Observatory by NCALM. PBO is operated by UNAVCO for EarthScope and supported by the National Science Foundation (No. EAR-0350028 & EAR-0732947). This data and material is also based on [data, processing] services provided by the OpenTopography Facility with support from the National Science Foundation (NSF Award Numbers 0930731 & 0930643).

Bridge

In chapter II I present paleoseismic a new paleoseismic record for the Santa Cruz Mountains section of the SAF, including the first geologic evidence for the historic 1838 and 1890 earthquakes. Historical records note several large earthquakes that caused widespread damage, however it was unknown which Bay Area fault these early historic earthquakes occurred on. The discovery of hundreds of pieces of cut redwood chips in a stratigraphic horizon just below the ante-penultimate (E3) earthquake surface demonstrated that the redwood forest at the site was cut down right before earthquake E3 and thus E3 must be historic. This was in contrast to our previous interpretation that used the absence of expected early historic exotic pollen and the radiocarbon age of delicate macrofossils (which are assumed to be *in situ*) to narrow our wide radiocarbon age distribution for E3

(and E2) into the prehistoric era. In the next chapter I carefully examine age dating techniques and constraints commonly used in paleoseismology as inputs to stratigraphic age models.

In chapter III I examine the contextual uncertainties associated with dating detrital charcoal, macrofossils and wood chips to determine the age of the deposit that contains them. I improve correlations with the historic record and the onset of redwood logging in the Hazel Dell area, by determining the felling date of a buried redwood tree at the site, the probable source of woodchips found at our earthquake E3 horizon. I also investigate the uncertainty that should be included for non-native bio-markers in statistical age models.

CHAPTER III

PUSHING THE LIMITS ON DATING EARTHQUAKES ON THE SANTA CRUZ MOUNTAINS SAN ANDREAS FAULT

This chapter is prepared for publication in the journal Geology. The work presented here reflects a multi-tiered effort to identify uncertainty in age dating techniques and improve age resolution of stratigraphy at the Hazel Dell paleoseismic site, Santa Cruz, California. This includes careful analysis of macrofossils, detrital charcoal and, annual growth rings from wood-chips and a redwood tree stump for radiocarbon age-determination, and review of sediment samples for preserved non-native pollen. I collected both macrofossils and tree ring samples for Accelerator Mass Spectrometry (AMS) radiocarbon analysis. Laboratory pretreatment of AMS samples was performed by me, with oversight from Tom Guilderson at Lawrence Livermore National Laboratories. Dan Gavin conducted non-native pollen analysis, provided in Appendix 3. I am the primary author of the manuscript, Ray Weldon, Tim Dawson, and Dan Gavin all provided editorial assistance.

INTRODUCTION

Earthquakes large enough to produce surface rupture pose great hazard to populations living on active plate margins. Because instrumental earthquake chronologies are too short to determine the frequency of hazardous earthquakes, paleoseismic studies that determine the age and size of past surface ruptures have become a high priority.

Radiocarbon is frequently used to date pre-instrumental ruptures but can have combined contextual and analytical uncertainty on the order of decades to centuries, especially in the past 300 years. Paleoseismologists add ordering information using Bayesian statistical modeling to reduce radiocarbon uncertainty in chronological age models. This often includes removal of apparently inconsistent radiocarbon samples, incorporating historical records, dendrochronology (and similar annual records), and increasingly, the appearance of biomarkers like non-native pollen. Excessive ordering constraints in paleoseismic earthquake age models, especially constraints based on stratigraphically inconsistent detrital charcoal samples and the timing of the first appearance of non-native pollen, have produced earthquake chronologies that are almost certainly incorrect.

Paleoseismology attempts to decipher the surface rupture behavior of a fault over a sufficient number of earthquake intervals to characterize fault recurrence behavior and seismic hazard. Because intervals between surface ruptures on faults span decades to thousands of years, uncertainties in estimates of surface rupture timing have a large impact on our understanding of the variability of earthquakes at a point on a fault, and our ability to correlate prehistoric ruptures between sites along faults. Here, we use absolute ages from high-precision (wiggle-matched) radiocarbon dates to contain the ages of three historic-era earthquakes on the northern SAF, substantially decreasing the recurrence interval of large earthquakes in the last 200 years at this location. Uncertainties in statistical age models are highly dependent on underlying assumptions, contextual and analytical uncertainties should be appropriately incorporated by carefully scrutinizing samples and including adequate uncertainty for historical markers.

The Hazel Dell paleoseismic site on the Santa Cruz Mountains section of the San Andreas Fault (SAF) provides the first definitive paleoseismic evidence of two pre-1906 19th century surface rupturing earthquakes (Figure 1; Streig *et al.*, 2014). Historical records note a few large earthquakes that caused widespread damage in the region in this time period, however it was not previously known with any certainty on which Bay Area faults these earthquakes occurred. Trenches at the site revealed fine-grained interbedded sand and silt above a buried soil that is faulted in the most recent event, 1906 (not shown here, see Streig et al., 2014), and in and two earlier earthquakes (Figure 2). We discovered hundreds of pieces of cut redwood chips coupled with numerous buried redwood tree stumps just below the buried soil, the ante-penultimate (E3) earthquake surface (Figure 2). This demonstrates that the redwood forest at the site was cut down right before earthquake E3, and thus E3 must be historic.

In our earlier study, we found that E2 has an OxCal modeled age range of 1840 to 1906, and E3 has an age range of 1815 - 1895 (both with 2σ uncertainty; Streig et al., 2014). These ages are constrained by AMS dates from redwood macrofossils, woodchips and one historic record of a lumber mill operating in the vicinity by 1832 (Pybrum-Malmin, 1998). To better resolve the onset of logging at the site we collected a slab from one of the logged trees and radiocarbon wiggle matched it and 2 wood chips to the INTCAL13 terrestrial ^{14}C calibration curve. We use these high-resolution age dates to update modeled ages for the onset of logging, and so with great certainty place earthquakes E2 and E3 in the historic period.

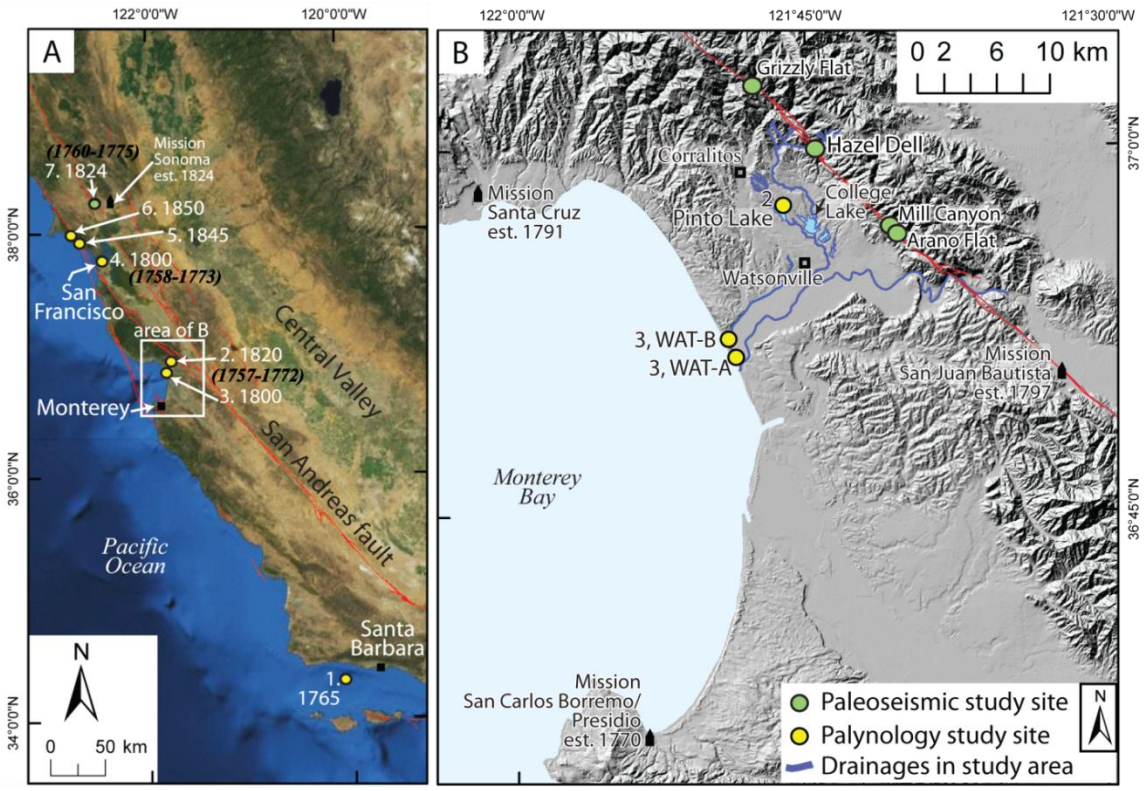

Figure 1. **A.** Locations of palynology studies (A, yellow circles 1-7) and paleoseismic (B, green circles) sites along coastal California. First occurrence of Erodium pollen in deposits: 1. Santa Barbara, 1750 - 1765, Mensing and Byrne (1998); 2. Pinto Lake, Watsonville, 1820 - 1860, Plater et al. (2006); 3. Watsonville slough, 1800 ± 20 years, Byrne and Reidy (2005); 4. Mt. Lake, San Francisco, 1800 ± 20 years, Reidy (2001); 5. Bolinas Lagoon, Marin, 1845 ± 10 years (Byrne et al., 2005); 6. Glenmire, Pt. Reyes, 1850 (Anderson et al., 2013); 7. Triangle G Ranch, Sonoma, 1776 - 1824 (Hecker et al., 2005). Black text is the earliest arrival of Erodium using the Mensing and Byrne migration rate of 30 - 50 km/yr. **B.** Streams in Santa Cruz County shown as light blue lines, the stream flowing from the Hazel Dell site to College Lake shown as a bold blue line. Assuming the first occurrence of Erodium in College Lake is the same as Pinto Lake ~1791 - 1823 (Plater et al., 2006). We infer Erodium was not found anywhere along the streams (blue lines) that flow into these lakes.

^{14}C AGE DATING

We recovered an abundance of datable material from stratigraphic units at Hazel Dell, including; detrital charcoal, macrofossils (inferred to be *in situ*), axe-cut wood chips, and logged tree stumps (Figure 2). Wood, macrofossils (redwood needles and cone fragments) and selected detrital charcoal samples (generally the last resort for a

layer) were analyzed at the Center for Accelerator Mass Spectrometry (CAMS) at Lawrence Livermore National Laboratory (LLNL). We dated 36 radiocarbon AMS samples, of these 3 samples are macrofossils, 15 are detrital charcoal, 4 are from 2 wood chips, 14 are sequential samples from a buried tree stump (Appendix E).

Detrital Charcoal and Macrofossils

In the Santa Cruz Mountains charcoal samples are most often derived from redwoods, which are long-lived and the wood is decay resistant, leading to great difference between radiocarbon ages and the age of the deposit (e.g. fire vs. charcoal burial). As a result, it is generally accepted that at sites where detrital charcoal is the most abundant datable material, success in dating earthquakes relies on analyzing large numbers of radiocarbon samples to identify those samples that are in stratigraphic order. Stratigraphically consistent samples are inferred to have residence times at the surface that is shorter than the time between resolvable layers at the site (Fumal, 2012; Fumal et al., 2003; Lienkaemper et al., 2002).

At Hazel Dell, we dated 15 detrital charcoal samples and found 8, or 53%, to be stratigraphically consistent. To the southeast at Mill Canyon, Fumal (2012) ran 25 detrital charcoal samples, and 5 samples, or 20%, were in stratigraphic order; 1.5 km southeast of Mill Canyon, at Arano Flat 113 detrital charcoal samples were dated (Fumal et al., 2003) and 36, or 31% were in stratigraphic order (Figure 1; age models for Arano Flat are in Streig et al., 2014). By comparison, the number of detrital charcoal samples dated and retained in age models at other paleoseismic sites in California reveals that between 20 – 65% of charcoal samples submitted for AMS dating are deemed reliable (Fumal, 2012;

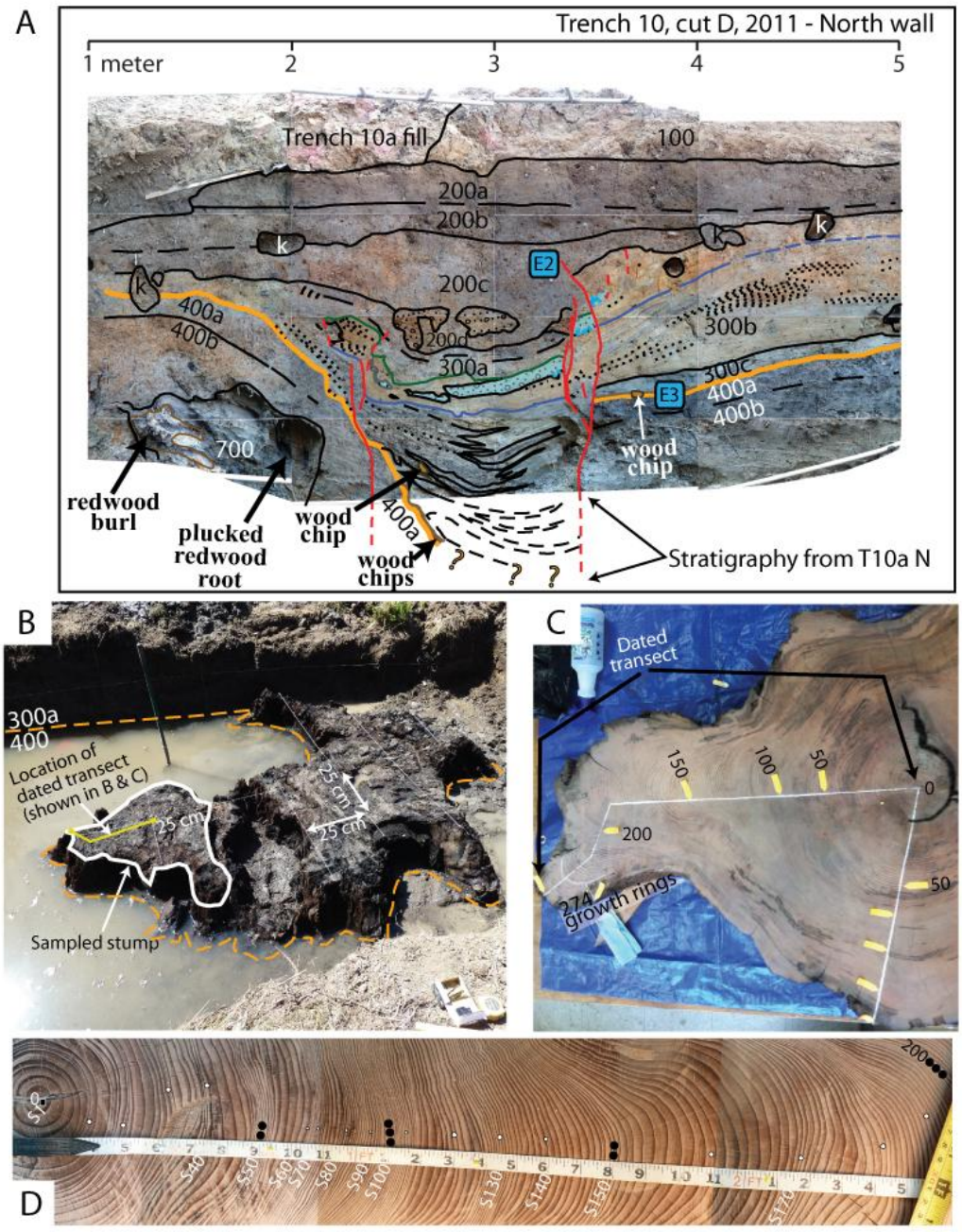

Figure 2. A. Photomosiac log of trench T10D. Showing buried soil unit 400a as a bold orange line, overlain by growth strata units 200 – 300. Wood chips are embedded in the upper horizon of unit 400a, redwood stumps were growning on this surface, the trees and redwood burl are rooted in the horizons below. Red lines are faults, sub-horizontal lines are unit horizons. **B.** Photograph of two buried redwood stumps, 40 - 50 cm below the ground surface at the E3 horizon, Hazel Dell site. Orange dashed line shows the buried unit 400a soil relative to the redwood stump. **C.** The sanded redwood slab with counted tree ring transects shown in white, number of rings shown at the orange arrows. We collected 14 AMS samples from single growth rings distributed roughly evenly from the pith to the outer ring along the long transect. **D**. Polished section of the long transect shown in B.

Fumal et al., 2003; Fumal et al., 2002; Hecker et al., 2005; Kelson et al., 2006; Lienkaemper and Williams, 2007; Lienkaemper et al., 2002; Scharer et al., 2007; Schwartz et al., 1998; Streig et al., 2014), and the remaining are out of stratigraphic order and excluded from age models.

It seems reasonable that identifiable organic remains (often called "macrofossils") should be less susceptible to reworking, so a growing number of paleoseismologists focus on such samples (e.g. Lienkaemper et al., 2002; Scharer et al., 2007). At Hazel Dell we dated 3 macrofossil samples from block samples of the stratigraphy that immediately post-dates our earthquake E3. Using a binocular microscope we identified and collected redwood cone fragments, delicate redwood needles and a redwood branch with needles still attached (Appendix E, samples HD10a-7-22, HD10a-5-18, HD10a-3-28 respectively). Of these only the branch with attached needles (HD10a-3-28; Appendix F) was stratigraphically consistent; the other two macrofossil samples were above this sample but yielded older calibrated ages that were inconsistent with HD10a-3-28 and the historic wood chips and logged tree stump discussed below. These macrofossils were collected from finely laminated sediments that preclude the possibility of subsequent bioturbation; the redwood cone fragments and needles were unquestionably recycled. Similarly, at Wrightwood, CA on the southern San Andreas, Biasi et al. (2002) report that pinecone macrofossils had large inherited ages that were inconsistent with other detrital samples and *in situ* peat dates. We conclude that macrofossils require the same consideration as other detrital radiocarbon samples and should be similarly scrutinized for consistency.

Wiggle Matching Analysis

In an effort to improve the accuracy of our radiocarbon dates and conclusively demonstrate that the site was logged by early European settlers (a critic might argue that Native Americans logged the site, although there is no record of their felling large redwood trees) ^{14}C "wiggle matching" was applied to 2 wood chips with preserved bark and a complete slab of a logged redwood tree stump that we excavated from one of our trenches (Figure 2). Wiggle matching compares a series of sequential ^{14}C dates with the known variation in ^{14}C production through time recorded in the ^{14}C calibration curve, and so with enough samples spanning the curve yields a unique calendar age (e.g. Reimer *et al.*, 2004). The redwood stump was encountered in growth position during 2008 excavations at the intersection of trenches T1 and T6 (Streig et al., 2014). In 2012 we re-exposed two stumps growing together with a combined diameter of roughly 1.75 meters (Figure 2a). We cut a roughly 25cm thick slab from the smaller stump, measuring 60 cm diameter for tree ring analysis (Figure 2 B, C). We collected the smaller stump because it had continuous growth rings; the larger stump was burnt and gouged. We sanded and polished the slab, and counted 274 rings from the pith (inner growth ring) to the outermost preserved ring, and collected AMS samples (Figure 2).

Standard ^{14}C calendar age calibration for these samples yield broad calendar age ranges, often with multi-modal distributions, and with statistical uncertainty on the order of several decades (i.e. using OxCal; Bronk Ramsey, 2009). Using the annual interval between ordered samples from the growth ring count, we plot both a visual and Bayesian statistical wiggle-match (Figure 3; Appendix 2). We use the OxCal (v. 4.2) D_Sequence model with gaps between samples to represent the number of rings counted between

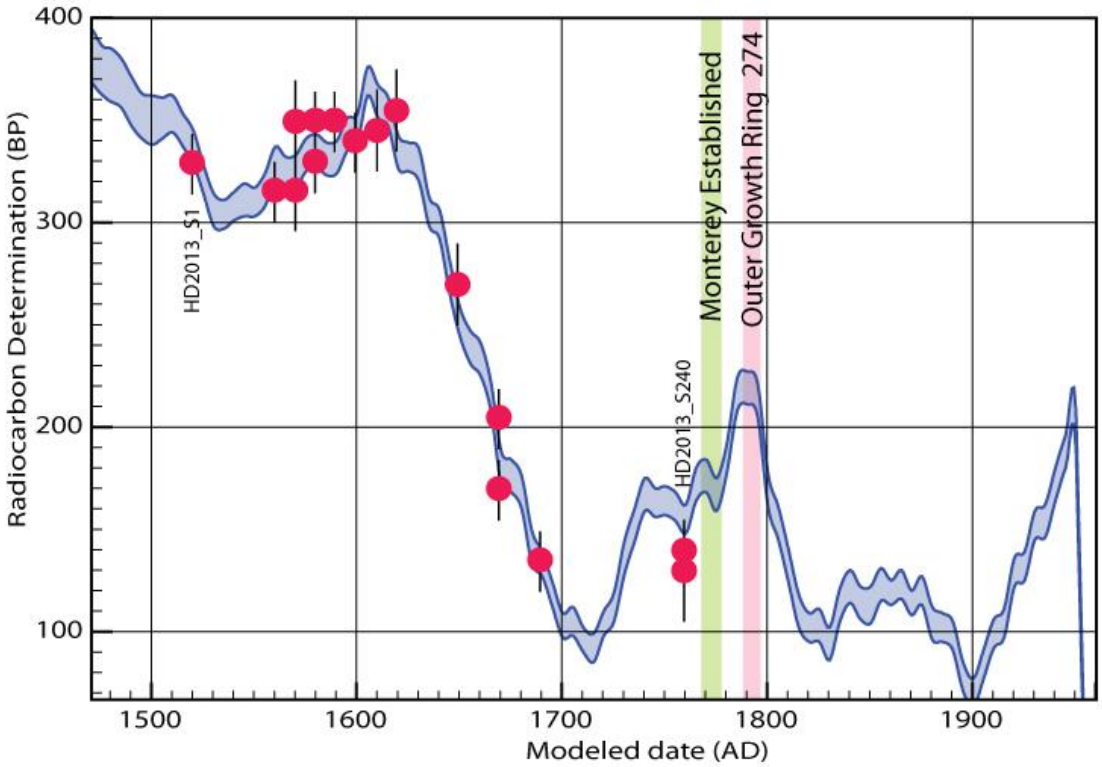

Figure 3. Wiggle match ^{14}C plot showing the best fit date of 1789 – 1797 for the outer growth ring of the redwood stump, with ^{14}C ages from the dated transect against the IntCal 13 calibration curve (Reimer et al., 2013). The 2σ modeled age range for the outer growth ring was modeled using D_Sequence, Oxcal v 4.2.2 (Bronk Ramsey, 2013). Red dots show the measured radiocarbon age in years BP, lines are 1σ laboratory uncertainty. The dots are sequential, gaps between samples reflect the interval, or number of growth rings between samples. The oldest sample is the center of the tree, the first growth ring, sample HD2013_S1, where 1 is the order in the tree ring sequence.

samples. We trim outliers through several model iterations to identify inconsistent ages. We discarded both samples from ring 271, which yielded much older ages than all of the others, perhaps due to contamination of the tree's surface by groundwater (Appendix E). We find, at 2σ certainty, that the outermost ring has an age of 1789 – 1797 and the innermost 1516 - 1523 (Figure 3; Appendix G). We also ran a conservative model with ring count uncertainty (+/- 2 years/decade) and found a 2σ modeled age range of 1779 – 1859 for the outermost ring, which is consistent with the above D_Sequence result and confirms our hypothesis that early European Settlers cleared the site.

We also wiggle-matched samples from the inner and outermost growth rings from two wood chips that had preserved bark. However, redwood growth is variable around the trunk of the tree and so the outer growth ring on a wood chip may not be from the last growth year of the tree. This can be a result of discontinuous or pinching growth rings, micro-rings, false growth rings which occur when limiting factors reduce growth rates, and areas with concentrated growth hormone produce larger more continuous growth rings (Fritz, 1940; Speer, 2010). Because of its irregular growth it is possible that the tree was cut down after the outermost recognized wood chip ring's age. We counted the number of preserved rings in 10 traverses on our tree cross section slab where the bark is preserved and found 32 years between the longest and shortest tree ring transects. From this data we infer that 11 ± 11 years (1 standard deviation) uncertainty needs to be added to the wood chips outermost ring age to determine its felling age.

The wood chips yield 2σ modeled outer growth ring age ranges of 1698 to 1850 for sample HD_2011_WC1 and 1725 to 1973 for sample HD_2011_WC2 (using OxCal v.4.1.7, Bronk Ramsey, 2012; see Streig et al., 2014 for additional discussion). While these results are consistent with the tree, because there are only 2 samples for each wood chip, and none landed on a steep or unique portion of the calibration curve, the results are less precise. The more conclusive result with woodchip sample HD-2011_WC1, which had 180 years between its two samples, is significant because it also limits E3 to have occurred before 1850, strongly suggesting that E3 occurred earlier than two historic large earthquakes in the late 1800's (1865, 1890) with unresolved fault sources.

EXOTIC POLLEN AS A RELATIVE AGE INDICATOR

The first appearance of pollen from exotic species, such as *Eucalyptus, Erodium cicutarium, Rumex* and *Plantago,* can reveal the onset of European settlement and related major land use changes (Anderson et al, 2013). *Erodium* is identified in cores from the Santa Barbara Basin dated around 1769 coinciding with the introduction of livestock by Spanish missionaries that year preceding significant Spanish settlement in California (Mensing and Byrne, 1998). Mensing and Byrne (1998) estimate a 30 to 50 km/yr migration rate for *Erodium* across the California grasslands, which would place *Erodium* in the Monterey Bay area by ~1770.

Erodium cicutarium is the most common exotic pollen source used as a relative age indicator by paleoseismologists in California (e.g. Fumal, 2012; Fumal et al., 2003; Hecker et al., 2005; Lienkaemper and Williams, 2007; Lienkaemper et al., 2002). The Mensing and Byrne (1998) *Erodium* migration rate is frequently used as a first-order age estimate for the stratigraphic horizon containing the first occurrence of *Erodium* pollen. It has also been used to argue that key sediment layers lacking non-native pollen preceded European settlement, and consequently an earthquake within stratigraphy lacking this pollen has been considered pre-historic. When these assumptions are applied as historical razors (a certain year with little to no uncertainty) in age determination models they can affect age interpretations by unrealistically forcing historic stratigraphy into the prehistoric period (if only by years).

At the Mill Canyon site, south of Hazel Dell, the ante-penultimate earthquake, MC-2 occurred at a stratigraphic horizon below the first appearance of *Erodium* pollen. Fumal (2012) presents two OxCal age models (Bronk Ramsey, 2009) for the site, the first

evaluates the effect of using potentially recycled charcoal from a fissure to constrain the timing of earthquake MC-2. The charcoal samples force the timing of a 19th century stratigraphic unit into the 18th century, and the estimated arrival of Erodium (based on the migration rate) is used to validate the 18th century result (Fumal, 2012). The second age model in Fumal (2012) excludes the suspect charcoal samples and Erodium from the age model, and the age of event MC-2 has a younger age distribution weighted with 95% confidence in the 19th century, shifting the probability distribution function (pdf) for the age of this event to reflect high probability that the most recent earthquake (MRE) occurred in the recent historic past.

A paleoseismic study on the Rodgers Creek Fault, in north San Francisco Bay, finds the first occurrence of *Erodium* above a prominent stratigraphic marker that reflects land-use disturbance, which probably coincides with the establishment of the first land grants and the local onset of grazing, reported to have begun around 1830, and the MRE at this site occurred just before that (Figure 1; Hecker et al., 2005). Despite this historical constraint, the authors give this horizon an age range of 1776 to 1830, the earlier age limit is based on the *Erodium* migration rate (Hecker et al., 2005). Hecker et al. (2005) present two age models to explore the effects of radiocarbon calibration model assumptions (i.e. use of historical razors) and sample selection on modeled stratigraphy and earthquake age ranges (using OxCal). One model uses the estimated exotic pollen arrival of 1776 as a historic constraint (based on Mensing and Byrne, 1998) this boundary forces a highly asymmetric modeled age distribution for the MRE, ranging between 1715 and 1776 AD at the 95% confidence interval. In a second model the authors use the historical date 1824, the founding of Mission Sonoma, as the historical model constraint.

In this model the pdf for the MRE broadens and shifts to 1740 - 1824 AD at the 95% confidence interval (Hecker et al., 2005). The first model excludes all dates after 1776 (the estimated arrival of exotic pollen) for the modeled pdf for the MRE, and places greater confidence on the estimated arrival date for exotic pollen than is warranted.

Erodium, is a problematic biomarker; it is generally suited to grasslands and is not found in forest shade (McLaughlan and Clark, 2004). It has low pollen production and dispersion, and has heavy seeds that are primarily dispersed by water transport and animal migration (Mensing and Byrne, 1998). Additionally, geologic (i.e. depositional setting), geographic (climate, topographic relief) and biologic (landscape openness) factors all contribute to pollen preservation and abundance in deposits and thus the success in applying this technique as an age indicator in paleoseismic studies. All of these factors impact the arrival of Erodium and preservation of its pollen in the stratigraphic record.

The first occurrence of *Erodium* in the Monterey Bay area is historically constrained to the early 19th Century (Plater et al., 2006; Byrne and Reidy, 2005; Hendry, 1925), later than the estimated arrival ~1770 from the migration rate (Mensing and Byrne, 1998). Cores from Pinto Lake, near Hazel Dell, Arano Flat, and Mill Canyon paleoseismic sites (Figure 1) show the first occurrence of *Erodium* pollen in the period between 1791 to 1823 (Plater et al., 2006), 20 to 50 years later than the estimated arrival date, and at least 20 years later than the first documentation of cattle and horse grazing in the region in 1807 (Pybrum-Malmin, 1998). A marsh core study in the Watsonville Slough (Figure 1) finds *Erodium* at a depth of 100 cm, the authors assign a date of 1800 ± 20 years to this horizon. This date is inferred and is based on an earlier study of *Erodium*

macrofossil remains in adobe bricks at Mission San Juan Bautista, established in 1797 (Figure 1; Byrne and Reidy, 2005; Hendry and Kelley, 1925).

The first occurrence of *Erodium* in the greater San Francisco Bay region, generally from 1770 to 1860 (Figure 1), is also several decades later than estimated using the Mensing and Byrne (1998) migration rate. A core at Mountain Lake in San Francisco finds the first occurrence of *Erodium* around 1800 ± 20 years (Figure 1; Reidy, 2001), and is within the same range as Monterey Bay. On the north side of San Francisco Bay, a marsh core study at Bolinas Lagoon finds the first occurrence of *Erodium* appears just before 1850 (Figure 1; Byrne, 2002). A second core site, at Glenmire, in Pt. Reyes (Figure 1), dates the first occurrence of exotic Plantago grass, to 1850, and the first occurrence of *Erodium* is stratigraphically above (younger than) that horizon (Figure 1; Anderson et al., 2013).

These studies highlight that the measured and historically constrained ages of the horizon associated with the first appearance of *Erodium* in this part of California is almost always later than the estimated arrival (Figure 1), and shows that *Erodium* is a difficult biomarker, especially in forest soils. Without additional local palynology studies, the migration rate proposed by Mensing and Byrne (1998) should be used only as a limit for the timing of the first stratigraphic occurrence of the exotic pollen. We have demonstrated that this limit can predate the actual age of the deposit by several decades. Site specific conditions and local historical records should inform the interpretation of the range of calendar years represented by the presence of exotic pollen, if a first order estimate based on the migration rate of *Erodium* is used in age determination models then

appropriate uncertainty on the estimate should be included in the model so a probable range of ages are not excluded.

Like many paleoseismic sites, at Hazel Dell we have found that sediments we know to be historic lack exotic pollen, but also have poorly preserved pollen abundance from native plant species (Appendix H). The lack of exotic fossil pollen does not inform the age of the stratigraphic units when low abundances of native pollen are preserved, a negative result (lack of preserved pollen) is inconclusive.

CONCLUSIONS

Incorporating stratigraphic, chronologic and historical ordering constraints in a statistical age model can reduce the range of ages for a calibrated radiocarbon date, and can be used to estimate the probable range of ages for an earthquake horizon (Biasi and Weldon, 1994). However, using incorrect constraints or even correct constraints without adequate uncertainty on their age estimates can generate erroneous probability distribution functions for earthquake ages. At our site, and many paleoseismic sites the four major sources of contextual error are uncertainty in radiocarbon ages derived from detrital charcoal, reworked macrofossils, the age of wood chips as a result of irregular tree growth, and the first occurrence of non-native pollen. To use bio-markers in age models local palynology studies are required for decade precision age control, and any study that uses regional migration rate requires much greater uncertainties then currently applied. These results are significant because applying age indicators without appropriate uncertainty to age determination models unrealistically skews pdf's for the unit or event

in question, and incorrect age results yield incorrect earthquake recurrence for paleoseismic studies.

We carefully scrutinized stratigraphic, chronologic and historical ordering constraints for Hazel Dell, and build a Bayesian statistical age model to estimate the probable range of ages for E2 and E3 at the Hazel Dell site. We interpret E1, the most recent event to be the 1906 rupture. Based on the historical constraints from the cut wood chips, we find two additional historical earthquakes that occurred in the 19th century, the modeled age for E2 is 1811 to 1906 (2σ confidence interval), and the modeled age for E3 is between A.D. 1788 and 1851 (2σ confidence), and E4 occurred before the 1523 AD (95% confidence level of the dating; Appendix 4). These results are robust, and increase the number of surface rupturing earthquakes on the SAF in the Santa Cruz Mountains three fold for the last 200 years.

BRIDGE

Paleoseismic studies aim to determine the age, style of deformation, and size of past surface ruptures, but large age uncertainties are inherent in these studies. In chapter III I refine earthquake age estimates, and timing of surface rupturing earthquakes on the on the Santa Cruz Mountains section of the SAF. I apply a dendrochronologic age dating technique, 'wiggle-matching', to reduce uncertainty on the timing of the last three surface rupturing earthquakes at Hazel Dell, and investigate other relative age markers and how they can be incorporated into statistical age models. We use statistical age models that use ordering information to reduce these uncertainties, and review how these age models, or ordering information can be more appropriately incorporated into age models. I

highlight the careful consideration that should be given to each input in an age determination model, and how dropping uncertainties on relative ages used as razors in these models can incorrectly trim an entire distribution of probable event ages that have in some cases have contained the actual event age.

In chapter IV I present paleoseismic and structural results from the Frazier Mountain site (FM site) on the Southern SAF. In this chapter I investigate the style of deformation and size of past surface ruptures at the FM site for the last five earthquakes. This study presents new results for a 200 km stretch of the fault that previously lacked this type of paleoseismic data, data that are key components in fault hazard characterization. In the next chapter I use 3D structural data across a step-over at the FM site to compare the style and amount of deformation in the last five earthquakes. I retrodeform stratigraphic surfaces to isolate folding per-event, and relate lateral slip on the fault to structural relief (fold relief) across the step-over to estimate ranges of lateral slip for the last 5 earthquakes.

CHAPTER IV

COSEISMIC FOLD DEFORMATION FOR THE LAST 5 EVENTS ACROSS A RELEASING STEP-OVER AT THE FRAZIER MOUNTAIN PALEOSEISMIC SITE, SOUTHERN SAN ANDREAS FAULT, CALIFORNIA

This chapter is prepared for publication in the Journal of Structural Geology, and is co-authored with my advisor Ray J. Weldon, II and Katherine M. Scharer (U.S. Geological Survey). This chapter summarizes a 3D analysis of progressive coseismic fold deformation across a releasing-step on the Southern San Andreas Fault at the Frazier Mountain paleoseismic site. Structural data presented in this article result from 5 years of paleoseismic investigations at the study site by the authors. I combined the structural survey data for each field investigation in a GIS, and generated structural contour maps of the paleo-earthquake horizons to quantify the amount of folding at each horizon for the last five earthquakes. Ray Weldon compiled and interpreted Cone Penetrometer Testing results (CPT), I assisted with this analysis, Ray drafted the corresponding CPT figure included in this chapter. Kate Scharer drafted some of the trench logs, provided the stratigraphic column and provided earthquake age dates from our OxCal analysis in Sharer et al. (2014). I drafted all other figures used in this study. I am the primary author of this chapter, both co-authors provided editorial assistance.

1. Introduction

Pull-apart basins form along releasing bends or steps along strike slip faults, and often preserve thick sections that yield long paleoseismic records of surface rupturing earthquakes (i.e. Onerdonk et al., 2013; Scharer et al., 2007; Weldon et al., 2002). In contrast, sites with geomorphic markers displaced across a fault yield high quality displacements along the fault (Zielke et al., 2010, 2012; Frankel et al., 2007). Geomorphic features are persistent in the landscape through time because they occur in areas of low sediment accumulation and thus rarely provide suitable material for high-resolution age-dating of prehistoric events, making these offsets difficult to attribute to individual earthquakes. This has led to the division of paleoseismology into micro-stratigraphic and micro-geomorphic subdisciplines and, by their nature, studies of the two types are difficult to combine. Determining earthquake chronology and slip estimates at a single site along a releasing bend, or step-over would eliminate the ambiguity inherent in tying earthquake age data from microstratigraphic earthquake chronology sites to nearby undated micro-geomorphic slip sites.

Step-overs, or sags are often closed depressions frequently seasonally inundated, have abundant datable material (i.e. peats and charcoal), and high sedimentation rates, because of this sags are the best sites for preserving evidence of earthquake timing. It is clear from historical ruptures that these depressions grow incrementally during earthquakes (Guo et al., 2012). Our site is located on a releasing (right) step on the SAF, 40 m wide and 150 m long along strike (Figure 1). The goal of this study is to isolate vertical relief generated by prehistoric surface rupturing earthquakes across the step-over at the Frazier Mountain site (FM site), and use structural relief as a proxy for lateral slip

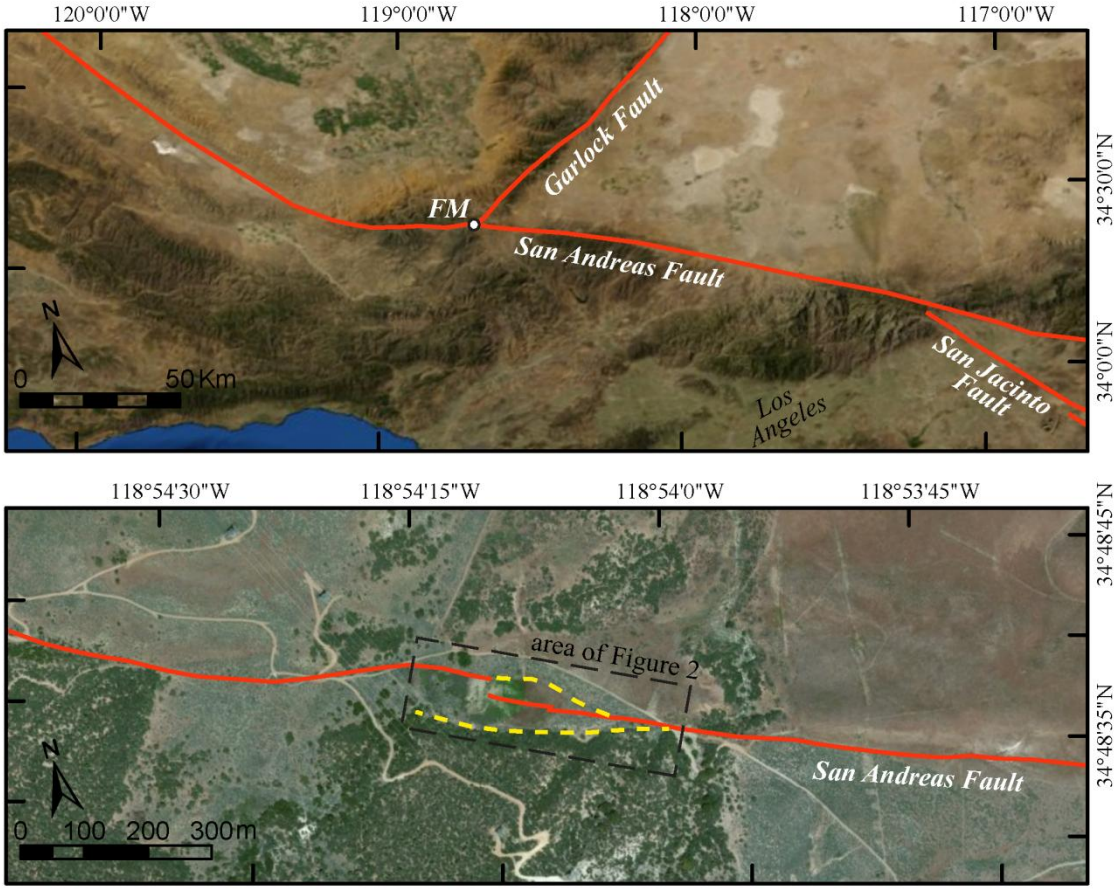

Figure 1. (a) Satellite image of the 'Big-Bend' region of the Southern SAF, CA (NASA Blue Marble: Next Generation imagery, Source: ESRI). Major faults are shown as red lines. The Frazier Mountain site is located in the Big Bend area on the Southern SAF (b) The 100 x 500 meter closed depression (shown in yellow where faults are no longer active) formed in a stretch of the fault where the surface traces of the SAF diverge in a transtensive manner from the regional trend. The past 5 – 10 earthquakes have bypassed the eastern edge of the older, larger step and appear to be the beginning of the end of the step-over. Aerial imagery of the Frazier Mountain paleoseismic site (i-cubed Nationwide Prime, Source ESRI).

on the fault. We carefully document and separate individual folding events and compare vertical relief generated across the site in the last five earthquakes. Geomorphic offsets measured both in the field and from LiDAR data near the site reveal 4 to 5 m of lateral displacement in 1857, FM1 (Sieh, 1978; Madden et al., 2013), we compare the structural relief generated by this known range of slip in 1857 with structural contour maps of vertical relief for four earlier earthquakes, FM 2 - 5. Paleoseismic results of earthquake

evidence and timing of these events at the FM site are presented in Scharer et al. (2014), and are only summarized in this paper.

This study integrates trenching (including digitizing photomosaic trench logs), surveying, B4 LiDAR data, cone penetrometer testing (CPT) and GIS techniques to generate detailed 3D maps of subsurface geologic units, fault traces and related folds across the site (Figure 2). The goal of this analysis is to isolate vertical deformation step-wise, as close to earthquake by earthquake as possible, for the last five earthquakes. This allows us to directly compare the fold orientation, geometry and vertical relief of deformation generated by each earthquake. The general process, assumptions and complications to retrodeforming these stratigraphic horizons are described below.

2. Geometry and Evolution of a Step-over

A releasing step on a strike-slip fault forms what is generally referred to as a pull-apart basin, described by Crowell (1974) as a deep, rhomboidal basin bounded on the sides by subparallel strike slip faults, and sometimes bounded on the ends by perpendicular or diagonal transfer faults that connect to the primary strike slip fault (Sylvester, 1988; Gürbüz, 2010; Mitra and Paul, 2011). Scaled physical models provide useful insights into the progressive evolution of three dimensional geometries of releasing step-over systems and have produced features we observe at the FM site. Vertical structural relief is primarily concentrated on step-over margins by normal faulting and folding, and the trough of the step-over is essentially flat-bottomed to gently dipping (Mitra and Paul, 2011; Figure 3). As cumulative slip across the pull-apart increases, discontinuous en-echelon faults can link up forming cross-basin fault zones

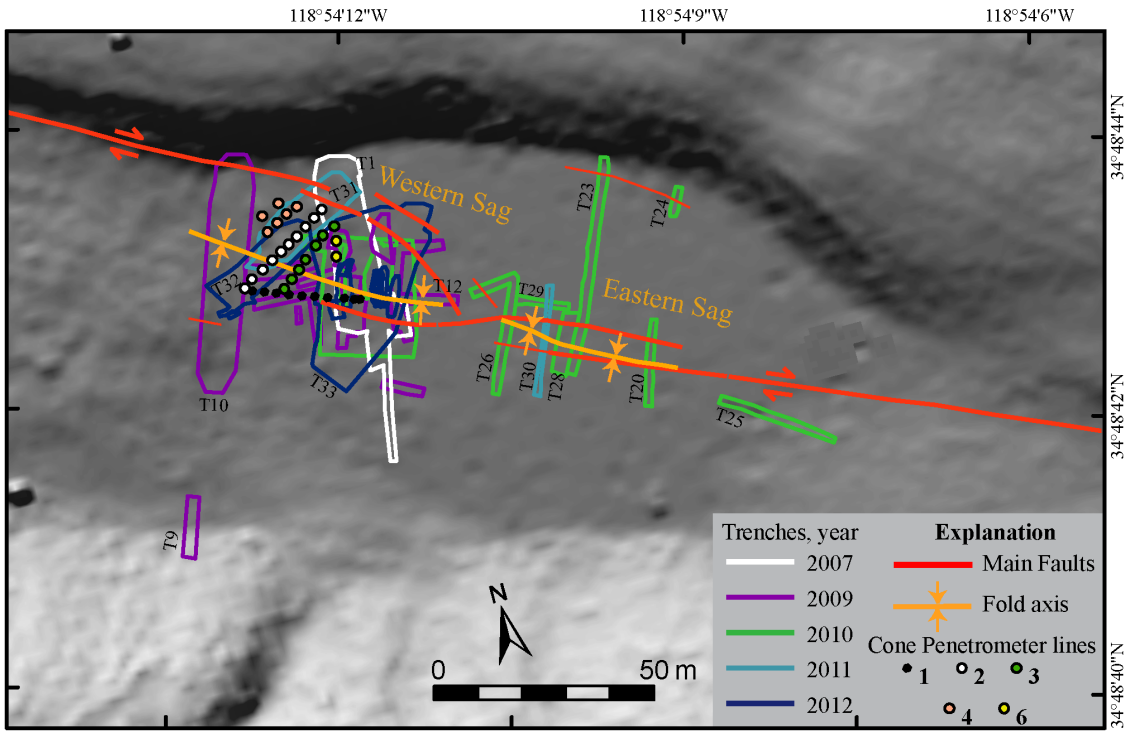

Figure 2. Frazier Mountain site map showing locations of trenches excavated in 2008, 2009, 2010, 2011 and 2012, and Cone Penetrometer (CPT) transects (2011, before the 2011 and 2012 trenches) in the northwestern portion of the site. Major, faults and syncline axes associated with the past 6 earthquakes are constrained by trench exposures of the structures and are shown as red and orange lines on the map, respectively. Hillshade derived from B4 lidar data (downloaded from OpenTopography).

(Wu et al., 2009; McClay and Dooley, 1995). We also observe dual opposing depocenters separated by a locally high area (Figure 3) (Wu et al., 2009; Mira and Paul, 2011).

Historic surface ruptures also inform paleoseismic observations of structural relief generated in earthquakes at the FM site. For example, the recent M7.1 2010 Yushu, Quinghai, China, earthquake ruptured across a releasing bend on the left-lateral strike slip Ganzi-Yushu fault along the Central section of the rupture (Guo et al., 2012) and provides a good example of vertical relief generated as rupture propagates across a releasing step. This step-over is roughly 260 m long and 40 m wide, and about 1 m of lateral slip at the site generated ~ 50 cm of vertical relief and sagging across the step-

over. Photographs and a 3D surface of structural relief generated by the rupture show both diagonal transfer faults and fold deformation through the sag.

Both analog model results and surface rupture observations in the Yushu earthquake are strikingly similar to the observed geometry between sags and faults at the FM site. Combining these models with detailed paleoseismic observations and high-resolution age dating allows us to compare our observations on the timing of faulting across the step-over with models of the evolution of a releasing step.

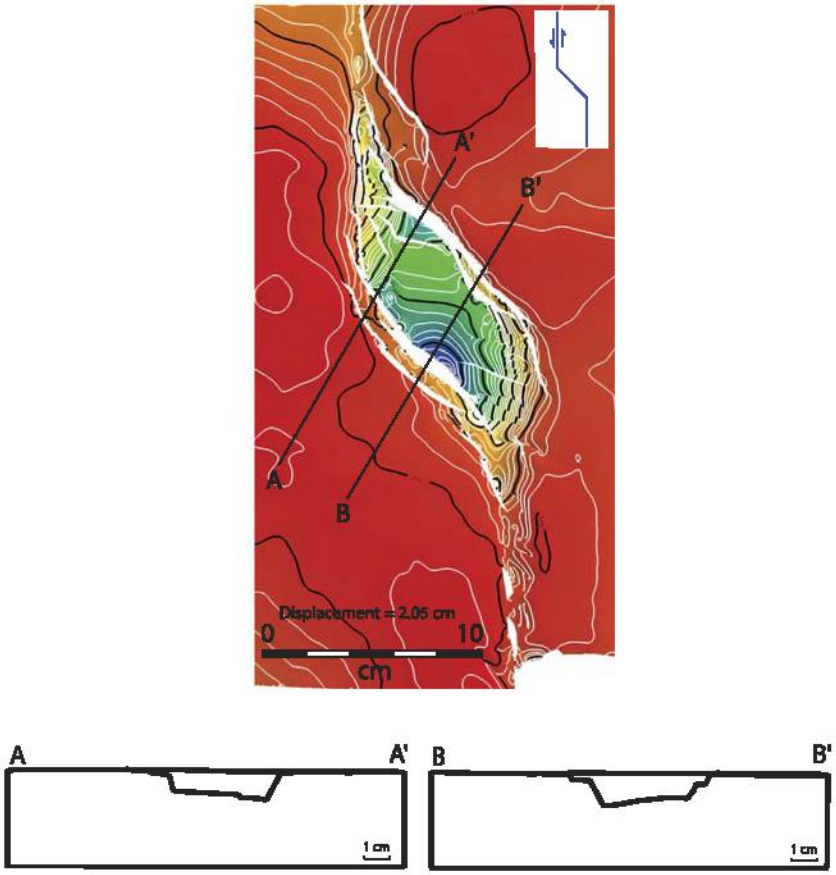

Figure 3. Analogue model of a releasing left step on a left lateral fault, from Mitra and Paul (2011). Contour map shows deformation at the surface after 2.05 cm of displacement, model dimensions are 30 x 15 cm. Dual depocenters form across the depression separated by an intrabasin high. Cross sections A-A' and B-B' show elevation rapidly drops across normal faults bounding the depression, fold deformation is broader, over several centimeters (Figure from Mitra and Paul, 2011).

3. Frazier Mountain Site

The FM site is located in a 100 x 500 m closed depression on a releasing step on the northwest end of the Mojave section of the San Andreas Fault (SAF) (Figure 1). The site is on the northern flank of Frazier Mountain, which consists mainly of Precambrian gneiss (Lindvall et al., 2002); locally the fault places middle Holocene to Pleistocene alluvium on the north against sandstone of the Pliocene Hungry Valley Formation on the south (Crowell, 1952; Duebendorfer, 1979; Lindvall et al., 2002). The margins of the depression are formed by prominent scarps on the northeast and southwest, and trenching reveals that these scarps are associated with older fault traces that do not offset deposits in the age range considered here (Figure 2). Faulting along the prominent northeast scarp (Figure 1b, yellow dashed lines) occurred more than 1,200 years ago (constrained by trenches across the older boundary on both sides of the depression, Figure 2), and since then slip has been concentrated across a narrower step in the fault. Younger cross-basin faults have formed within this narrow step and offset historic deposits, our network of trenches and CPT's are concentrated in this area (Figure 2). 34 paleoseismic trenches, plus additional cuts in key areas, excavated 3 to 9 meters below the ground surface, clearly show the main active trace of the San Andreas Fault right stepping 40 m over 150 m along strike, and producing two synclines that dramatically thicken the stratigraphic section (Figure 2). The fault generally produces an uphill facing scarp on the north flank of Frazier Mountain. This scarp essentially acts as a backstop and funnels sediment deposited by an active alluvial fan that bounds the west end of the closed depression (Figure 2), and is sourced by drainages along the north flank of Frazier Mountain. Paleoseismic trenches were located on the distal portion the alluvial fan, age dating from

these trenches yield an average sedimentation rate of ~0.01 m/year in the western part of the site.

Stratigraphic and structural relationships spanning the 40 m wide by 150 m long step-over, demonstrate progressive fold deformation across two depocenters separated by a low relief intra-basin high (Figure 2). Earthquakes rupturing through the site have repeatedly produced vertical relief of both sags on the surface and are subsequently infilled by alluvium and pond deposits (Figure 4, 5). The western syncline is both wider and deeper than the eastern syncline. The western syncline is roughly 30 meters wide and 70 meters long and records 5 earthquakes within a 5 meter thick section (Figure 6), whereas the eastern syncline is shorter, narrower and shallower. The Eastern Sag is 40 meters long, 10 meters wide, and here evidence for earthquake 5 is about 2.5 meters below the ground surface (Figure 7). Stratigraphy at the site is generally fine-grained, and dominated by alternating silt to organic-rich mud deposits interbedded with broadly tabular, massive, well-sorted, fine-grained sand layers (Figure 4, 5). These sand layers are laterally continuous and distinctive enough to confidently trace through the site. There is an abrupt transition to poorly sorted, gravelly sand capping the site in the last ~200 years (Figure 5).

4. Summary of Earthquakes at Frazier

The oldest earthquake structure contoured in this study, FM 5, generates folding in both the Eastern and Western Sags for deep stratigraphic units, 25 to 35 (Figure 6, 7). This event occurred while unit 24 was at the ground surface and has upward fault terminations extending into units 24 and 25. Units 23 and one lower unnumbered unit are

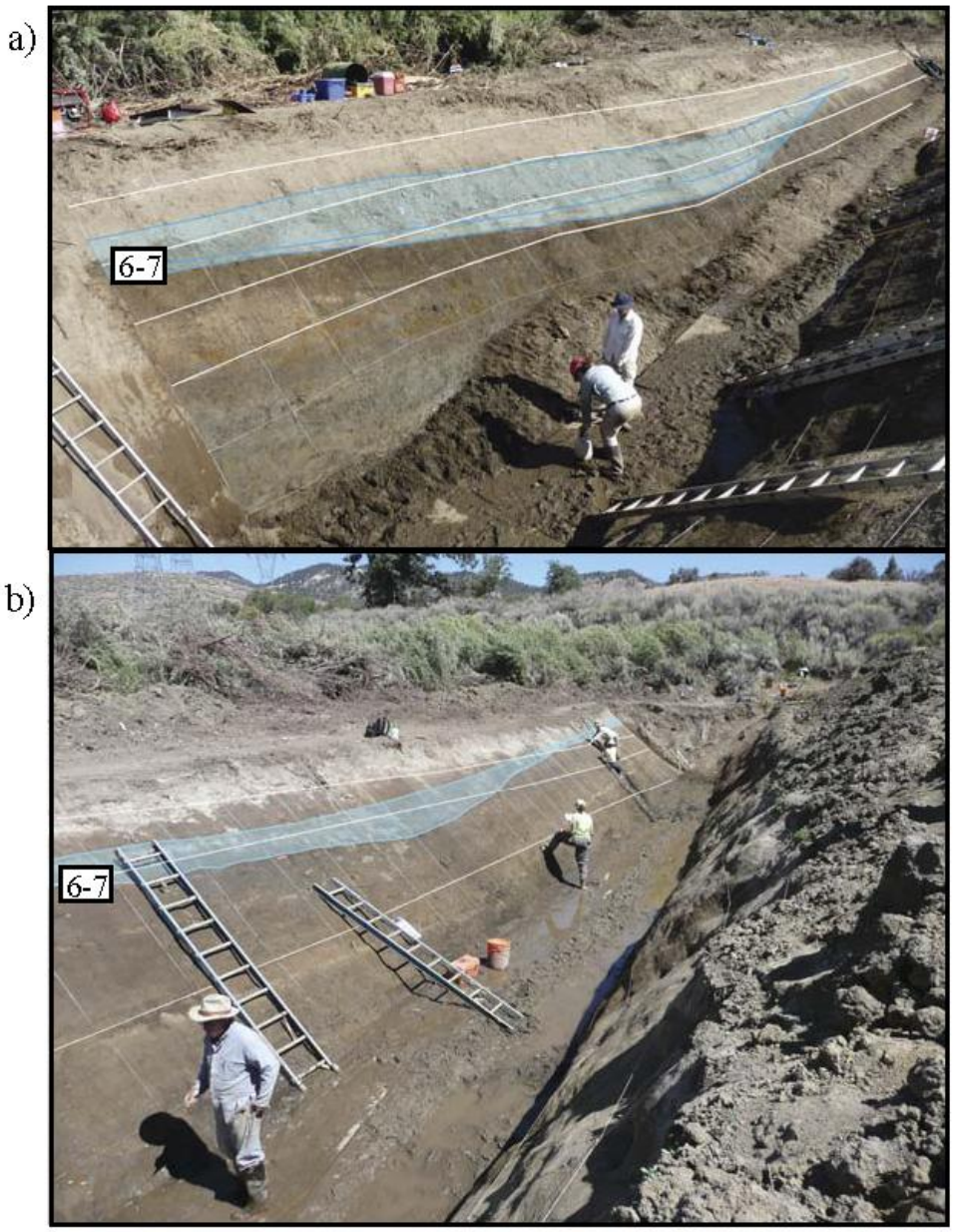

Figure 4. Photographs highlighting fold deformation. Units 5-7 are colored so the lower surface is the base of unit 7 and the upper surface is the base of unit 4 a course sand to gravel, shown as a blue polygon in both photos. (a) Photograph of trench T10 West wall, and (b) Trench T1 West wall, cut1. The base of unit 7 drops about ~1 meter from the outer edges of the fold limbs to the fold axis. Units 5-7 thickens in the fold axis, and are twice as thick in center of fold as the limbs of the fold. The top of the blue polygon is the base of Unit 4, folded in FM1. The base of the blue polygon, unit 7,is folded in two events, FM1 and FM2. Units 5-7 are thicker in T10 (a), the westernmost trench, which is closer to the sediment source than all other trenches. T1 (b) is ~15 m east of T10, and units 5-7 are noticeably thinner. [Note: The apparent warping of the white grid in the upper photos (T10E) is due to an irregular wall and the perspective of the photo; the grid is really horizontal and spaced 50 cm apart vertically.]

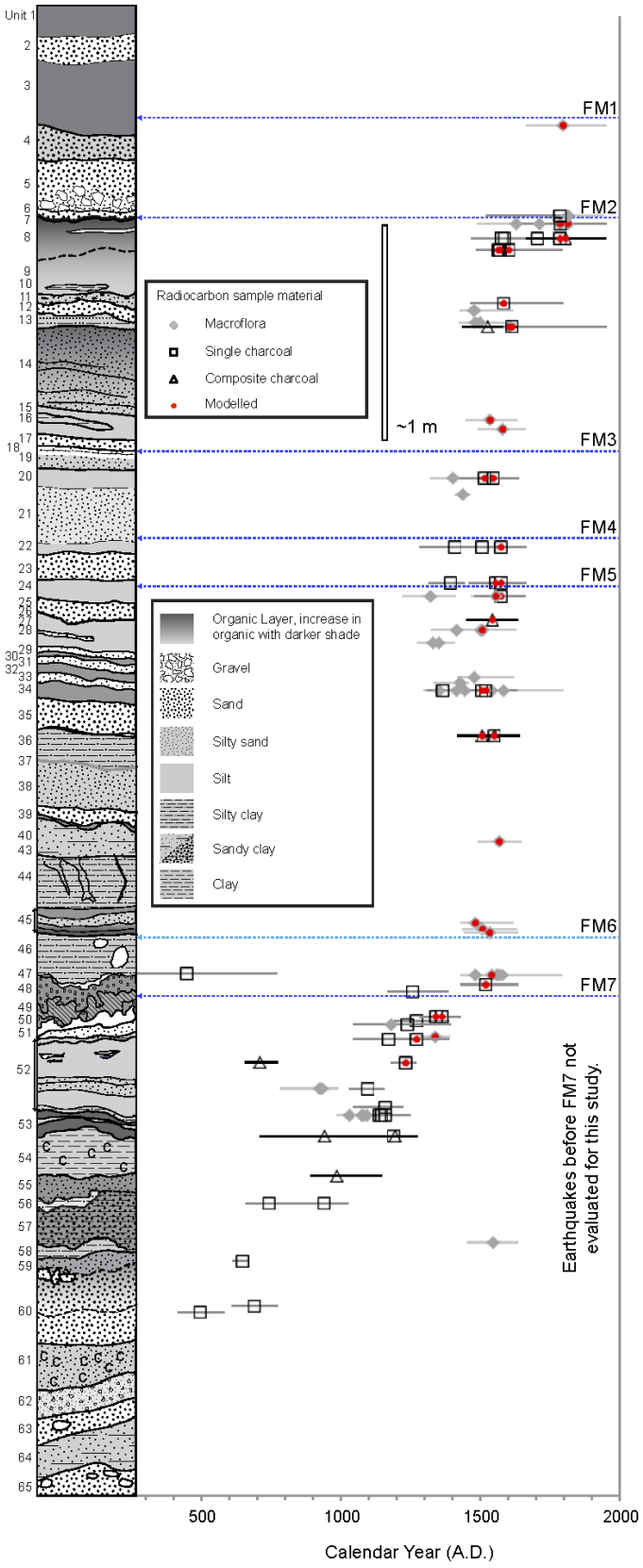

Figure 5. Stratigraphic column showing deposits, relative locations of dated radiocarbon samples and earthquake horizons at the Frazier Mountain site. Key to stratigraphic patterns, and explanation of radiocarbon sample material (i.e. charcoal, macrofossil etc.) shown on the right. Samples shown with red centers were stratigraphically consistent and retained in the site's age model (Dating results and the final OxCal model are included in Scharer et al., 2014).

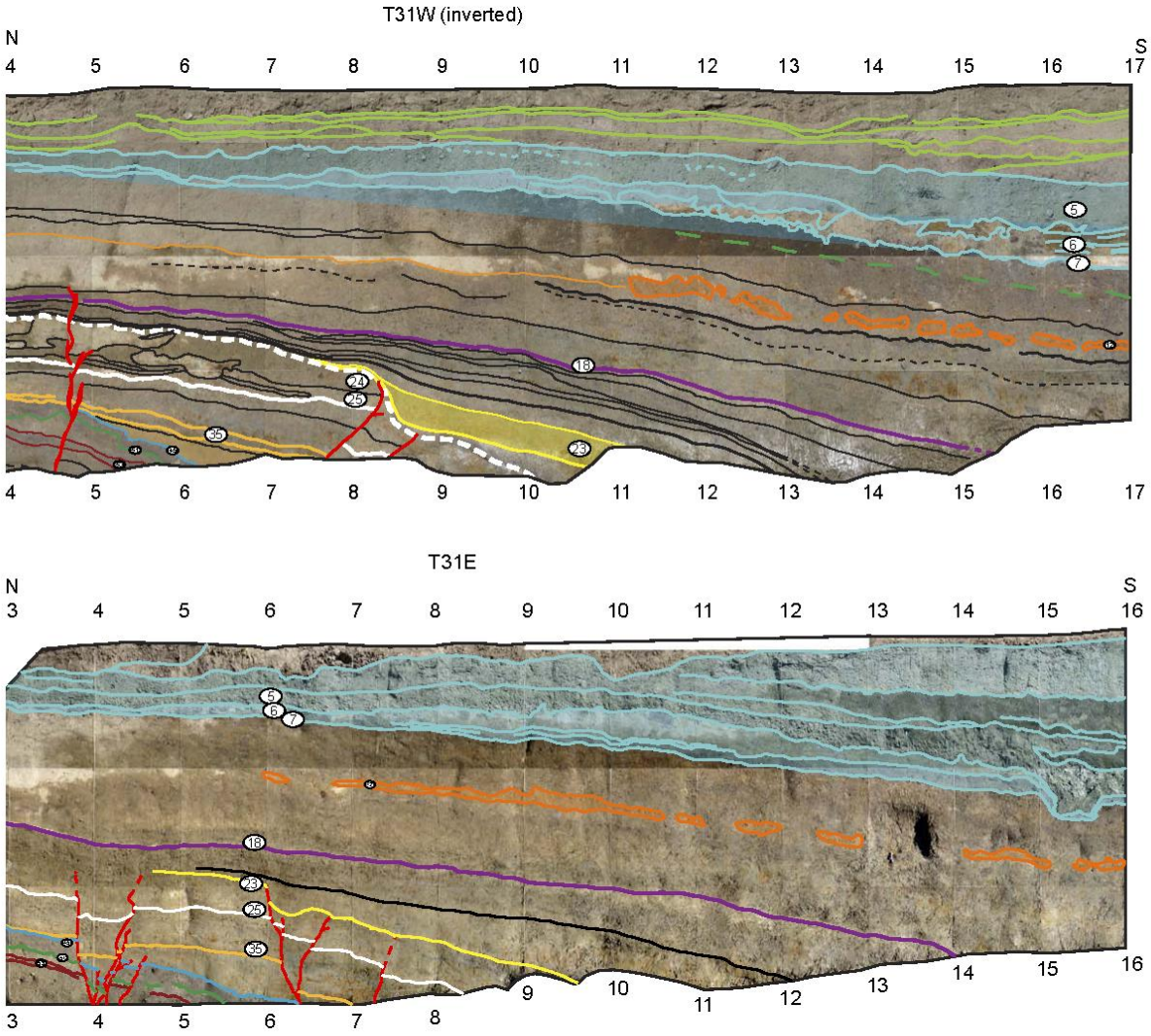

Figure 6. Photomosaiced trench logs from the Western Sag, for trench (a) T31W (west wall, inverted), and (b) T31E (east wall). Stratigraphic units are mapped as solid lines and shaded colored polygons. Sequences of sedimentation infilling relief from sag-deformation (folding) caused by earthquakes can be seen where units thicken from the northern margin of the step-over toward the south. Broad ~40 m wide, fairly symmetrical fold deformation is observed in the Western sag. (a) Trench T31W, the FM5 earthquake horizon is shown as a white dashed line below unit 23. Unit 23 is part of the growth strata sequence infilling vertical relief generated in earthquake FM5, and has infilled only ~ 1/3 to 1/2 the structural relief created by rupture across the step-over in that event. The base of unit 23 is lithologically distinct, and is laterally extensive between trenches, and is the most continuous unit between earthquakes FM4 and FM5 and so was used for the FM4 earthquake fold surface.

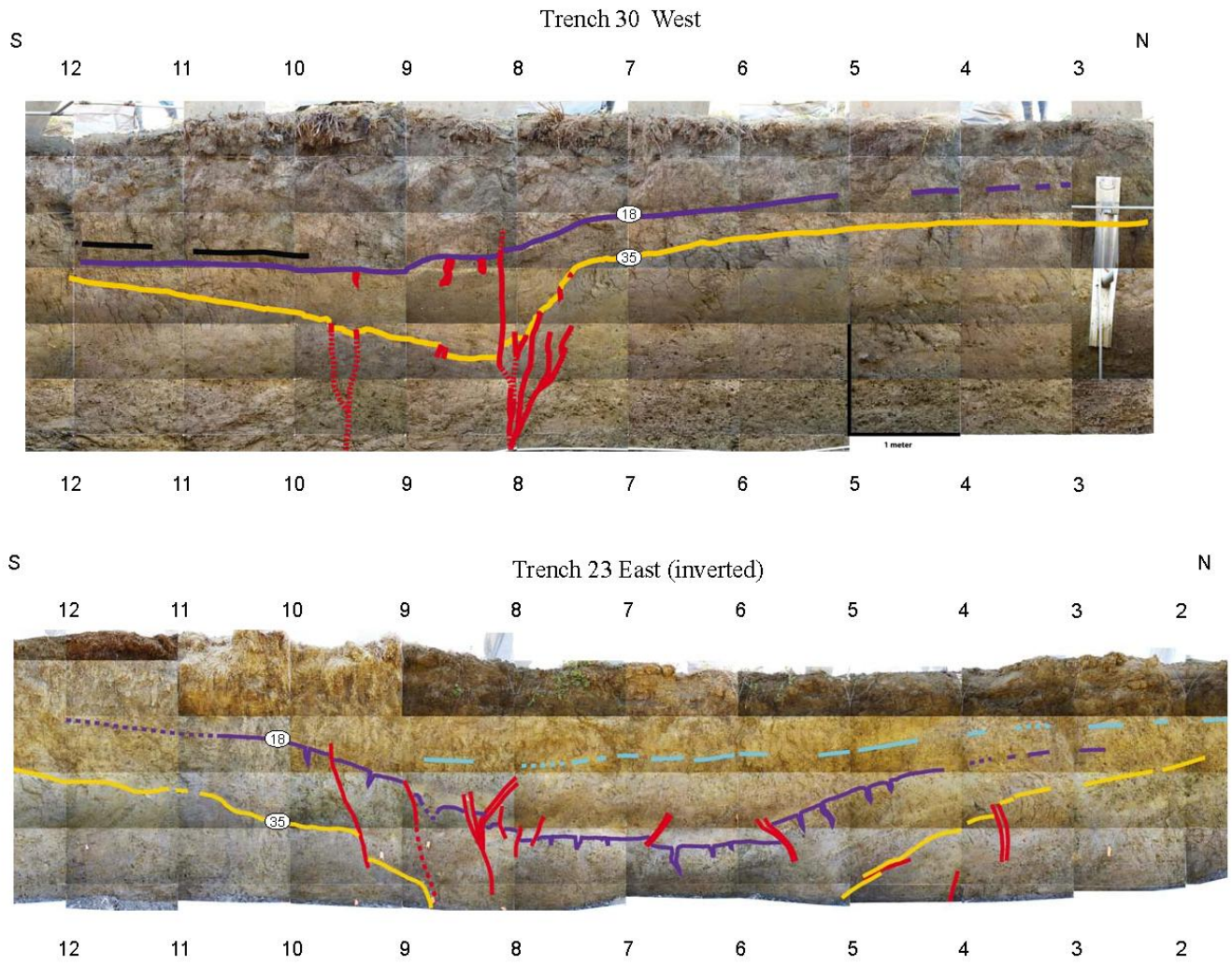

Figure 7. Photomosaiced trench logs from the smaller, Eastern Sag for trenches (a) T23 and (b) T30. Folding in the Eastern sag about 7 m wide, and asymmetrical across the synclinal fold axis to the east, shown in trench T23. Vertical relief is largely accommodated along the sag margins, the base of the sag is roughly flat bottomed to gently dipping.

growth strata that on-lap and partially infill vertical relief across faults and sagging generated in this earthquake (Figure 6). FM5 has an OxCal modeled 2σ age range of 1510 to 1572 (Scharer et al., 2014).

Earthquake FM4 offsets the base of unit 22 and unit 23, a well sorted sand, ~10 cm across a fault that trends roughly N50W through the center of the Western Sag, and documented in trenches T1 and T31 (Figure 5, 6). Unit 23 records all deformation in FM4, and because it is the upper portion of a sequence of growth strata deposited after the previous event (FM5) it also records some part of FM5 deformation. Vertical relief generated by the FM4 earthquake is largely infilled by unit 21 (observed in T1, unit not identified in T31). FM4 yielded a 2σ age range of 1540 to 1606 (Scharer et al., 2014). Unit 21 is not traceable through the site, so we chose to structure contour the more laterally continuous unit 23 to best approximate FM4 deformation.

Earthquake FM3 is distinct in both the Eastern and Western Sag, this earthquake generated small cracks and fissures on the order of a few centimeters wide and 10's of centimeters deep in unit 18, and extending downward into units 19 and 20 (Figure 5). Unit 18, a thin finely laminated clay bed, was at the ground surface at the time of FM3, and fissures and relief generated by this earthquake were subsequently filled with sand of unit 17 (Figure 5, 6, 7). A few faults exhibit vertical separation in FM3, but most vertical relief at this horizon is accommodated by fold deformation. FM3 has an OxCal modeled 2σ age range of A.D. 1563 to 1626. Units 5, 6 and 7 post-date earthquake FM2, and together are twice as thick in the center of the fold as in the limbs (Figure 4, 6). Units 6 and 7 are sand (6) and discontinuous 1-2 cm thick organic stringer (7), where it is present at the base of unit 6. Units 6-7 are the basal, fine-grained facies of a thick poorly sorted

gravelly sand, units 5 and 6 (Figure 4). FM2 caused significant folding, and units 5 and 6 filled the depression generated by this event. FM2 has a 2σ OxCal modeled age range of 1733 – 1854, and could be the historic 1812 earthquake. FM 1 postdates unit 4, a silty sand, and occurred within unit 3, an organic silt. Silt and sand deposits, units 1 and 2, overlie unit 3 and are not involved in any earthquakes (Figure 5). FM1 is the historic 1857 M7.9 SAF earthquake that extended from Parkfield at the north (the northern end of Figure 1), south to the junction with the San Jacinto Fault (Figure 1).

5. Methods

5.1. Paleoseismology and Surveying

We excavated a combination of vertical slot trenches in the upper 2 -3 meters, and 'V' trenches with ~ 30° sloped walls from the surface or below 'boxes' cut into the previously trenched upper 2 – 3 meters in 2007, 2009, 2010, 2011 and 2012 (Figure 2). Trench exposures were cleaned, and gridded with a string and nail grid, and photographed. Grids in slotted trenches on vertical benches were 1 m x 0.5 m (horizontal x vertical), and larger 'V' trenches were gridded with 1 m x 0.65 or 1.3 m grids (horizontal x face perpendicular; Figure 4) to account for the slope of the trench wall; this allows us to plot photomosiac logs to a 1 x 0.5 or 1m grid when projected onto a vertical plane. All trench exposures were logged on a printed photo mosaic of high-resolution digital photographs at a scale of roughly 1:10. Stratigraphic units and structural relationships were documented and described on photo logs.

We surveyed trench edges, trench grids, the base of every unit that was thick enough or laterally extensive enough to correlate between trenches, faults, fissures and

other ground shaking related features exposed in each trench, and surveyed or hand measured small cut-backs into primary trench walls during each field season. We usied a Leica total station, and installed a network of benchmarks the first and second years of the study to place all surveys in a common reference frame, and merge data sets for five investigation years. Horizontal uncertainties between survey years are less than 5 cm for surveys in 2010, 2011 and 2012, with horizontal errors less than ~10 cm for surveys in the years 2007 and 2009. We surveyed the benchmarks and some trench locations with a differential GPS unit (Trimble GeoXH), and used these coordinates to translate and rotate total station survey data in a Cartesian coordinate system to WGS 84 UTM zone 11N projection. GPS positions were post processed using Trimble Pathfinder software and a network of permanent GPS base stations to reduce position uncertainty.

During 2007 only trench grids were surveyed using a differential GPS unit, so 3D locations of points on stratigraphic units were measured from photomosaic logs in the lab. These measurements are internally consistent, i.e. there is less than 5 cm of relative uncertainty between stratigraphic points measured this way. However, absolute position uncertainty in this survey stems from the original vertical and horizontal uncertainties from post processed differential GPS coordinates (on the order of ~5-10 cm horizontal, and ~15 cm vertical). We reduced horizontal and vertical uncertainties for these grid coordinates by re-surveying nails from the 2007 investigation with a total station in successive years, with uncertainties on total station positions of less than 5 cm (and often sub-centimeter), and made appropriate minor adjustments to the 2007 survey. Only trench grid locations were surveyed with the total station during the 2009 field

investigation, so we measured key stratigraphic units on photomosaic trench logs, placed into the site reference frame using the surveyed string grid.

5.2. Cone Penetrometer Test Transects

We used Cone Penetrometer Tests (CPT) transects to laterally extend observations of key stratigraphic units identified in the upper ~8 meters of section in excavations, and to see how deformation changed with depth below our excavations. CPT's were carried out by Gregg Drilling and Testing, Inc. using a 25-ton CPT rig with a 15 cm^2 piezocone (cone number GDC-36), and data was recorded at 5 cm intervals down to about 20 meters on average. The data were collected on August 15 – 16, 2011, and named "FRAZIER MOUNTAIN SITE – Job 600". Raw data and calibration specifics are available from Gregg Drilling or the authors of this interpretation . The CPT rig recorded; Depth, Tip Pressure, Sleeve Pressure, Pore Fluid Pressure, Tilt X, Tilt Y, UVIF (Ultraviolet Induced Fluorescence), Resistivity, and Temperature.

The network of CPT's were designed to first extend between pre-existing trenches 1 to 10, along the margin of the large sag, CPT line 1. Lines 2, 3, 4 and 6 connect orthogonal lines across the projection of the syncline that defines the sag (Figure 2). A few of the CPT transects were located directly within existing trench footprints (Figure 2), and some CPT measurements were located on undisturbed ground and trenches were subsequently excavated that field season, 2011, and the following year, 2012. Thus we are able to directly compare sedimentary units in the upper 5 m of section with the CPT data and use these correlations to map stratigraphic units between CPT's across the rest of the network.

For analysis we used normalized tip resistance (Qc), normalized friction ratio (Fr), and a soil behavior type chart (SBT, based on Olsen, 1988; produced by the Gregg Drilling with propriety software). An example of Qc, Fr, and SBT are shown for Line 2, with interpreted correlations (Figure 8). It is important to note that it is often impossible to follow units with any single parameter (such as Qc or Fr); to go from CPT site to CPT site requires looking at all three together because one or more might not be obviously correlatable. Major lithologic contrasts were initially correlated simply from the CPT logs, as shown in Line 2 (Figure 8). The CPT interpreted elevation of a unit might be somewhat different (a few cm) from the unit elevations known from surveyed trenches, because we chose spikes in the Qc and Fr plots that were correlatable between CPT's and best represented each key stratigraphic layer. We took the depths of key layers, units 6, 18, 23, and 35, and identified which features in the CPT logs best represented the top and bottom of the stratigraphic units known from trenches. We did this independent of trench results and only compared the two techniques once initial CPT stratigraphic picks were complete (Figure 8). We compared the depth of CPT line 2 lithologic picks with unit elevations from logs for trenches 31 and 32 that were excavated subsequent to the CPT investigation, and found that they agree well. We then chose depths from the CPT

Figure 8. (next page) CPT plots for Line 2 showing (a) normalized cone resistance (Qc), (b) Friction ratio (Fr) plotted with Qc, (c) soil behavior type (SBT, after Olsen, 1988). Location of Line 2 is shown on figure 2, CPT's are individually numbered 2.0 through 2.9 from southwest to northeast. CPT correlations are based on Qc, Fr and SBT. Fr and Qc are plotted together in (b) to highlight how the two measurements are combined to interpret both the coarse-grained units (sands) with Qc and fine-grained (slit and clay) with Fr measurements. At the FM site, broad correlations are most easily seen in SBT (c), where major sections interpreted as sand, can be traced between sites. At the finest scale, mapping individual units, Fr, (b), correlates best because the variations are higher frequency than Qc and SBT, but are clearly correlatable to the broader variations seen in Qc, (a), which provides a bridge between SBT and Fr results.

a) Cone Resistance (Qc)

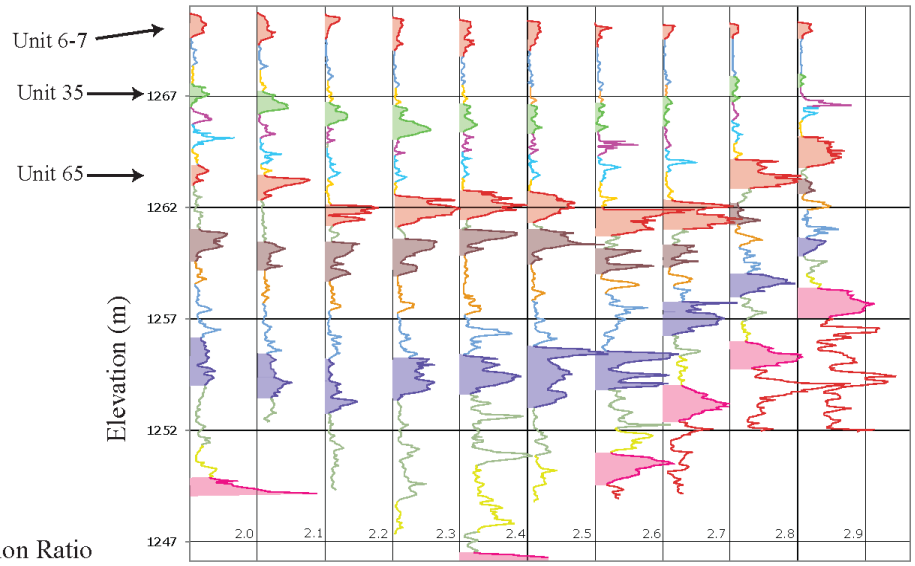

b) Normalized Friction Ratio (Fr) & Cone Resistance (Qc)

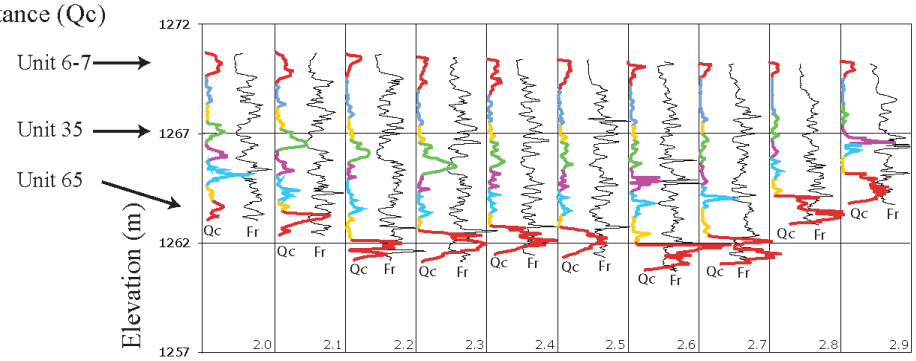

c) Soil behavior type (SBT)

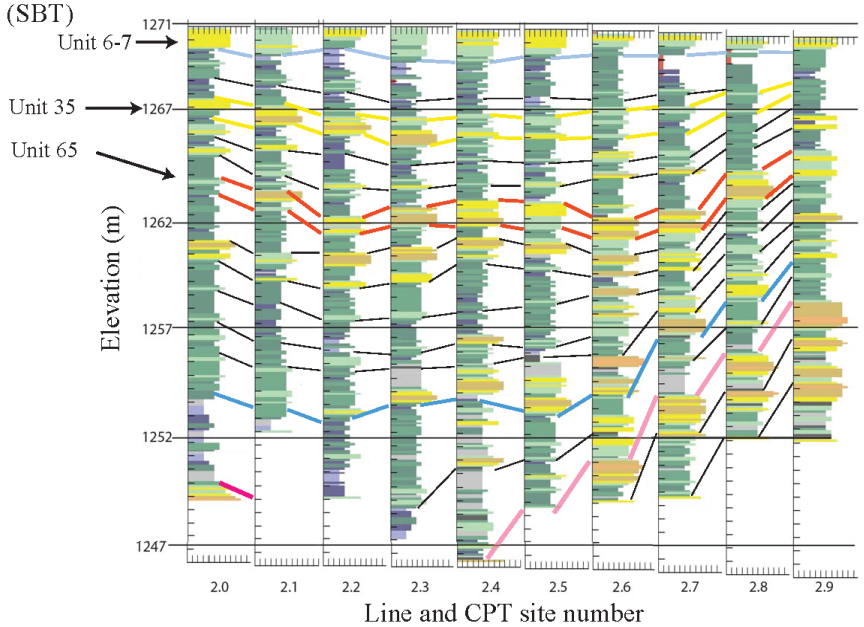

correlations for all five stratigraphic units considered in this study (except where CPT's encountered fill), and incorporated these unit elevations in our 3D point data base spanning the Western Sag.

The upper 5 meters of CPT 2.0 shows a sand layer (Figure 8c, yellow block on the interpretive soil chart) is associated with high cone resistance and low friction ratio (Figure 8a, b). Subsequent trenching (trenches 31 and 32) revealed that the "sand" near the top of CPT 2.0 (elevation 1270) is our stratigraphic unit 6, and the sand at elevation 1267 is unit 35, the two coarsest units in the upper part of the section at the site. Records from CPT transect 2.0 to 2.9 highlight progressive fold deformation with depth, where unit 35, deformed in 5 earthquakes, descends as the CPT transect extends to the northeast into the sag; whereas the stratigraphically higher unit 6 remains at about the same elevation because this unit only records 2 earthquakes. We identify the deepest stratigraphic unit exposed in trenches, unit 65 (Figure 5), and find it has more vertical relief across CPT transect 2.0 to 2.9 than stratigraphically higher units, like unit 35 (Figure 8a, b). In addition, similar layered sediments extend at least 3 times deeper than we have currently exposed in trenches. These deeper layers have steeper dips and are more deformed than the upper section exposed in trenches, especially at the northern margin of the sag. Some of the deeper units near elevations 1261, 1256, and 1250 m appear to be sand layers like the key marker units in the upper stratigraphic section (Figure 8a). The CPT correlations reveal that with deep enough excavations we could work out a much longer earthquake chronology at the FM site.

5.3. Data Compilation

We generate structure contour surfaces for the base of units, 4, 6-7, 18, 23 and 35 to represent deformation in events FM1through FM5 respectively. We compile data for unit 35 for FM5 structure contouring because it is the most distinct and extensive stratigraphic unit between the FM4 and FM5 earthquake horizons, and was widely surveyed in the field. However, unit 35 is 10 stratigraphic units below the FM5 event horizon, the greatest stratigraphic distance from the surface of interest of all the units evaluated here. Unit 35 is high in the stratigraphic section above FM6, separated by 10 older stratigraphic units (units 45 to 36) that appear to completely infill structural relief generated by earthquake FM6 (Figure 8). Future work will involve carefully measuring and compiling unit 25 from trench logs, to better bracket the FM5 event horizon. This unit is less distinct and was difficult to correlate between trenches while in the field, but should be possible if the unit was identified and logged in all exposures by comparing photomosaic logs and stratigraphic sections side by side. This additional step may help us more carefully separate deformation associated with FM5 from FM6, and test whether there is an additional event between FM5 and FM6.

Because stratigraphic units thin and taper out of the sags we locally employed a pinch out rule to extend observations of units based on the presence of their conformable basal contact with underlying stratigraphy. We used this rule where trench logs show stratigraphic relationships, but we lack survey data for a unit. The resulting 3D point data reflect observed tapering relationship of the deposits, and the margins of the deposits don’t abruptly end. We also added zero values where units pinch out to place a hard sedimentary boundary on the sag-filling shape of the deposits. These steps minimize edge

effects on interpolated surfaces and contours of the stratigraphic surface data. We added CPT-inferred depths for units 6, 18, 23 and 35 to the compiled stratigraphic trench survey data.

6. 3D Structural Analysis

We plot elevations of the stratigraphic horizons to portray the density and areal data coverage for each surface (Figure 9). We interpolate a surface through these elevations; this surface reflects deformation for all earthquakes a unit has experienced and to varying extents unfilled deformation from the earthquake below. Stratigraphic survey points do not directly overlie each other, so, to retrodeform sag filling deposits, we must either subtract one surface from another, or subtract the points for a given event from a surface fit to another set of points. The latter produces the least interpreted and most artifact-free results. We tried progressively retrodeforming interpolated surfaces earthquake by earthquake, but found small variations in each retrodeformation step compound, producing artifacts in multiply deformed surfaces. We difference the point data for each earthquake surface from an interpolated surface for the previous earthquake to isolate the folding for each earthquake horizon. For example, if we want to evaluate vertical relief generated in FM3 we difference the point data for unit 18 from the 'total deformation'

Figure 9. (next page) Elevation of stratigraphic point data where warm colors are high elevations and blue are lower (left column) and retrodeformed surfaces (right column) for unit 4 (a)(b), unit 6-7 (c)(d), unit 18 (e)(f), unit 23 (g)(h) and unit 35 (i)(j). 1 m color ramp in the right column for all surfaces, where 0 m relief is shown as red and equals no change in surface position (elevation), and increased vertical sagging shown as increasingly cool colors, where 1 m+ of vertical deformation is shown as dark blue. Thin black lines on surfaces are 25 cm contours. Profile locations for Figure 11 are shown on all surfaces as A-A', etc.

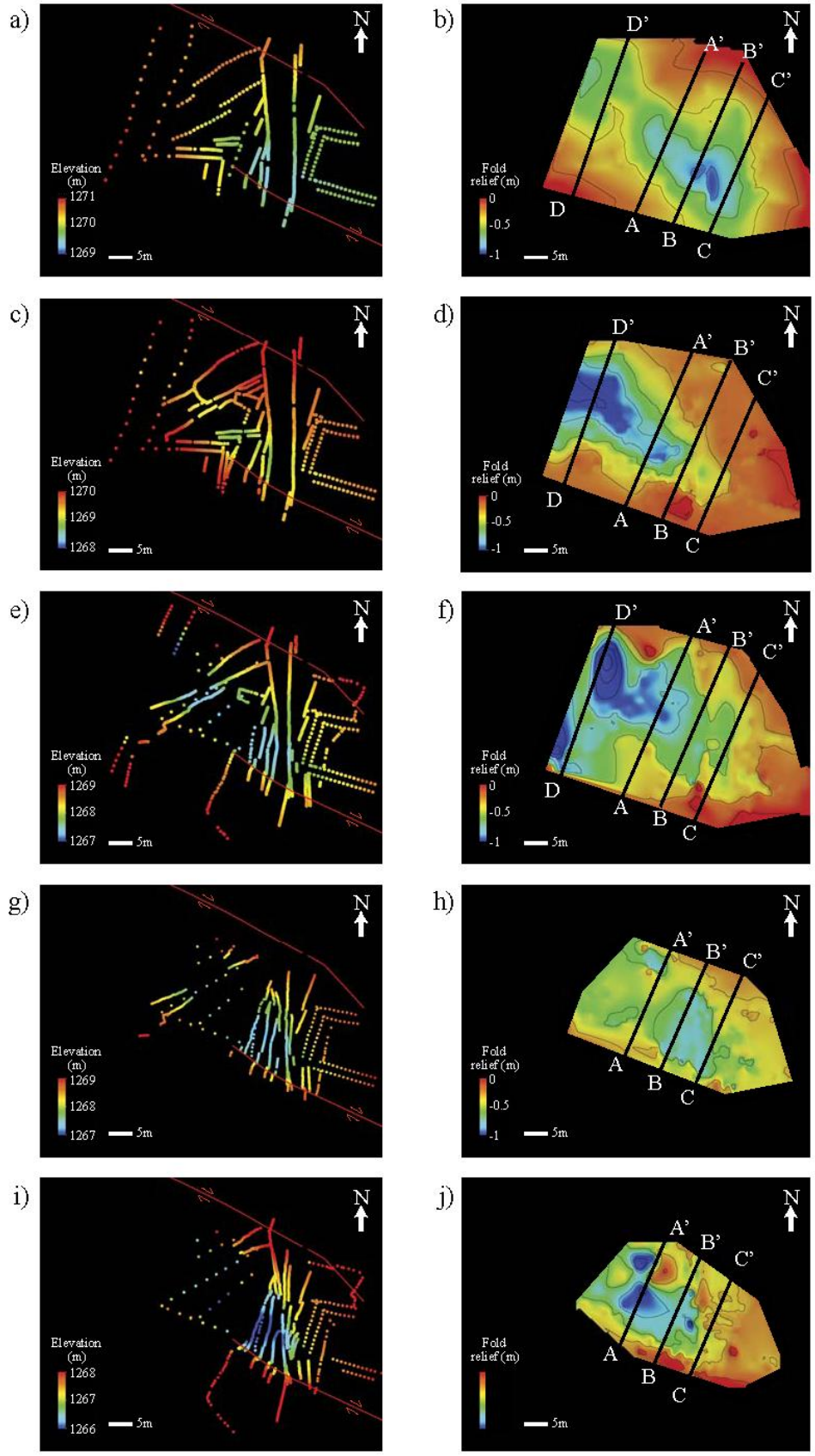
a)
N
Elevation (m)
1271
1270
1269
5m
b)
D'
A'
B'
C'
N
Fold relief (m)
0
-0.5
-1
5m
D
A
B
C
c)
N
Elevation (m)
1270
1269
1268
5m
d)
D'
A'
B'
C'
N
Fold relief (m)
0
-0.5
-1
5m
D
A
B
C
e)
N
Elevation (m)
1269
1268
1267
5m
f)
D'
A'
B'
C'
N
Fold relief (m)
0
-0.5
-1
5m
D
A
B
C
g)
N
Elevation (m)
1269
1268
1267
5m
h)
A'
B'
C'
N
Fold relief (m)
0
-0.5
-1
5m
A
B
C
i)
N
Elevation (m)
1268
1267
1266
5m
j)
A'
B'
C'
N
Fold relief (m)
5m
A
B
C

surface for unit 7 that is deformed by earthquakes FM1 and 2, but is inferred to postdate complete infilling of relief generated by earthquake FM3. Differencing earthquake surfaces isolates folding in each event, and also largely removes the depositional gradient for these low energy distal alluvial deposits. This is because the deposits are lithologically similar, have the same alluvial sediment source on the western margin of the step-over, and the units are all generally fine-grained depression filling deposits, and so have similar trends and ranges of surface gradients. The differenced points have values ranging from 0 (i.e. no change) to negative values (reflecting downward change). Surfaces interpolated from these differenced points reflect sag deformation for FM1, FM2 and FM3 (Figure 9).

Our calculated sag deformation for FM4 is a maximum, because unit 23 also reflects some fraction of FM5 vertical relief. Unit 23 predates FM4, so the base of the unit records all deformation in that earthquake. However, stratigraphic relationships in trenches reveal that unit 23 is not the top of the growth strata sequence after FM5, infills only about a third to half the relief generated in that event, and thus has some residual vertical relief from the partial infilling after FM5 (Figure 6). The difference between the surface for unit 23 and points for unit 35 captures event FM5 minus a fraction of relict FM5 relief that was not completely infilled by growth strata, and was still expressed in the topography when unit 23 was deposited. Thus our calculated deformation for FM5 is a minimum.

As noted above we remove the depositional surface gradient from each folded surface by subtracting out the overlying earthquake surface, which is inferred to contain ~ the same surface gradient in addition to the earthquake deformation. However, for FM1,

there is no overlying earthquake surface to subtract and remove the depositional surface gradient. Figure 10a shows this is a significant problem because the entire east side, beyond the sag, is lower than the west side where the sediments are sourced (Figure 10a). In Figure 10b and c we difference unit 4 from the modern ground surface, and find that subtracting the modern ground surface from unit 4 (FM1) overcorrects for surface gradient, creates a topographic low centered at the western margin of the site (Figure 10c), and no change or sagging across the rest of the site (Figure 10c); which is unrealistic based on trench exposures.

This problem is additionally complicated because we interpret unit 5, a gravelly sand deposit, to reflect anthromorphic changes in the landscape. This unit has both atypical grain size and upper surface slope compared to other deposits filling the depression. We also know from trench exposures that units 5, 6 and 7 do not completely infill relief generated by earthquake FM2. If a stratigraphic unit has completely infilled vertical relief caused by an earthquake then the deposit should be thickest in the center of the fold, the locus of folding. However, trench and CPT data show that the gravel and sands of unit 5, 6 and 7 are thickest on the western margin of our study, high on the alluvial fan deposits bounding the western edge of the depression and nearest the sediment source. The modern ground surface is not a good proxy for the surface gradient of these deposits.

Second, we fit a first order linear regression to 5 data points to represent the slope of the top of unit 4 (Figure 10). These points are located away from the fault and syncline, and reflect the average surface gradient of the unit in areas that are undeformed by earthquake FM1. The points span the apex of the alluvial fan on the western margin of

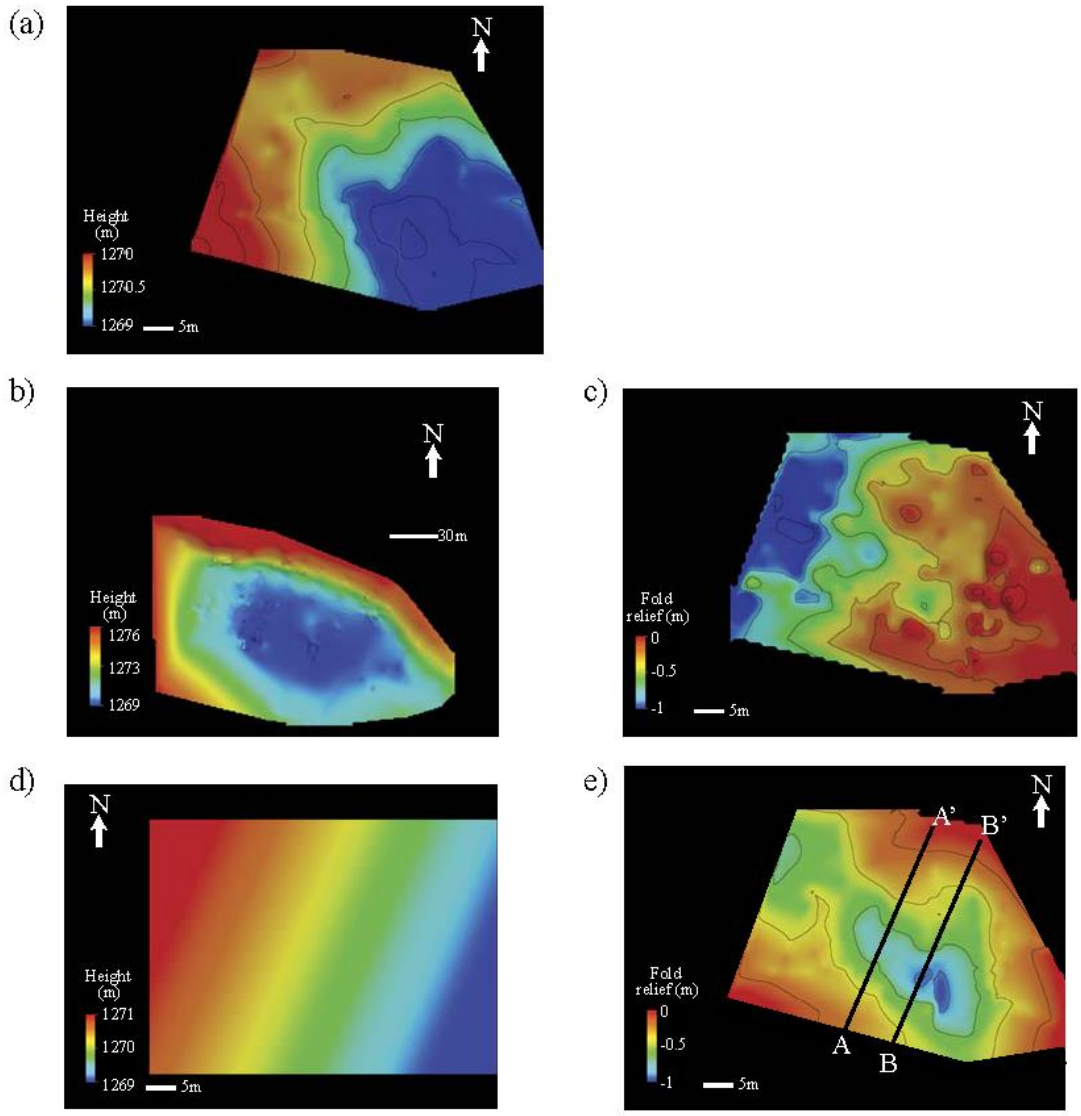

Figure 10. Figures illustrating steps to remove surface gradient and isolate FM1 sag deformation. (a) interpolated surface for the base of unit 4, (b) interpolated ground surface from dense survey data (control ground points and tops of trenches). (c) Surface interpolated for unit 4 stratigraphic points minus the interpolated ground surface in (b). (d) First order linear regression to fit 5 points on the margins of the data set from unit 4 defining the general slope of the top of the gravel across the Western sag. (e) FM1 fold deformation. Surface interpolated for unit 4 points minus (d).

the depression to the easternmost edges of the site (Figure 10d). Figure 10e shows that differencing unit 4 points from the slope calculated in this way tilts unit 4 downward on

the west, does not overcorrect for surface gradient in the eastern part of the site, and better reflects fold deformation observed across the Western Sag (Figure 10e).

In the remainder of this study I refer to the resulting retrodeformed and gradient corrected surfaces by the earthquake these surfaces represent. To summarize; FM1 is represented by the base of unit 4 and is corrected for depositional surface gradient. FM2 is the base of units 6 and 7 minus unit 4. FM3 is the base of unit 18 minus units 6 and 7. FM4 is the base of unit 23 minus unit 18, this however includes some fraction of vertical relief associate with FM5. FM5 is represented by the base of unit 35 minus the base of unit 23, but underestimates deformation in FM5 because some fraction of FM5 deformation is included in unit 23.

7. Results

FM1, 2, 3 and 5 have 70, 83, 85 and 80 cm of structural relief across the sag respectively, and the values for FM5 are a minimum. FM4 has 47 cm vertical relief at its greatest depth, this is a maximum value of structural relief, since unit 23 also captures a fraction of FM5 deformation. A correction can be made between FM4 and FM5 estimates to better represent deformation in each of these earthquakes. We know from trench exposures that unit 23 infills roughly the upper 1/3 to 1/2 of relict relief from FM5 (Figure 6), so the maximum depth value of 47 cm of vertical relief in FM4 (Figure 9h) can be divided by 2 to yield ~ 24 cm of structural relief in FM4, and is a better estimate for this event. We can add the remaining 24 cm to the FM5 value of 80 cm of structural relief across the sag, totaling over 1 m of vertical relief in earthquake FM5. We can see in Figure 9h that structural relief for the uncorrected FM4 surface is not as pronounced, or

sharp on the step-over margins as the other earthquake surfaces (Figure 9). Reducing vertical relief by half would make the FM4 surface even more gently folded, and strikingly dissimilar to the amount of vertical relief generated in the other four earthquakes.

Profiles of the earthquake surfaces however, reveal that all five earthquakes have similar shapes, and the greatest amount of vertical relief for each earthquake is accommodated on the step-over margins by both fault and fold deformation (Figure 11). Points shown in Figure 11 for A-A' through D-D' are the elevation every 25 cm for a 2 m wide swath centered on the profile lines (profile locations shown in Figure 9). Lines drawn through the points for A-A' through D-D' reflect the average elevation for each cross-section swath (Figure 12). Profile D-D' only includes data from shallower earthquake surfaces that were exposed in the westernmost trenches, there is no trench data for units 23 and 35 (FM 4 and 5) this far west, and along this profile line. We compare the shape and geometry of structural relief generated in an earthquake for all five earthquake surfaces by stacking the profiles (Figure 13). We shift the profiles, and rotate some slightly so the southern syncline margins align (Figure 13). These stacks reveal that the southern margin of the sag is relatively steep and accommodates the greatest amount of vertical relief over a very short distance (about 5 to 7 meters along the profile) for all five surfaces (Figure 13). In general, in the area we have excavated, the northern margin of the syncline is less steep than the south margin, elevations gradually

---

Figure 11. (next 2 pages) Profiles showing vertical relief across all five surfaces, for a 2m swath centered on profile lines. Profile locations are shown on Figure 9, (a)A-A', (b) B-B', (c) C-C' and (d) D-D'. Profile D-D' is only compared for shallower surfaces that were exposed in the westernmost trenches; no trench data exist for units 23 and 35 in that area.

(a)

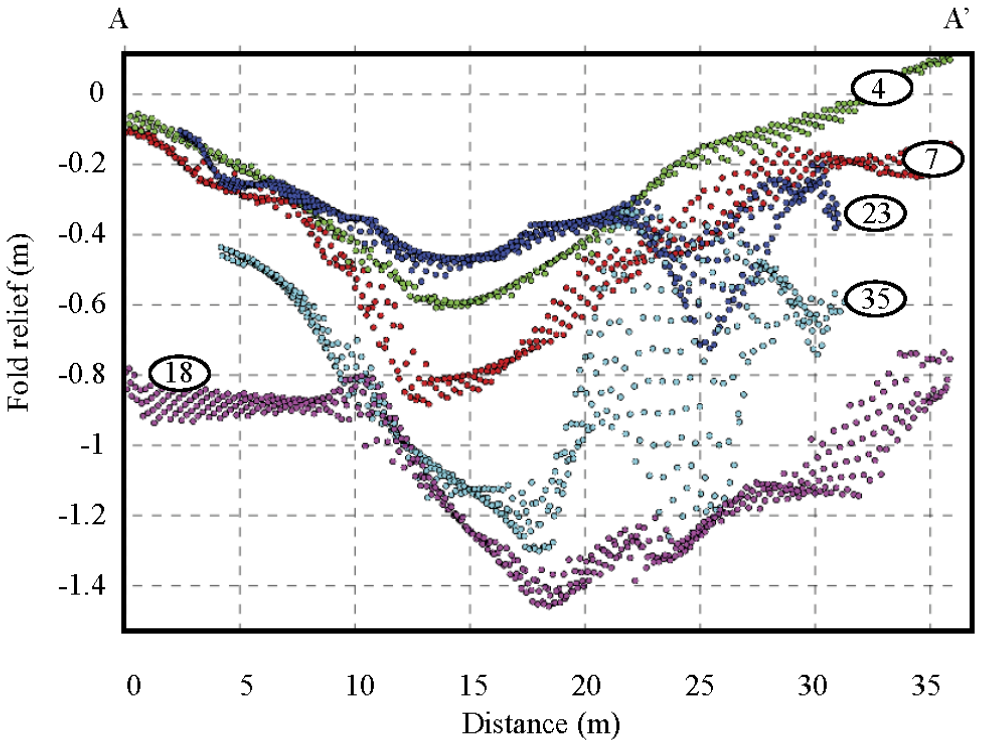
A
A'
0
-0.2
-0.4
-0.6
-0.8
-1
-1.2
-1.4
Fold relief (m)
4
7
23
35
18
0
5
10
15
20
25
30
35
Distance (m)

(b)

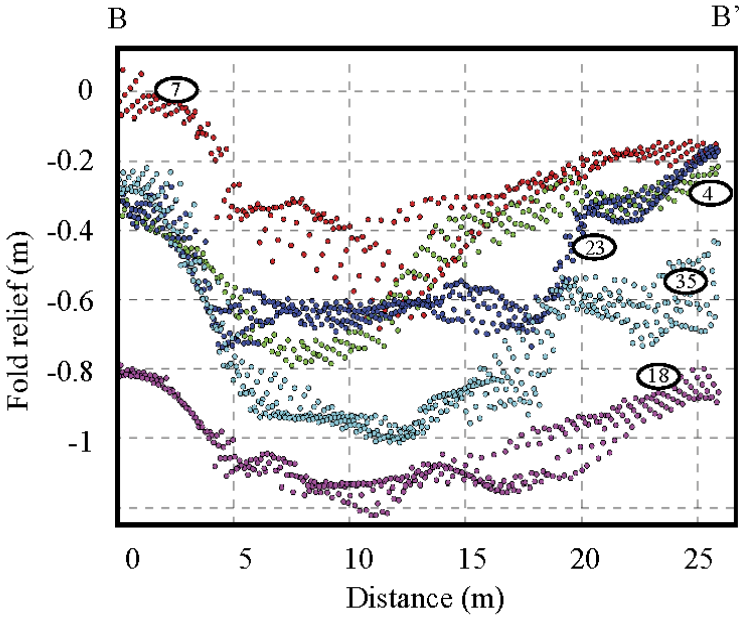
B
B'
0
-0.2
-0.4
-0.6
-0.8
-1
Fold relief (m)
7
4
23
35
18
0
5
10
15
20
25
Distance (m)

(c)

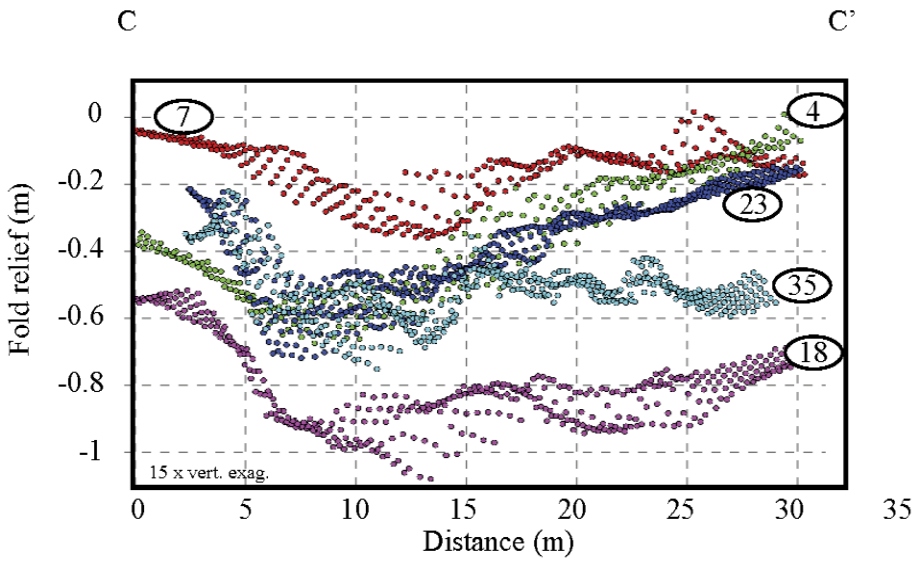
C
C'
7
4
23
35
18
0
-0.2
-0.4
-0.6
-0.8
-1
Fold relief (m)
15 x vert. exag.
0
5
10
15
20
25
30
35
Distance (m)

(d)

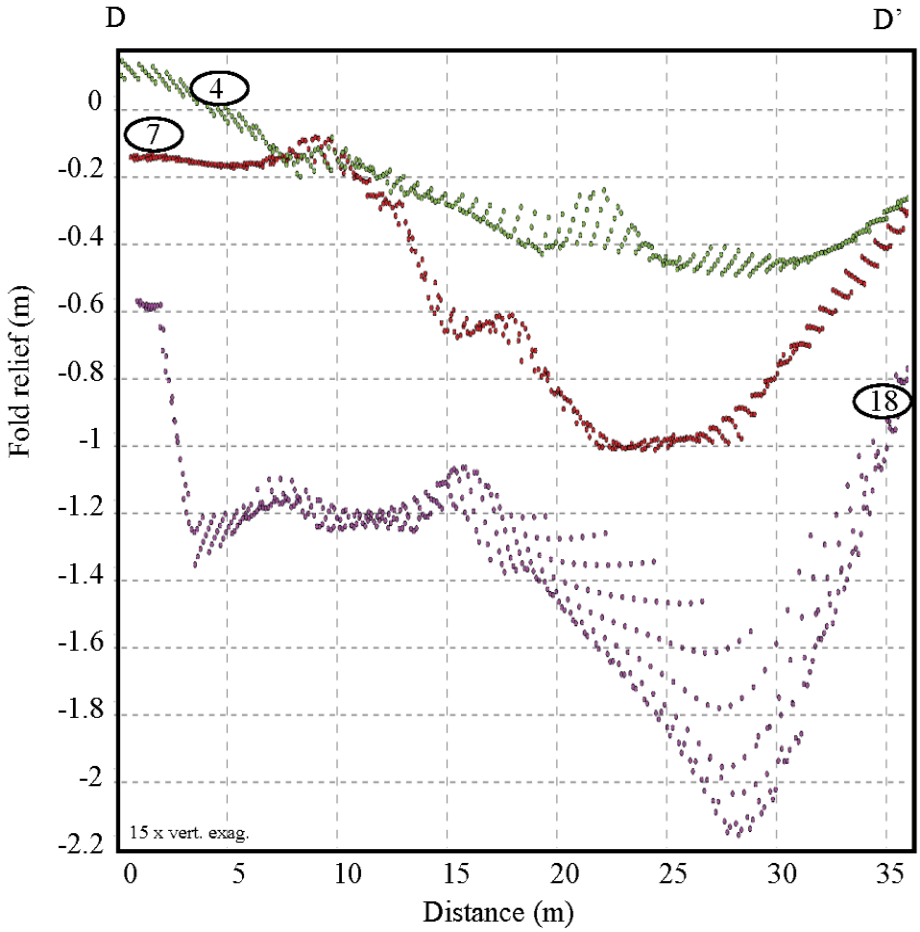
D
D'
4
7
18
0
-0.2
-0.4
-0.6
-0.8
-1
-1.2
-1.4
-1.6
-1.8
-2
-2.2
Fold relief (m)
15 x vert. exag.
0
5
10
15
20
25
30
35
Distance (m)

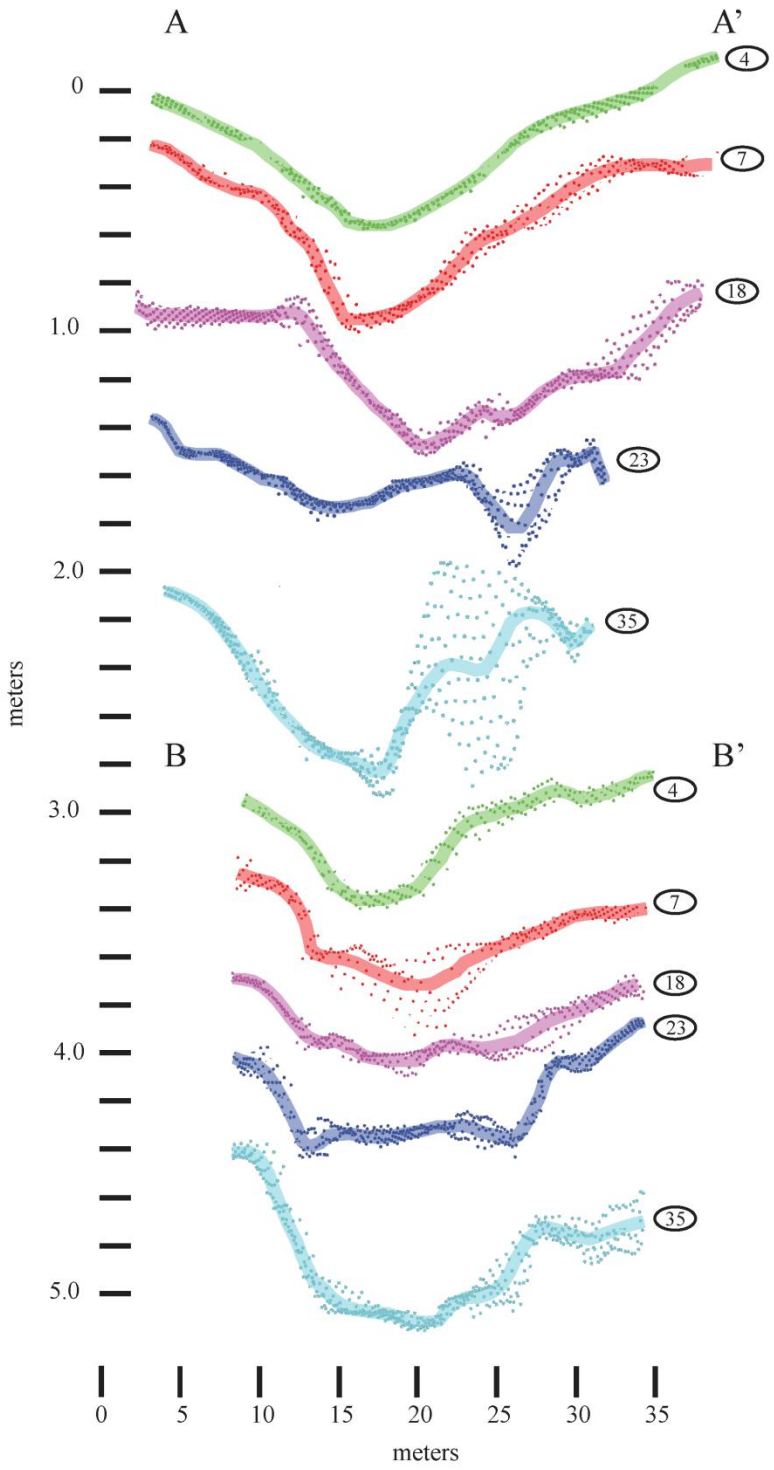

Figure 12. Trend lines drawn through swath point data for stratigraphic surfaces (units) shown in Figure 1, for profiles A-A'and B-B'.

rise over 10 to 15 m distance to the north edge of the step-over in all four profiles (Figure 13). The floor of the syncline is roughly flat bottomed to gently dipping in profiles B-B' and C-C', and is remarkably similar to profiles for the scaled analog clay-cake model shown in Mitra and Paul (2011; Figure 3). Profile D-D' does not include all 5 surfaces,

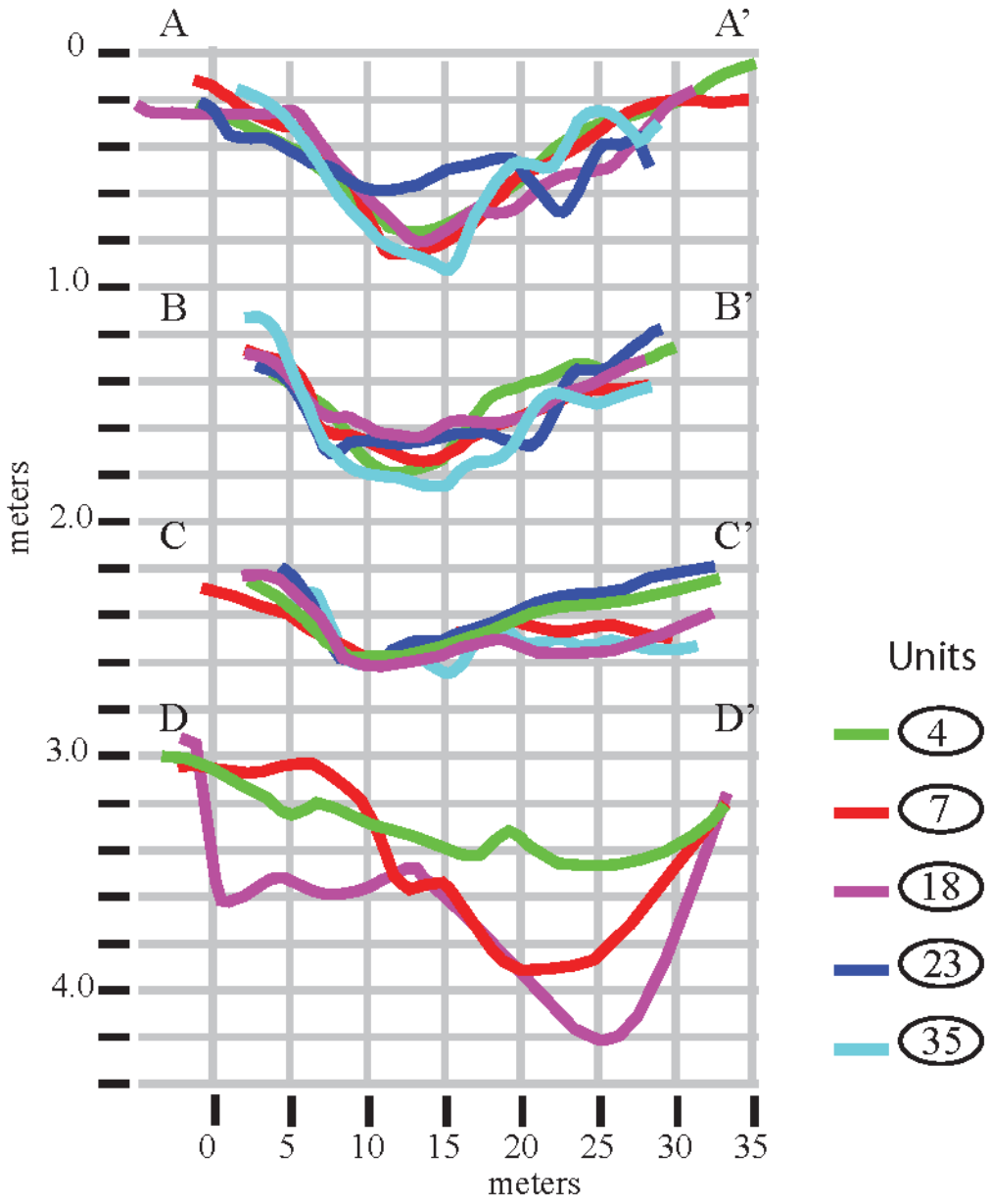

Figure 13. Stack of average elevation profile lines for earthquake surfaces taken from Figure 12. Profiles have been shifted so the southern margin of the sag aligns. These stacks highlight the similarity in syncline shape, and amount of vertical relief for each earthquake surface (FM1 through FM5).

and is on the edge of the data for units 4, 7 and 18 and so is difficult to compare. Overall, we find that the shape of the syncline is strikingly similar for all five earthquake surfaces.

It is difficult to capture the 3D differences between surfaces in the cross sections, so we also compare the volume and area folded in each of the earthquakes (Table 1). This is calculated by measuring volume of fold relief below the inflection from gradual to steep surface slope along the sag margins (Figure 9). We know from the profiles in Figure 11 that the margins of the sags are relatively steep, and most vertical relief is captured there, so the region below this inflection point should reflect most structural relief generated by each earthquake. The inflection point ranges from ~ -0.5 to -0.75 m of structural relief, shown by the color ramp for all surfaces in Figure 9 (approximately the yellow to orange transition, Figure 9). We measure fold volume below this inflection point on the basin margins for a swath of topography clipped between profiles A-A' and C-C' shown on Figure 9. This area overlaps in all surface models, so we can directly compare structural relief generated event by event for exactly the same location. Using the entire surface model would bias fold relief volumes towards the higher stratigraphic units that have more areal coverage. However, the method used here still biases toward stratigraphically higher surfaces; lower surfaces for FM 4 and FM5 (Figure 9h, j) are shorter in the northeast – southwest direction (perpendicular to the fold axis). However, this should have a small effect in this comparison because the inflection for these surfaces is in-board (basin-ward) of the surface edges.

We consider fold volume to be a proxy for vertical relief over an area. We find that earthquake FM1 has greater fold volume than all other surfaces. FM2 and FM3 have roughly the same amount fold volume. FM3 is roughly 85% of FM2, but the greatest

structural relief at the FM3 horizon occurs west of the area we analyzed (Figure 9f). FM4 has smaller fold volume than the other four earthquake surfaces and is an overestimate because this horizon includes some fraction of FM5 deformation. FM5 values are minimum estimates and should increase to values similar to FM2 and 3 (Table 1), with a correction for the relict FM5 relief included in FM4 estimates. Overall, structural contour maps and fold volume estimates highlight the similarities in sag (fold) geometry and orientation for all five events, and reveal similar structural relief in the Western Sag for four of the last 5 events.

Table 1. Volume and Folding estimates of vertical relief generated by earthquakes FM1 through FM5.

Earthquake	Volume (m^3)	Area (m^2)
FM1 (1857)	127	570
FM2	78	368
FM3	67	376
FM4	43	312
FM5	55	245

* Note the volume of unfolded unit 23 is not equivalent to FM4, so values here are high, and includes a fraction of FM5 deformation.

FM5 values are low, some fraction included in FM4. With a correction FM5 values will increase, and FM4 will decrease.

8. Discussion

At the FM site we have extensively documented dual depocenter sags separated by an intra-basin high, our observations support analog sand-box and clay cake transtensive step-over model results by Wu et al. (2009) and Mitra and Paul (2011). Wu et al. (2009) find that the dual opposing depocenter geometry forms in the early to middle

stages of transtensional basin evolution, and that basin margins are characterized by en-echelon oblique extensional faults that hard-link with increased displacement on the fault, this suggests that the active step constrained by trenches is young. The broader, depression bounding, step-over traces at the FM site point to more mature, late stage evolution (Figure 2). Older basin side wall faults on the norhease and southwest margins of the site have been abandoned in the last > 7 earthquakes (Scharer et al., 2014), and slip has been transferred basin-ward of those traces, to its present configuration (Figure 1, 2). With enough cumulative lateral slip on the SAF the active cross-basin faults identified in our trenches will eventually link up, completely bypassing the geometrical complexity that locally drives the right step (Wu et al., 2009; McClay and Dooley, 1995).

Retrodeformed stratigraphic surfaces allow direct comparison of fold shape, orientation, and amplitude for the last five earthquakes. We find that rupture across the step-over generated a long trough trending N55 – 60°W for earthquakes FM 1 through 5 (Figure 9). Retrodeformed and gradient corrected surfaces in Figure 9 have 25 cm contours to highlight narrow, steep areas with the greatest structural relief. Profiles taken across these surfaces reveal steep side-walls and a roughly flat bottom (Figure 13). This highlights that the majority of vertical relief generated in a rupture is concentrated on the margins of the sags and is accommodated by both oblique normal faulting and folding. These findings are also similar to experimental clay models for an oblique step-over (e.g. Figure 3; Mitra and Paul, 2011), and observations of ruptures across releasing step-overs in earthquakes (e.g. 2010 Yushu earthquake, China, Guo et al., 2012). From studies such as these we know the ratio of lateral slip outside the step-over and vertical relief within the step-over vary based on step-over geometry, size, and depth of the step.

We know 4 - 5 m of slip occurred across the active, 40 m wide, 150 m long step-over at the site in 1857, FM1 (Sieh, 1978; Madden et al., 2013); and so at least 2 earlier earthquakes must have had similar slips. One earlier earthquake, FM4, is smaller than all the others, probably generating~ 0.24 m of structural relief, sagging, across the step-over. The earliest earthquake considered here, FM5 generated 1/3 more structural relief across the step-over than 1857, and so must have had larger slips at the site. We conclude that earthquakes FM1, FM2 and FM3 are very similar and slip in FM5 is only ~ 33% greater, and within a 0.6 coefficient of variation, which is the variability of surface displacement at a point on a fault (Hecker et al., 2013). Earthquake FM4 has smaller displacement than the other five earthquakes, and is not within the coefficient of variation of 0.6 for the FM1 vertical displacement, and so must represent smaller slip at the site in that earthquake.

With the increased availability to collect airborne and terrestrial LiDAR after a rupture it will become possible to compare rupture and sag deformation across step-overs relative to the amount of slip on the fault, and the geometry of the step-over (transtensive or pure strike slip), and develop empirical relationships between all of these factors. Empirical relationships from historic ruptures combined with this study and other 3D structural analyses of sags formed at a step-over on strike slip faults will allow scientists to estimate lateral slips for observed fold deformation at sag-pond paleoseismic sites. This would increase the number of directly dated slip estimates along many faults, and would greatly improve our understanding slip distribution along paleo-ruptures, and could in turn inform our understanding of the behavior of fault rupture and fault rupture models.

9. Conclusions

We present the first 3D paleoseismic study constraining vertical relief generated in each of the last five earthquakes across a small step-over on the Southern SAF at Frazier Mountain. Earthquakes ruptured through the site and repeatedly down-dropped stratigraphy within the step-over depression. We document progressive fold deformation with depth, and growth strata sequences above earthquake horizons. We find that four of the last five earthquakes were remarkably similar, with ~ 0.8 m of vertical relief across the sag, the synclinal trough trends N55 – 60°W, and vertical relief is largely accommodated on the sag margins for all five earthquakes considered here (FM 1 through FM5). We use slip on the fault in the 1857 earthquake as a proxy for slip in three earlier events, and conclude that FM2, FM3 and FM5 all had ~ 4 to 5 m lateral displacements on the fault to generate vertical relief comparable to deformation observed at the 1857 event horizon. Earthquake FM4 has about 30% of the structural relief, and represents smaller lateral slip at the FM site in that event.

CHAPTER V

CONCLUSIONS

Introduction

This dissertation investigates the recurrence and style of coseismic deformation for surface rupturing earthquakes at two sites on the San Andreas Fault (SAF), California. In this dissertation, I have presented two very different studies and approaches to evaluate the similarity of rupture at a site and how it is affected by rupture extent for prehistoric earthquakes at the Hazel Dell and Frazier Mountain paleoseismic sites. Paleoseismic studies like these, which characterize the frequency of large earthquakes on the SAF, deformation in these events, and how these earthquakes are associated with adjacent sites and broader segments are critical in order to evaluate fault behavior models, and to guide how seismic hazards should be modeled for faults like the SAF. I provide a brief summary of my findings, and how these data compare with a composite data set of earthquakes for California, below.

Chapter II presents the first geologic evidence for two pre-1906 surface rupturing earthquakes in the 19th century on the Santa Cruz Mountains section of the SAF. Historical records note several large earthquakes that caused widespread damage in the region, however it was not previously known with any certainty on which Bay Area faults these earthquakes occurred. At Hazel Dell, we find the SAF ruptured in 1906, 1890 and 1838. Table 1 summarizes the last four earthquakes, the interval between earthquakes and the estimated slip in the Hazel Dell area for each event. In this study (Chapter II), I also use information recorded for historical earthquakes, and compare the

timing and deformation at Hazel Dell with neighboring sites to correlate between sites and estimate earthquake rupture lengths and magnitudes for these earthquakes. In Chapter III, I use multiple high precision age-dating techniques to demonstrate with great certainty that the three most recent surface rupturing earthquakes at Hazel Dell occurred during European settlement of the area, and show how over interpretation of C14 and pollen data led to erroneous assignment of correlative events at nearby sites to the prehistoric era. High resolution age-dating for these earthquakes is important because the three earthquakes were very closely spaced in time, probably had similar displacements of 1 - 2 m (discussed in Chapters II and III). This suggests a cluster of surface rupturing earthquakes on the SAF in 68 years that culminated in the 1906 earthquake.

This 68 year rupture history differs greatly from the long interval before and after these events (Table 1). We are presently 108 years into the open interval since the 1906 earthquake. Perhaps paradoxically Table 1 also highlights that there is a similar range of displacements in each event, for a wide range of rupture lengths (or equivalently earthquake magnitudes) and the time interval before or after the events. Deformation at the site, and in the vicinity based on our correlation to other sites was similar in the M 7.9 1906 earthquake, a 490 km long rupture, and in the 1890 earthquake, an ~ M 6.2 to 6.4 earthquake, with only ~ 70 km rupture. The 1890 earthquake is a mere fraction (1/7) of the 1906 surface rupture length, but generated the same range of displacements in the Santa Cruz Mountains, so slip at a point in an earthquake is not a direct function of length or seismic moment (a function of rupture area and displacement). The southern Santa Cruz Mountains segment may be a transition zone between the fully locked Peninsula section to the north and the creeping San Juan Bautista section to the South (Chapter II),

which defines the end of all ruptures extending from the north. The Santa Cruz Mountains section is located at the tail end of large multi-segment ruptures (like the 1906 earthquake), and near the center of the rupture (and peak displacements) when this segment ruptures independently of other segments (like the 1890 earthquake). Or, there are internal local properties of the fault that tends to yield similar displacement each time it ruptures, regardless of the extent of the rupture.

Chapter IV examines deformation across a step-over for the last five surface rupturing earthquakes at the Frazier Mountain site on the Southern SAF. This study is part of a larger effort that I am a coauthor on (Scharer et al., 2014; Scharer, Weldon and Streig, *in review*) in which we dated and characterized pre-historic earthquakes at Frazier Mountain. Here, I only discuss the structural relief across the step-over associated with the past five earthquakes, which is the portion of the broader project that I was responsible for, organized and led. I isolated vertical relief generated in each of the last five earthquakes by retrodeforming 3D surfaces, interpolated from trench and CPT observations, for stratigraphic units displaced in earthquakes that occurred between the units. In this chapter I compare the geometry and amount of vertical relief in each of these earthquakes. Vertical relief, or sagging across the step-over, is very similar in four of five earthquakes since 1550 (Table 2). At Frazier Mountain, vertical relief generated in earthquakes FM1, FM2 and FM3 are very similar, and structural relief generated in the earliest earthquake considered here, FM5, is only ~ 33% greater than those events. Earthquake FM4, is smaller than all the others, and generated ~ 0.24 m of structural relief, or sagging, across the step-over (Table 2). Earthquake FM4 is beyond typical along strike variability of displacement, however FM5 is not, and so maximum vertical

relief across the step-over in this event is within a range comparable to FM1. I infer that slip is very similar in four of the last five events to generate the same style and amount of deformation across the step-over. We know 4 - 5 m of slip occurred at the site in FM1, the 1857 earthquake (Sieh, 1978; Madden et al., 2013), and so earthquakes FM2, FM3 and FM5 must have had similar slips.

Without rupture lengths for these earthquakes we cannot assess whether similar displacements at Frazier Mountain are associated with similar rupture extents, and whether larger or smaller displacements reflect larger or smaller ruptures. So we need to turn to results from our earlier study, Scharer, Weldon and Streig (*in review*), that correlates earthquakes between Frazier and other Southern SAF paleoseismic sites (Table 2, Rupture length column). In this study we find FM2 and FM4 are short ruptures less than 100 km in length, and FM3 is longer, extending ~300 km between paleoseismic sites (Table 2; Scharer, Weldon and Streig, *in review*). FM5 probably had a similar rupture length to the 1857 event (Table 2), and so based on this correlation, earthquake FM5 was at least as large as the M 7.9 1857 earthquake.

Table 1. Earthquakes identified at the Hazel Dell site in the Santa Cruz Mountains on the SAF, summarizing event ages, interval between earthquakes, estimated slip, rupture length and earthquake magnitude. Summarized from Chapters II and III.

Earthquake	Event Age (AD)	Interval	Slip	Rupture length	Magnitude Estimate
		open (>108 years)			
E1	1906		1.7 - 2 m	490 km	M 7.9
		16 years			
E2	1890		1 - 1.7 m	probably 70 km (Santa Cruz segment)	M 6.4
		52 years			
E3	1838		~ 1.5 m	at least 70 km (Santa Cruz segment)	M 6.8 to 7.2
				probably 140 km (Santa Cruz + Peninsula segment)	
		522-1083 years			
E4	755 - 1316		not resolved		

Table 2. Earthquakes identified at the Frazier Mountain site on the Southern SAF, summarizing event ages, interval between earthquakes, vertical relief estimates across the step-over, lateral slip ranges, rupture length and earthquake magnitude. Summarized from Chapter IV, Scharer et al., 2014, and Scharer, Weldon and Streig, *in review*.

Earthquake	Event Age (AD)*	Interval	Maximum Vertical relief	Lateral Slip	Rupture length*	Magnitude Estimate*
		open (>157 years)				
FM1	1857		0.70 m	4 - 5 m	350 km	M 7.9
		45 -124 years				
FM2	1733 – 1812		0.83 m	= to FM1	~100 km	~M 7 - 7.2
		107-276 years				
FM3	1563 to 1626		0.85 m	= to FM1	~300 km	~M 7.6
		43-86 years				
FM4	1540 to 1606		0.24 to 0.47 m	< 1/2 of FM1	<100 km	M 6.4 - 7
		30-96 years				
FM5	1510 to 1572		0.80 to 1.04 m	1/3 > than FM 1	~350 km	> M7.7 - 7.9

* OxCal modeled 2σ age ranges, rupture length and magnitude estimates from Scharer et al., 2014, and Scharer et al., in review.

Relating Paleoseismic Results to Fault Behavior Models

Paleoseismic studies at Hazel Dell and Frazier Mountain show a range of rupture lengths produce similar deformation at a site. These results call into question commonly accepted fault behavior models describing the spatial and temporal distribution of earthquakes along a fault (Figure 1). Which of these rupture models best describe our observations of displacement and rupture length for earthquakes on the Northern and Southern SAF? Strict segmentation (Figure 1c) is clearly not the case at either Hazel Dell or Frazier Mountain sites where varied rupture lengths are well established (Table 1 & 2, Rupture length). Partial segmentation is reasonable (Figure 1b), i.e. where a site is located at the tail end of a large multi-segment rupture and in the center of single segment ruptures. This could explain our observations at Hazel Dell, but not Frazier. We cannot rule out an entirely random rupture model (Figure 1a) for the Hazel Dell data set, but combining our results with results from other paleoseismic sites on the SAF may allow us

to further evaluate this model. There could also be an internal property of the fault that causes rupture, and once the rupture reaches the full seismogenic depth there is a set amount of displacement, this behavior is not described by these models.

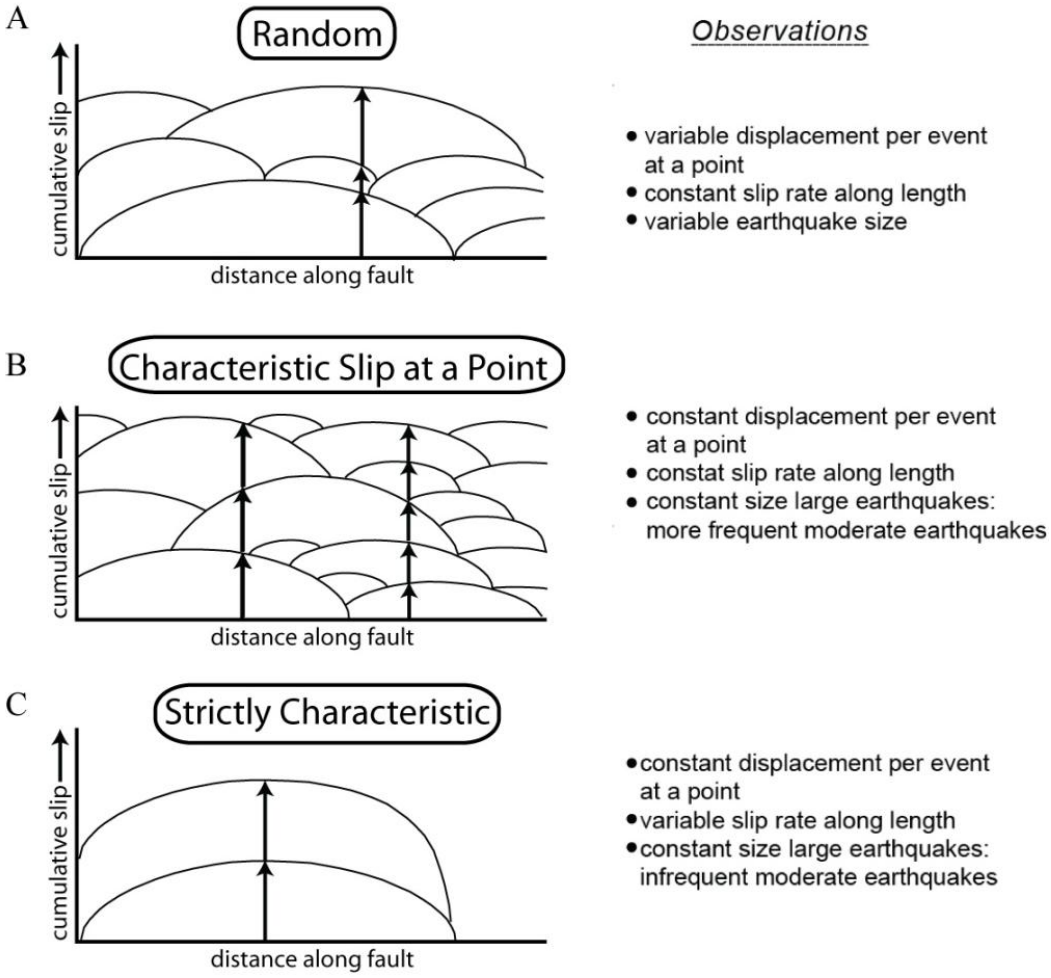

Figure 1. Models of slip accumulation along a fault, showing the spatial and temporal distribution of earthquakes and slip along the length of the fault. For, (A) Random model, (B) Characteristic slip at a point, (C) Strictly Characteristic earthquake model. Half circles represent slip along the length of a fault in one earthquake. Vertical arrows show coseismic slip at a point on the fault in different earthquakes. Modified from Sieh, 1981, and Schwartz and Coppersmith, 1984.

How can a range of earthquake rupture lengths produce similar displacements? Seismic moment is a function of rupture area and displacement, but rupture on a fault can

only grow as wide (i.e. deep) as the depth of the seismogenic zone (usually between 12 – 15 km depth), at this depth limit larger magnitude earthquakes grow in length (e.g. Scholz, 2008; King and Wesnousky, 2007). The aspect ratio of rupture length versus width for historic earthquakes (length/width) reveals that slip increases ~ linearly with rupture length for an aspect ratio of 10:1, but for earthquakes with aspect ratios >10:1 displacement values flatten out and become roughly constant, and displacement becomes independent of rupture length (Scholz, 2008). So, for a fault with a seismogenic depth of 15 km, a rupture 150 km long would have the same range of displacement as a rupture twice as long.

Figure 2 is a table from the 2013 Uniform California Earthquake Forecast (UCERF) and shows a composite plot of rupture length versus average displacement for earthquakes in California. On Figure 2, displacement rapidly rises in the first 200 km of rupture length, whereas 200 to 500 km long ruptures have about the same amount of slip. This plot highlights the relationships discussed above, and that we can observe ~ the same amount of displacement at a point despite different earthquake rupture lengths once rupture length is greater than 200 km. For example, at Frazier we observe ~ 4 - 5 m displacements for multiple events of varying rupture lengths ranging from 100 to 350 km (Table 2). Within the range of typical along strike variability of displacement, observations at Frazier agree with the relationship shown in Figure 2. This relationship does not explain smaller repeated displacements, like at Hazel Dell where we document 1 to 1.5 m of slip for estimated rupture lengths from 70 to 490 km. Here, the 490 km long 1906 earthquake generated ~1.7 m slips, and the 1890 earthquake, a ~ 70 km long rupture also generated 1 – 1.7 m of slip. As discussed above, Hazel Dell might best be explained

by a partial segmentation rupture model. The relationship in Figure 2 offers some insight that other processes might govern the tendency for similar slips at a point on a fault for a range of longer rupture lengths.

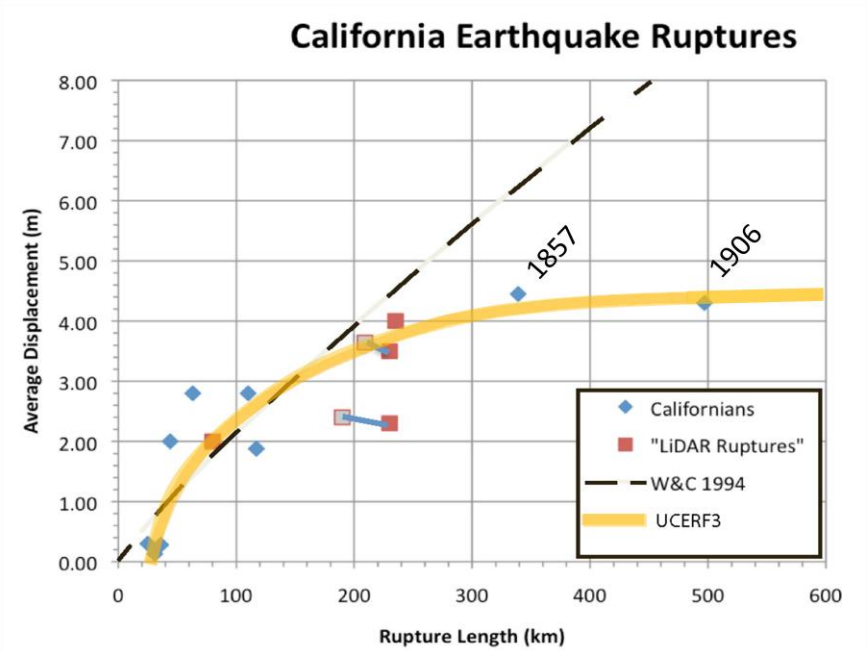

Figure 2. Plot of rupture length versus average displacement (m) for earthquakes in California. Blue diamonds are historic earthquakes in California with accepted displacement and length observations, red boxes are early historic and latest prehistoric ruptures recently measured from LiDAR data. Red boxes with gray interior are less likely, alternative interpretations for LiDAR measured ruptures. (Figure from Biasi et al., 2013, reproduced with permission from Weldon.)

APPENDIX A

HAZEL DELL SITE STRATIGRAPHIC UNIT DESCRIPTIONS, ADDITIONAL TRENCH LOGS, AND EVENT EVIDENCE TABLE

This appendix includes detailed stratigraphic unit descriptions, and modeled age ranges for the stratigraphic units. Additionally, we include a summary table of earthquake evidence for E1 – E4 including the type of event evidence, the location of the feature on the trench log and the interpreted Earthquake horizon for that trench exposure.

We excavated several fault normal trenches and could not present all trench logs in Chapter II. Plate A, includes photomosiac trench logs of the opposing trench walls for trenches 7, 8 and other exposures (cut back) of trench 10. Additionally, I include one log from Trench 4 located in the transpressional region (where the fault is locally left-stepping), where older stratigraphic units are nearer to the ground surface.

Detailed Stratigraphic Unit Descriptions

Unit 900 is a light gray massive clayey silt, this unit is only exposed in Trench 4. Detrital charcoal sampled from this unit yielded a 2σ modeled age range of B.C. 801 – 921.

Unit 700 is a massive greenish gray clay, observed only west of the structural depression (sag) bounding fault (Chapter II, Figure 5a). The base of the unit was not exposed, however as much as 50 to 65 cm of unit thickness is exposed in trenches T8 and

T10a. This is the oldest and deepest unit correlated between trenches. A single detrital charcoal sample from this unit yielded a 2σ modeled age range of B.C. 43 – 352.

Unit 600 is silty clay coarsening upward to silty sand, and is divided into subunits 600a and 600b. 600a is a light gray silty sand to silt, with some brown to strong brown mottles. This unit has a gradational basal contact to unit 600b. Unit 600b is light gray clayey silt to silty clay with common brown to strong brown mottles in the upper 15 cm. the basal contact is sharp over 5cm, and wavy. Unit 600a is discontinuous, and directly underlies the gravel unit 500. Unit 600a ranges between 10 to 15 cm thickness, where preserved, and unit 600b is 20 – 30 cm thick in trenches T8 and T10a. These units are observed west of the depression-bounding fault, and are correlated between trenches. Unit 600b has a 2σ OxCal modeled age of A.D. 663 – 872 (Chapter II, Figure 8).

Unit 500 is a matrix supported sandy gravel, composed primarily of sand and pebbles, with occasional cobbles and is the deepest and oldest stratigraphic unit observed both east and west of the fault, the matrix is tan to reddish brown (Chapter II, Figure 5a - Trench 8,). This unit has a weak soil developed in the upper 10cm, the soil overprints matrix, is medium gray, and is poorly preserved and discontinuous across trench 7 and 8 exposures. Unit 500 is 20 to 35 cm thick west of the fault, the base of the unit was not exposed east of the western sag-bounding fault. This unit unconformably overlies unit 600a and 600b.

Unit 400 is a massive gray to black clayey silt with abundant detrital charcoal fragments, this is subdivided into units 400a and 400b. The upper horizon, 400a (15-20 cm) is defined by a distinct dark gray to black color that grades downward to medium grey, it is massive with abundant detrital charcoal within the upper 10 cm, possibly in situ

burn horizon 400b is dark gray to gray blue clayey silt with lesser amounts of charcoal. The basal contact of the unit is slightly wavy and gradational over 5 to 10 cm. This unit represents fine-grained overbank alluvial deposits with strong organic development in unit 400a, the upper 20 to 30 cm of the deposit, is a buried soil and shows a period of marsh stability prior to deposition of the overlying sandy alluvial unit 300. Unit 400a is 5 cm thick west of the depression-bounding fault, and 8 – 20 cm thick east of the fault. Unit 400b is 20 to 30 cm thick where the base of the unit is exposed in T8. Unit 400a has a 2σ OxCal modeled age range between A.D. 1278 – 1400, and 400b an age range between A.D. 663 - 872.

Unit 300 is a light tan to grayish-orange silty sand to sandy silt and consists of three distinct alluvial deposits, subunits 300a, 300b and 300c. Subunit 300c is a massive to finely laminated light grayish yellow silty sand, within the structural depression in trench T10 the unit is interbedded very fine sand, silt and organic layers, with some angular axe-cut wood chips at the base of the unit. Unit 300c infills a depression formed on the unit 400a surface. The base of unit 300c is weakly laminated in areas with parted organic layers of redwood needles, leaves and cone fragments. 300c is 20 – 25 cm thick in trenches T7 and T8, and thickens substantially within the depression. At its thickest it is 70 cm in T10a, unit thickness decreased in subsequent cuts northward to 50cm in cut T10f. A redwood leaf sampled from the base of Unit 300c has an OxCal modeled age of A.D. 1651 – 1811, redwood needles collected from a needle hash layer within 300c axe-cut wood chips were also found at the base of Unit 300c and yielded an age range of A.D. 1642 - 1805, bristles from a redwood cone found in the unit have a modeled age of A.D. 1639 – 1804. Axe cut wood chips were found worked into the top of unit 400a and

within the base of unit 300c, and provide another age constraint (discussed in Chapter II). Dates from the growth rings in the wood chips allowed us to narrow the age of the deposit to post A.D. 1810. Subunit 300b is a massive to locally laminated and crossbedded tan to light orange silty sand. Unit 300b ranges from 15 to 30 cm thickness in all trench exposures. This is overlain by unit 300a, massive sandy silt to silty sand with some fine laminations. Unit 300a has a sharp to diffuse and planar basal contact, is 10 to 25 cm thick, and is not preserved everywhere. Units 300a, b and c represent relatively low energy water-lain and marsh deposits. Subunit 300f is slope derived colluvial deposits that interfinger with all water-lain facies of unit 300 (a-c), and is documented in the east end of trench T6.

Unit 200 is a light gray to grayish brown massive clayey silt with sand to coarse sand and consists of subunits 200a, 200b, 200c, 200d and 200f. Unit 200a is a light grayish brown silt, well sorted and massive, and is 10 – 25 cm thick. Subunit 200b is massive, contained abundant roots and rootlets and has a relatively planar basal contact that is gradational over roughly 5cm, and is 15 – 30 cm thick. Subunit 200a conformably overlies subunit 200b and grades upward from sandy silt to clayey silt with sand, the basal contact is gradual over ~5 cm. Unit 200c is massive, poorly sorted silt to coarse sand, this unit grades into 200d which has pockets of grain supported coarse sand along the base. Unit 200c is 35 cm thick in trench T10, and tapers to the north and south to 25 cm thickness in T7 and T8. Unit 200d is only observed in trench T10 cuts A through F, and is 15 – 30 cm thick. Unit 200f is a medium to dark gray brown massive silty sand with a weak incipient soil developed. 200f is only observed in trench T10 A through F, and is 5 – 10 cm thick. Unit 200 reveals a depositional change from the well-sorted

laminated sands and interbedded silts, clays and organic layers of Units 300a, 300b and 300c, to higher energy, coarse grained, massive mud flow deposits of Unit 200. Unit 200f reveals that there was a brief hiatus in deposition of the unit 200 sequence, 200f was deposited and persisted at the surface long enough to develop a weak soil, then was subsequently buried by 200d through 200a.

Unit 150 is a tan to light orange very fine sand, well sorted and discontinuous. Only observed in trench 10 cuts.

Unit 100, light brown to tan massive silt. This deposit represents agriculturally modified stratigraphy immediately below the ground surface including the depth of the till-zone and roots from former apple trees. This unit ranges from 30 to 40 cm thickness, and has a sharp (over 1 -2 cm) wavy basal contact.

Summary Table of Earthquake Evidence

Included in this appendix is a summary table of evidence for earthquakes E1 – E4 at the Hazel Dell site, including the type of event evidence, the quality of the observation, the location of the feature on the trench log and the interpreted Earthquake horizon for that trench exposure (Table A1). Two plots at the base of the table summarize the quality ranked evidence for each event horizon.

Table A1. Summary of Earthquake Evidence at Hazel Dell

Earthquake	Location *	Earthquake Evidence	Earthquake Horizon	Earthquake Qualifier**
E1 (1906)	T8 S 2008 m 1-2	A sub vertical fault extends upward into unit 200a. Units 400 -700 are truncated on the east by the fault.	200a base	Very likely
E1 (1906)	T8 N 2008 m 1-2	A sub vertical fault extends upward into unit 400a. Units 500 -700 are truncated on the east by the fault.	unclear	Probable
E1 (1906)	T7 N 2008 m 5.5-7	Fault extends upward to the base of unit 200a. The base of unit 300a is vertically separated 50 cm across 3 strands of the fault. Vertical separation is exaggerated by lateral slip on the fault.	200a base	Very likely
E1 (1906)	T7 S 2008 m 5-6	Fault extends into the base of unit 200a. Unit 400a is vertically separated 20 cm across the fault, 400a is thinner east of the fault and is juxtaposed against a thicker section of 400a west of the fault. Here lateral slip exaggerates apparent vertical separation of the units.	200a base	Very likely
E1 (1906)	T10a N 2008 upper bench	A sub vertical fault extends upward into unit 200a.	200a base	Likely
E2	T8 S 2008 m 6	Upward fault terminations within unit 300a top/200c base. Unit 300b is displaced between two fault strands, laminations within 300b are clearly offset with down on the east sense of displacement. Unit 300a is truncated against the eastern fault strand.	200c base	Very likely
E2	T8 N 2008 m 5-6	Upward fault terminations within unit 300a top/200c base. Unit 300b is displaced between two fault strands, laminations within 300b are clearly offset with down on the east sense of displacement.	300a/unclear	Very likely
E2	T7 N 2008 m 7-8	Upward fault terminations within unit 300b. Laminations in 300b are clearly offset, with down on the west sense of displacement. Unit 400a shows the same down on the east dispalcement.	300b top/unclear	Likely
E2	T7 S 2008 m7-8	Upward fault terminations within unit 300b. Laminations in 300b are clearly offset, with down on the west sense of displacement. Unit 400a shows the same down on the east dispalcement.	300a/unclear	Likely
E2	T10d N 2011 m 2-4	Units 200c and 200d in vertical fault contact with unit 300a and b.	200c top	Very likely
E2	T10f N 2011 m 2-4	Units 200c and 200d in vertical fault contact with unit 300a and b	200c top/200b base	Very likely
E2	T10g N 2011 m 2-4	Units 200c and 200d in vertical fault contact with unit 300a and b	200c top	Very likely
E2	T10a N 2008 m 5-7	Units 200c and 200d in vertical fault contact with unit 300a and b	200c top	Very likely
E3	T8 S 2008 m 5-7	Unit 400 is folded, with unit 300b and 300c deposited as an on-lap sequence against the fold scarp	400a	Likely
E3	T8 N 2008 m 4.5-6	Unit 400 is folded, with unit 300b and 300c deposited as an on-lap sequence against the fold scarp	400a	Likely

Earthquake	Location *	Earthquake Evidence	Earthquake Horizon	Earthquake Qualifier**
E3	T10d N 2011 m 2-4	Unit 400 is folded and faulted forming a depression/fissure >1m wide and 1.5 m deep. E2 generated a depression that was subsequently filled by units 300 a,b,c and 200 c,d.	400a	Very likely
E3	T10f N 2011 m 2-4	Unit 400 is folded and faulted forming a depression/fissure >1m wide and 1.5 m deep.	400a	Very likely
E3	T10g N 2011 m 2-4	Unit 400 is folded and faulted forming a depression/fissure >1m wide and 1.5 m deep.	400a	Very likely
E3	T10a N 2008 m 5-7	Unit 400 is folded and faulted forming a depression/fissure >1m wide and 1.5 m deep.	400a	Very likely
E4	T8 S 2008 m 2-6	Upward fault terminations within unit 500, and as upward terminating fissures that are filled with gravel from the overlying unit 500. Gravel filled fissures were observed near meters 2, 3 and 4.5.	500	Very Likely
E4	T8 N 2008 m 2-5	Upward fault terminations within unit 500, and as upward terminating fissures that are filled with gravel from the overlying unit 500. Gravel filled fissures were observed near meters 2, 3 and 4.5.	500	Very Likely
E4	T4 S 2008 m 10.5	Upward fault termination in unit T4-500?(deposit correlated with unit 500 in all other trenches), fault truncates the lower section of T4-500 gravel and places it in vertical fault contact with unit T4-700, a green-gray silty clay.	T4-500	Probable

* Location abbreviations are listed by trench number (eg. T8), trench wall (N-S), the year the trench was excavated, and the meter marker on the log where the event evidence is observed (eg. m 1-2).

** Earthquake Qualifiers based on criteria outlined in Scharer et al. (2007)

Earthquake	Sum of Rank	Average Rank
E1	22	4.4
E2	38	4.8
E3	28	4.7
E4	13	4.4

Earthquake evidence is ranked on a scale of 1 to 5, with 5 the higest score (very likely), and 1 the lowest (unlikely).

Histogram of event indicators compiled from above

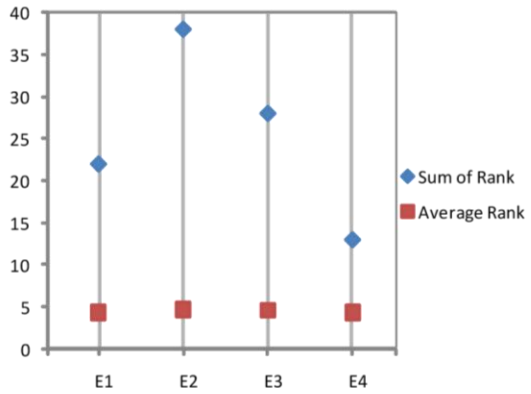

APPENDIX B

WIGGLE-MATCH OXCAL MODELS FOR TWO WOOD CHIP SAMPLES

We used AMS ^{14}C radiocarbon ages from growth rings sampled from wood chips recovered from unit 400a (Figure B1), the E3 earthquake horizon, to constrain the timing of the death of the chips independently of the Historic record. These wood chips have preserved bark, so we were able to sample both outer rings and the inner-most preserved ring. We count 180 annual growth rings for sample HD-2011-WC-1 and 24 rings for sample HD-2011-WC-2. A Bayesian approach combining 14C dates with the relative age between samples (years from annual growth rings) was employed to wiggle-match the results using OxCal v.4.1.7 (Bronk Ramsey, 2012; Bronk Ramsey et al., 2001). Using their wiggle-matching technique OxCal yields a 2σ modeled felling age range of 1698 and 1850 for sample HD_2011_WC1, and 1725 to 1973 for sample HD_2011_WC2. (Figure B2). We know from paleoseismic trenches that the felling date of these wood chips is prior to the 1906 earthquake. This trims the felling age range for sample HD_2011_WC2, to 1725 to 1906 (within 2σ confidence).

Figure B1. Photograph looking down (i.e. map view) of the top of unit 400a, a buried soil, showing in-place wood chips. Orange flags mark the locations of wood chips recovered from the unit as we excavate down. Notice the sharp cut edges of the wood fragments. Yellow level in the upper right corner for scale, 21 inches length.

(a)

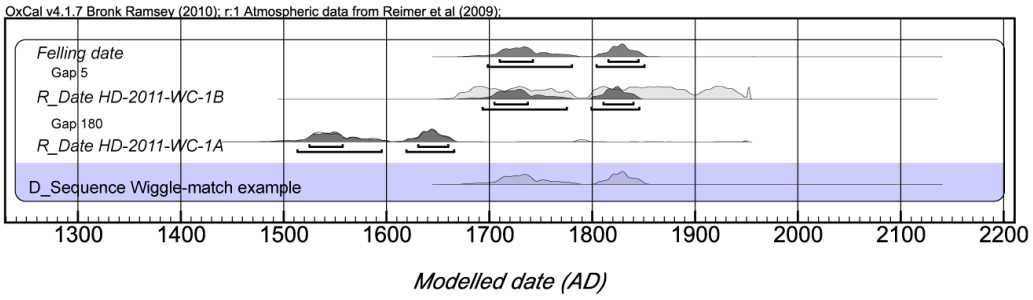

(b) OxCal Table View

Name	Unmodelled (BC/AD) from	to	%	from	to	%	Modelled (BC/AD) from	to	%	from	to	%	Indices A_{comb}	A
Felling date							1710	1845	68.2	1698	1850	95.4		
R_Date HD_2011_WC_1B	1682	1952	68.2	1669	1953	95.3	1705	1840	68.2	1693	1845	95.4	100.4	
R_Date HD_2011_WC_1A	1524	1659	68.2	1496	1795	95.4	1525	1660	68.2	1513	1665	95.4	104.7	
D_Sequence Wiggle-match	1710	1845	68.2	1698	1850	95.4							103.6	

(c)

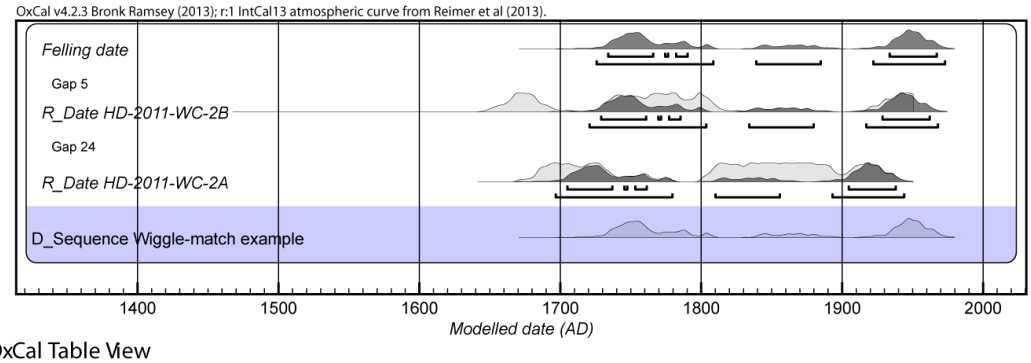

(d) OxCal Table View

Name	Unmodelled (BC/AD) from	to	%	from	to	%	Modelled (BC/AD) from	to	%	from	to	%	Indices A_{comb}	A
Felling date							1734	1967	68.3	1725	1973	95.3		
R_Date HD-2011-WC-2B	1664	....	68.3	1649	...	95.4	1729	1962	68.3	1720	1968	95.3	100.3	
R_Date HD-2011-WC-2A	1690	1925	68.2	1680	1938	95.5	1705	1938	68.3	1696	1944	95.3	89.7	
D_Sequence Wiggle-match	1734	1967	68.3	1725	1973	95.3							92.8	

Figure B2. OxCal model and table of calibrated ages for wood chip samples HD-2001-WC-1 and WC-2. (a) and (c) Prior probability distribution functions (pdf's) for radiocarbon samples shown in light gray, posterior pdf's shown in dark gray. (a) modeled felling date for sample HD-2011-WC-1A the inner growth ring, and HD-2011-WC-1B the outer growth ring, with 180 years of growth rings between inner and outer rings. 5 year lag between death of sample and the age of the outermost ring (methodology from Bronk Ramsey et al., 2001). (b) OxCal Table for sample HD-2011-WC-1. (c) modeled felling date for sample HD-2011-WC-2A the inner growth ring, and HD-2011-WC-2B the outer growth ring , with 24 years of growth rings between inner and outer rings. 5 year lag between death of sample and the age of the outermost ring (Bronk Ramsey et al., 2001). (d) OxCal Table for sample HD-2011-WC-2

APPENDIX C

RADIOCARBON SAMPLES FROM THE HAZEL DELL SITE

Table C1. Radiocarbon Samples from the Hazel Dell Site

Sample Name	Laboratory Number [*]	Unit	^{14}C age [†, ‡, §]	±	Material
HD T7-2	Beta-264162	200b	220	40	Charcoal
HD T7-7	Beta-254277	200b	350	40	Charcoal
HD T7-3	Beta-254274	300a	1150	40	Charcoal
HD10a-5-18	CAMS-158276	300c	220	30	Redwood needles
HD10a-7-22	CAMS-158277	300c	230	30	Redwood cone fragments
HD T8-2	Beta-264164	300c	340	40	Charcoal
HD10a-3-28	CAMS-158278	400a Top/300c base	190	30	Redwood branch and needles
HD10a-3-28-duplicate	CAMS-158289	400a Top/300c base	160	30	Redwood branch and needles
HD-2011-WC-1-A	CAMS-158281	400a Top	280	30	Wood chip, inner growth ring
HD-2011-WC-1-B	CAMS-158282	400a Top	130	40	Wood chip, outer growth ring
HD-2011-WC-2-A	CAMS-158283	400a Top	115	30	Wood chip, inner growth ring
HD-2011-WC-2-B	CAMS-158284	400a Top	185	35	Wood chip, outer growth ring
HDT8-40-1	CAMS-158280	400a	350	30	Charcoal
HD T7-5	Beta-264163	400a	340	40	Charcoal
HD T7-1	Beta-264161	400a	590	40	Charcoal
HD T7-4	Beta-254275	400a	650	40	Charcoal
HD T7-6	Beta-254276	400a	640	40	Charcoal
HD T8-31	Beta-254278	600b	1250	40	Charcoal
HDT8-32-2008	CAMS-158279	600b	1270	30	Charcoal
HD 4-1	Beta-264157	700a Top	2260	40	Charcoal
HD 4-7	Beta-264158	700b Base	2120	40	Charcoal
HD 4-9	Beta-264159	700b Base	2300	40	Charcoal
HD 4-12	Beta-264160	900	2710	40	Charcoal

Notes:

[*]) Samples processed at Center for Accelerator Mass Spectrometry (CAMS) at Lawrence Livermore National Laboratoryand Beta Analytic Inc., Florida (Beta).

[†]) The quoted age is in radiocarbon years using the Libby half life of 5568 years and following the conventions of Stuiver and Polach (ibid.).

[‡]) Radiocarbon concentration is given as conventional radiocarbon age.

[§]) Sample preparation backgrounds have been subtracted, based on measurements of samples of ^{14}C-free wood. Backgrounds were scaled relative to sample size.

APPENDIX D

ARANO FLAT OXCAL MODEL AND

TABLES OF RADIOCARBON SAMPLES

In this appendix, I provide an OxCal model of stratigraphic ages constraining the timing of earthquake horizons at the Arano Flat site, 9.5 km south of the Hazel Dell site on the Santa Cruz Mountains section of the SAF. I ran this OxCal model using the accelerator mass spectrometry ^{14}C age determinations from detrital charcoal samples collected from trenches and presented in a table in Fumal *et al.*, 2003b. No model was included in their Open File Report (Fumal *et al.*, 2003). This is Model version 6, outliers were trimmed in 5 earlier model iterations. Table D1 is table of values showing the modeled and unmodeled OxCal calibrated ages used to construct Figure D1. The complete table of radiocarbon samples from Fumal et al. (2003b) is provided in Table D2.

Figure D1. (next page) OxCal age model for samples from key stratigraphic units for the Arano Flat site (data from Fumal et al., 2003). This is a model of stratigraphic ages constraining the timing of earthquake horizons at the Arano Flat site, 9.5 km south of the Hazel Dell site on the Santa Cruz Mountains section of the San Andreas fault. Prior Probability distribution functions (pdf's) for radiocarbon samples shown in light gray, posterior pdf's shown in dark gray. Unit numbers shown on the blue shaded bars. Modeled earthquake ages shown by darker (red)pdf's and labeled by event name.

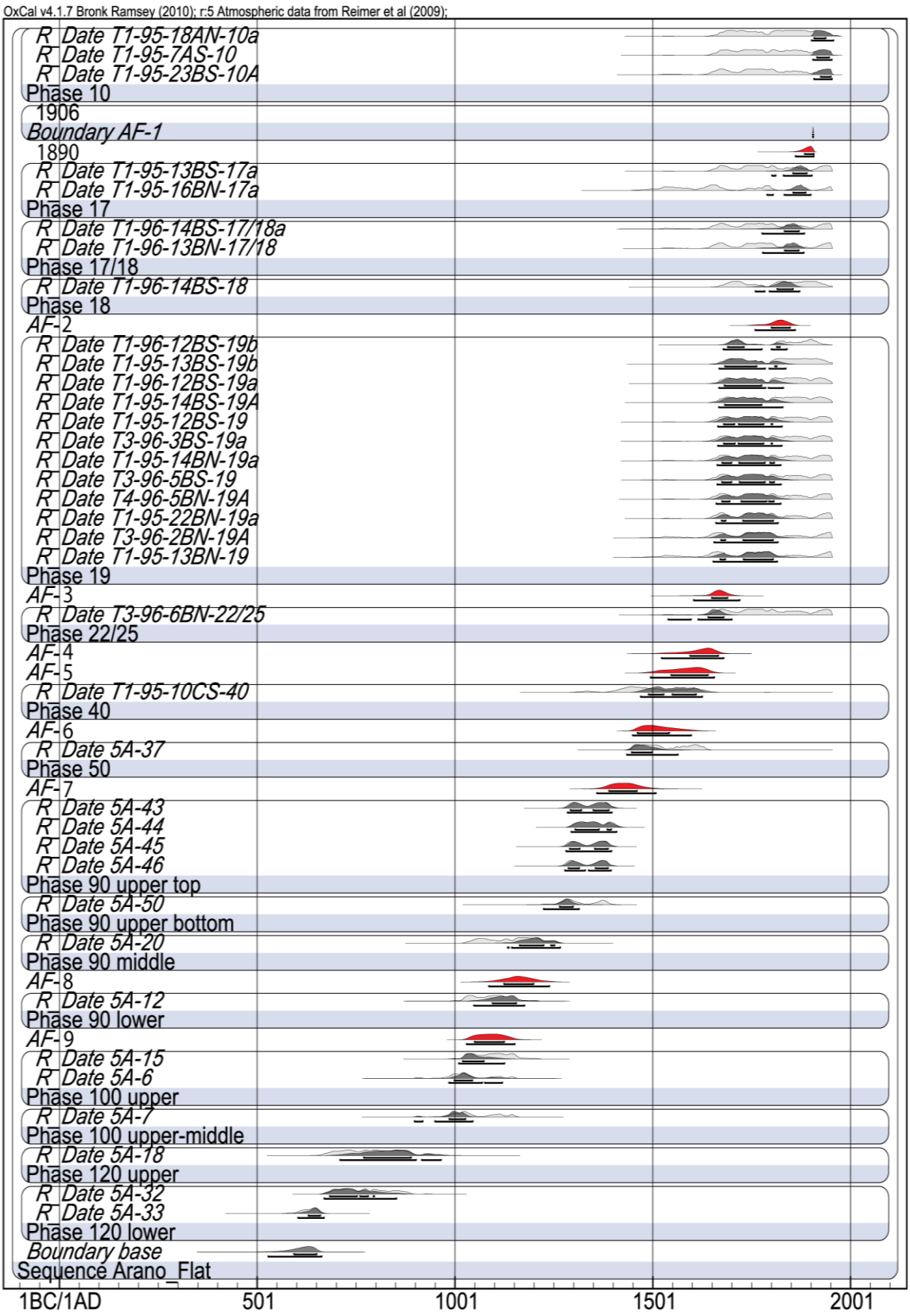
OxCal v4.1.7 Bronk Ramsey (2010); r:5 Atmospheric data from Reimer et al (2009);
R_Date T1-95-18AN-10a
R_Date T1-95-7AS-10
R_Date T1-95-23BS-10A
Phase 10
1906
Boundary AF-1
1890
R_Date T1-95-13BS-17a
R_Date T1-95-16BN-17a
Phase 17
R_Date T1-96-14BS-17/18a
R_Date T1-96-13BN-17/18
Phase 17/18
R_Date T1-96-14BS-18
Phase 18
AF-2
R_Date T1-96-12BS-19b
R_Date T1-95-13BS-19b
R_Date T1-96-12BS-19a
R_Date T1-95-14BS-19A
R_Date T1-95-12BS-19
R_Date T3-96-3BS-19a
R_Date T1-95-14BN-19a
R_Date T3-96-5BS-19
R_Date T4-96-5BN-19A
R_Date T1-95-22BN-19a
R_Date T3-96-2BN-19A
R_Date T1-95-13BN-19
Phase 19
AF-3
R_Date T3-96-6BN-22/25
Phase 22/25
AF-4
AF-5
R_Date T1-95-10CS-40
Phase 40
AF-6
R_Date 5A-37
Phase 50
AF-7
R_Date 5A-43
R_Date 5A-44
R_Date 5A-45
R_Date 5A-46
Phase 90 upper top
R_Date 5A-50
Phase 90 upper bottom
R_Date 5A-20
Phase 90 middle
AF-8
R_Date 5A-12
Phase 90 lower
AF-9
R_Date 5A-15
R_Date 5A-6
Phase 100 upper
R_Date 5A-7
Phase 100 upper-middle
R_Date 5A-18
Phase 120 upper
R_Date 5A-32
R_Date 5A-33
Phase 120 lower
Boundary base
Sequence Arano_Flat
1BC/1AD
501
1001
1501
2001
Modelled date (BC/AD)

Table D1. Arano Flat Table Results from OxCal Model

Calibrated unmodeled and modeled age ranges are shown as both 68.2% (1σ) and 95.4% (2σ).

Name	Unmodelled (BC/AD)						Modelled (BC/AD)							
	from	to	%	from	to	%	from	to	%	from	to	%	A	C
R_Date T1-95-18AN-10a	1683	1935	68.2	1668	1949	95.4	1909	1938	68.2	1902	1957	95.4	93.4	99.9
R_Date T1-95-7AS-10	1669	1947	68.2	1663	1952	95.4	1916	1947	68.2	1906	1953	95.4	102.6	99.9
R_Date T1-95-23BS-10A	1655	1952	68.1	1643	1954	95.4	1925	1951	68.2	1908	1954	95.4	109.4	99.9
Phase 10														
1906														
Boundary AF-1	1905	1906	68.2	1905	1906	95.4	1905	1906	68.2	1905	1906	95.4	100	100
AF-2							1885	1908	68.2	1862	1908	95.4		99.9
R_Date T1-95-13BS-17a	1664	1952	68.2	1652	1953	95.4	1855	1890	68.2	1802	1903	95.4	70.2	99.8
R_Date T1-95-16BN-17a	1521	1952	68.2	1468	1955	95.4	1856	1887	68.2	1790	1900	95.4	19.3	99.8
Phase 17														
R_Date T1-96-14BS-17/18a	1655	1952	68.1	1643	1954	95.4	1834	1870	68.2	1777	1884	95.4	81.1	99.6
R_Date T1-96-13BN-17/18	1652	1952	68.2	1642	1954	95.4	1834	1870	68.2	1779	1882	95.4	57.1	99.6
Phase 17/18														
R_Date T1-96-14BS-18	1692	1920	68.2	1675	1942	95.4	1815	1855	68.2	1760	1872	95.4	102.4	99.5
Phase 18														
AF-3							1801	1848	68.2	1760	1861	95.4		99.6
R_Date T1-96-12BS-19b	1697	1917	68.3	1681	1938	95.3	1690	1822	68.2	1679	1840	95.4	87.5	99.7
R_Date T1-95-13BS-19b	1690	1925	68.2	1669	1944	95.4	1683	1814	68.2	1669	1837	95.4	93.6	99.6
R_Date T1-96-12BS-19a	1682	1937	68.3	1669	1946	95.4	1682	1776	68.2	1668	1831	95.4	98.1	99.8
R_Date T1-95-14BS-19A	1681	1938	68.2	1666	1952	95.4	1683	1776	68.2	1668	1829	95.4	99.4	99.7
R_Date T1-95-12BS-19	1669	1947	68.2	1663	1952	95.4	1680	1803	68.2	1665	1827	95.4	104.5	99.8
R_Date T3-96-3BS-19a	1669	1947	68.2	1663	1952	95.4	1680	1803	68.2	1665	1827	95.4	104.5	99.7
R_Date T1-95-14BN-19a	1666	1951	68.1	1655	1953	95.4	1676	1808	68.2	1664	1824	95.4	107.0	99.8
R_Date T3-96-5BS-19	1666	1951	68.1	1655	1953	95.4	1676	1808	68.2	1664	1825	95.4	107.0	99.7
R_Date T4-96-5BN-19A	1663	1951	68.2	1648	1953	95.4	1676	1807	68.3	1661	1824	95.4	109.5	99.8
R_Date T1-95-22BN-19a	1661	1952	68.2	1647	1954	95.4	1675	1805	68.2	1661	1817	95.4	110.2	99.8
R_Date T3-96-2BN-19A	1645	1953	68.1	1524	1955	95.4	1673	1805	68.2	1656	1817	95.4	114.9	99.6
R_Date T1-95-13BN-19	1642	1953	68.2	1521	1955	95.5	1671	1805	68.2	1654	1815	95.4	115.7	99.8
Phase 19														
AF-4							1650	1690	68.2	1604	1720	95.4		99.9
R_Date T3-96-6BN-22/25	1663	1951	68.2	1648	1953	95.4	1641	1680	68.2	1540	1700	95.4	69.3	99.9
Phase 22/25														
AF-5							1595	1666	68.2	1523	1680	95.4		99.8
AF-6							1547	1640	68.2	1495	1656	95.4		99.8
R_Date T1-95-10CS-40	1414	1623	68.3	1324	1646	95.4	1490	1610	68.2	1470	1626	95.4	87.8	99.8
Phase 40														
AF-7							1462	1542	68.2	1450	1598	95.4		99.8

AF-7							1462	1542	68.2	1450	1598	95.4		99.8
R_Date 5A-37 Phase 50	1453	1623	68.2	1446	1635	95.4	1447	1498	68.2	1435	1564	95.4	105.5	99.8
AF-8							1390	1461	68.2	1360	1508	95.4		99.9
R_Date 5A-43	1290	1390	68.2	1281	1400	95.4	1293	1390	68.2	1285	1397	95.4	101.2	99.8
R_Date 5A-44	1306	1400	68.2	1294	1411	95.4	1305	1396	68.2	1295	1409	95.4	101.7	99.8
R_Date 5A-45	1286	1389	68.2	1278	1398	95.4	1291	1388	68.2	1282	1396	95.4	100.9	99.7
R_Date 5A-46 Phase 90 upper top	1283	1387	68.2	1274	1397	95.4	1287	1388	68.2	1279	1395	95.4	100.3	99.8
R_Date 5A-50 Phase 90 upper bottom	1268	1387	68.2	1226	1397	95.4	1265	1299	68.2	1225	1314	95.4	111.9	99.9
R_Date 5A-20 Phase 90 middle	1048	1217	68.2	1034	1252	95.4	1164	1252	68.2	1134	1267	95.4	98.6	99.8
AF-9							1125	1199	68.2	1086	1239	95.4		99.9
R_Date 5A-12 Phase 90 lower	1027	1153	68.2	1016	1182	95.4	1096	1156	68.2	1049	1176	95.4	102.7	99.8
AF-10							1050	1125	68.2	1030	1152	95.4		99.7
R_Date 5A-15	1027	1153	68.2	1016	1182	95.4	1020	1074	68.2	1011	1126	95.4	100.5	99.8
R_Date 5A-6 Phase 100 upper	983	1146	68.3	900	1155	95.4	999	1045	68.2	986	1120	95.4	115.1	99.8
R_Date 5A-7 Phase 100 upper-middle	989	1148	68.2	974	1155	95.4	986	1027	68.2	899	1046	95.4	106.6	99.6
R_Date 5A-18 Phase 120 upper	695	874	68.3	664	946	95.4	770	890	68.2	710	965	95.4	98.2	99.5
R_Date 5A-32	690	859	68.3	680	882	95.4	684	797	68.2	670	853	95.4	105.2	99.7
R_Date 5A-33 Phase 120 lower	615	655	68.2	590	666	95.4	630	660	68.2	604	670	95.4	104.7	99.6

Sequence Arano_Flat

Table D2. - Arano Flat Radiocarbon Ages

This is a complete table of radiocarbon samples run at LLNL CAMS presented in Fumal and others (2003). This table includes sample numbers, units and 14C ages and errors reported in their Open File Report. This is the full data table, no outliers have been trimmed from this data set.

Unit	**Sample #** [a]	**14C Age** [b, c, d]	**+/-**
Unit 120 lower	5A-19	1800	40
Unit 120 lower	5A-17	610	40
Unit 120 lower	5A-33	1410	30
Unit 120 lower	5A-32	1240	40
Unit 120 upper	5A-18	1230	60
Unit 120 upper	5A-16	2080	50
Unit 100 lower	5A-9	4040	40
Unit 100 lower	5A-13	1650	40
Unit 100 upper	5A-34	1060	50
Unit 100 upper	5A-31	1250	40
Unit 100 upper	5A-8	1070	40
Unit 100 upper	5A-7	1000	40
Unit 100 upper	5A-6	1010	40
Unit 100 upper	T1-95-10DS-100	1060	60
Unit 100 upper	5A-30	1030	40
Unit 100 upper	5A-15	950	40
Unit 100 upper	5A-3	1320	50
Unit 100 upper	5A-2	1070	40
Unit 90 lower	5A-12	950	40
Unit 90 middle	5A-11	1010	40
Unit 90 middle	5A-36	970	40
Unit 90 middle	5A-35	960	40
Unit 90 middle	T1-95-10CS-100	1000	60
Unit 90 middle	T1-95-7CS-100	950	50
Unit 90 middle	5A-21	1060	40
Unit 90 middle	5A-20	880	50
Unit 90 middle	5A-14	1340	80

Unit 90 upper bottom	5A-52	780	40
Unit 90 upper bottom	5A-51	800	40
Unit 90 upper bottom	5A-50	690	50
Unit 90 upper top	5A-47	1020	60
Unit 90 upper top	5A-46	660	40
Unit 90 upper top	5A-45	650	40
Unit 90 upper top	5A-44	600	40
Unit 90 upper top	5A-43	640	40
Unit 50	5A-42	580	40
Unit 50	5A-41	1380	40
Unit 50	5A-40	670	40
Unit 50	5A-39	480	50
Unit 50	5A-38	490	40
Unit 50	5A-37	370	40
Unit 50	T1-95-11CS-50	910	60
Unit 50	T1-95-11CS-50C	160	60
Unit 40	T1-95-11CN-40	690	60
Unit 40	T1-95-9CN-40	480	60
Unit 40	T1-95-10CS-40	430	80
Unit 25	T1-95-11CN-25	3120	60
Unit 25	T1-95-9BS-25	2300	80
Unit 25	T1-95-12CN-25	1110	60
Unit 25	T1-96-13DS-25	770	40
Unit 25	T3-96-5BN-25-CAMS33090	630	50
Unit 25	T1-95-11CS-25	610	60
Unit 25	T1-95-21DN-25a	560	50
Unit 25	T1-95-10BS-25	410	80
Unit 25	T3-96-5BN-25-CAMS31267	390	60
Unit 25	T1-95-11BN-25A	380	60
Unit 22/25	T3-96-3CS-22/25	490	60
Unit 22/25	T3-96-4BS-22/25b	470	60
Unit 22/25	T4-96-4BN-22/25B	360	60
Unit 22/25	T3-96-4BS-22/25-CAMS31266	320	60
Unit 22/25	T3-96-4BS-22/25-CAMS31476	270	60
Unit 22/25	T3-96-6BN-22/25	170	60

Unit 22	T1-95-12CS-22-CAMS27246	800	50
Unit 22	T3-96-3CN-22-CAMS31477	700	50
Unit 22	T3-96-3CN-22-CAMS31271	510	50
Unit 22	T1-95-16CN-22a	500	60
Unit 22	T1-95-12CS-22-CAMS22851	420	60
Unit 22	T1-96-14CS-22a	350	50
Unit 22	T1-95-12BN-22A	330	60
Unit 22	T1-96-14CS-22b	310	50
Unit 19	T1-95-21CN-19A	3450	70
Unit 19	T1-95-18BN-19A	2500	60
Unit 19	T1-95-17BS-19A	1870	60
Unit 19	T1-95-20CN-19A	460	60
Unit 19	T4-96-5BN-19B	350	60
Unit 19	T1-95-13BN-19	210	60
Unit 19	T3-96-2BN-19A	200	60
Unit 19	T1-95-22BN-19a	180	50
Unit 19	T4-96-5BN-19A	170	60
Unit 19	T3-96-5BS-19	160	60
Unit 19	T1-95-14BN-19a	160	60
Unit 19	T3-96-3BS-19a	150	60
Unit 19	T1-95-12BS-19	150	60
Unit 19	T1-95-14BS-19A	130	60
Unit 19	T1-96-12BS-19a	130	50
Unit 19	T1-95-13BS-19b	100	60
Unit 19	T1-96-12BS-19b	50	50
Unit 18	T1-95-15BN-18A	2520	70
Unit 18	T1-95-18BN-18a	1220	50
Unit 18	T1-95-14BS-18A	380	60
Unit 18	T1-95-17BN-18a	340	60
Unit 18	T1-96-13BS-18b	310	60
Unit 18	T1-96-4AS-18	310	60
Unit 18	T1-95-13BS-18	290	60
Unit 18	T1-96-15BN-18a	280	50
Unit 18	T3-96-4AS-18	280	50
Unit 18	T1-95-14BS-18b	230	50
Unit 18	T3-96-3BS-18	220	50
Unit 18	T1-95-19CS-18A	220	50
Unit 18	T3-96-15BN-18B	120	60

Unit 18	T1-96-14BS-18	80	60
Unit 17/18	T1-96-14BN-17/18	300	50
Unit 17/18	T1-96-14BS-17/18b	270	60
Unit 17/18	T1-96-13BN-17/18	190	50
Unit 17/18	T1-96-14BS-17/18a	180	60
Unit 17	T1-95-13BS-17b	430	60
Unit 17	T1-96-13BN-17A	370	40
Unit 17	T1-95-16BN-17a	250	60
Unit 17	T1-95-13BS-17a	170	50
Unit 10	T1-95-5AN-10	370	60
Unit 10	T1-95-23BS-10A	180	60
Unit 10	T1-95-7AS-10	150	60
Unit 10	T1-95-18AN-10a	120	60

Notes:

a) Samples processed at Center for Accelerator Mass Spectrometry (CAMS) at Lawrence Livermore National Laboratory, and at Beta Analytic Inc., Florida (Beta).

b) Preliminary ^{14}C ages, a d13C value of -22 was used as the assumed value for all samples according to Stuiver and Polach (Radiocarbon, v. 19, p.355, 1977).

c) The quoted age is in radiocarbon years using the Libby half life of 5568 years and following the conventions of Stuiver and Polach (1977).

d) Radiocarbon concentration is given as conventional radiocarbon age.

APPENDIX E

RADIOCARBON SAMPLES USED FOR WIGGLE MATCHING

AND A REVISED OXCAL MODEL

FOR THE HAZEL DELL SITE

Table E1. Radiocarbon Ages for wood chips, redwood cones & needles, and detrital charcoal from the Hazel Dell Site.

Sample Name	Laboratory Number [a]	Unit	^{14}C age [b, c, d, e]	± (1 σ)	Material [f, g]
HD T7-2	Beta-264162	200b	220	40	Charcoal
HD T7-7	Beta-254277	200b	350	40	Charcoal
HD T7-3	Beta-254274	300a	1150	40	Charcoal
HD10a-5-18	CAMS-158276	300c	220	30	Redwood needles
HD10a-7-22	CAMS-158277	300c	230	30	Redwood cone fragments
HD T8-2	Beta-264164	300c	340	40	Charcoal
HD10a-3-28	CAMS-158278	400a Top/ 300c base	190	30	Redwood branch and needles
HD10a-3-28-duplicate	CAMS-158289	400a Top/ 300c base	160	30	Redwood branch and needles
HD-2011-WC-1-A	CAMS-158281	400a Top	280	30	Wood chip, inner growth ring

HD-2011-WC-1-B	CAMS-158282	400a Top	130	40	Wood chip, outer growth ring
HD-2011-WC-2-A	CAMS-158283	400a Top	115	30	Wood chip, inner growth ring
HD-2011-WC-2-B	CAMS-158284	400a Top	185	35	Wood chip, outer growth ring
HDT8-40-1	CAMS-158280	400a	350	30	Charcoal
HD T7-5	Beta-264163	400a	340	40	Charcoal
HD T7-1	Beta-264161	400a	590	40	Charcoal
HD T7-4	Beta-254275	400a	650	40	Charcoal
HD T7-6	Beta-254276	400a	640	40	Charcoal
HD T8-31	Beta-254278	600b	1250	40	Charcoal
HDT8-32-2008	CAMS-158279	600b	1270	30	Charcoal
HD 4-1	Beta-264157	700a Top	2260	40	Charcoal
HD 4-7	Beta-264158	700b Base	2120	40	Charcoal
HD 4-9	Beta-264159	700b Base	2300	40	Charcoal
HD 4-12	Beta-264160	900	2710	40	Charcoal
HD2013_S1	161669	Ring 1, innermost ring. Pith.	350	20	Growth ring. Redwood, tree stump
HD2013_S1 duplicate	161670	Ring 1, innermost ring. Pith.	350	20	Growth ring. Redwood, tree stump
HD2013_S40	161671	Ring 40	330	20	Growth ring. Redwood, tree stump

HD2013_S50	161672	Ring 50	330	20	Growth ring. Redwood, tree stump
HD2013_S50 duplicate	161673	Ring 50	365	20	Growth ring. Redwood, tree stump
HD2013_S60	161674	Ring 60	350	20	Growth ring. Redwood, tree stump
HD2013_S60 duplicate	161675	Ring 60	370	20	Growth ring. Redwood, tree stump
HD2013_S70	161676	Ring 70	365	20	Growth ring. Redwood, tree stump
HD2013_S80	161677	Ring 80	360	20	Growth ring. Redwood, tree stump
HD2013_S80 duplicate	161678	Ring 80	335	20	Growth ring. Redwood, tree stump
HD2013_S90	161679	Ring 90	365	20	Growth ring. Redwood, tree stump
HD2013_S100	161680	Ring 100	375	20	Growth ring. Redwood, tree stump

HD2013_S130	161681	Ring 130	285	20	Growth ring. Redwood, tree stump
HD2013_S140	161682	Ring 140	210	20	Growth ring. Redwood, tree stump
HD2013_S150	161683	Ring 150	215	20	Growth ring. Redwood, tree stump
HD2013_S150 duplicate	161684	Ring 150	180	20	Growth ring. Redwood, tree stump
HD2013_S170	161685	Ring 170	190	20	Growth ring. Redwood, tree stump
HD2013_S170 duplicate	161686	Ring 170	145	20	Growth ring. Redwood, tree stump
HD2013_S240	161687	Ring 240	145	25	Growth ring. Redwood, tree stump
HD2013_S240 duplicate	161688	Ring 240	155	20	Growth ring. Redwood, tree stump
HD2013_S271	161689	Ring 271, near bark.	730	20	Growth ring. Redwood, tree stump

HD2013_S271 duplicate	161690	Ring 271, near bark.	260	20	Growth ring. Redwood, tree stump

Notes:

a) Samples processed at Center for Accelerator Mass Spectrometry (CAMS) at Lawrence Livermore National Laboratory, and at Beta Analytic Inc., Florida (Beta).

b) Preliminary ^{14}C ages, a d13C value of -22 was used as the assumed value for all samples according to Stuiver and Polach (Radiocarbon, v. 19, p.355, 1977).

c) The quoted age is in radiocarbon years using the Libby half life of 5568 years and following the conventions of Stuiver and Polach (1977).

d) Radiocarbon concentration is given as conventional radiocarbon age.

e) Sample preparation backgrounds have been subtracted, based on measurements of samples of ^{14}C-free wood. Backgrounds were scaled relative to sample size.

f) Tree ring samples from the redwood stump were pretreated with acid-alkali-acid washes, the final acid wash was a wet oxidation step (0.1 molar K2CrO5 + 2 molar H2SO4) to remove translocated folic acid/cellulose between growth rings and minimize measured age uncertainty.

g) Wood chip samples underwent standard acid-alkali-acid pretreatment and did not undergo wet oxidation.

APPENDIX F

UPDATED OXCAL MODEL WITH NEW AGE RESULTS FROM REDWOOD STUMP WIGGLE MATCH AND MACROFOSSILS

This appendix includes an updated OxCal model for stratigraphic ages constraining the timing of earthquake horizons at the Hazel Dell site using new tree stump age constraints (outer growth ring age range, 1789-1797 at 2σ confidence, Appendix G), and one macrofossil for unit 300 (sample HD10a-3-28, Appendix E; Figure F1, F2). Here, I include photographs of three macrofossils collected from unit 300 and run as AMS radiocarbon samples (Figure F1). Of these, only sample HD10a-3-28, a redwood leaf (branch & needles) was in stratigraphic order. Results from the updated model are included in Table F1.

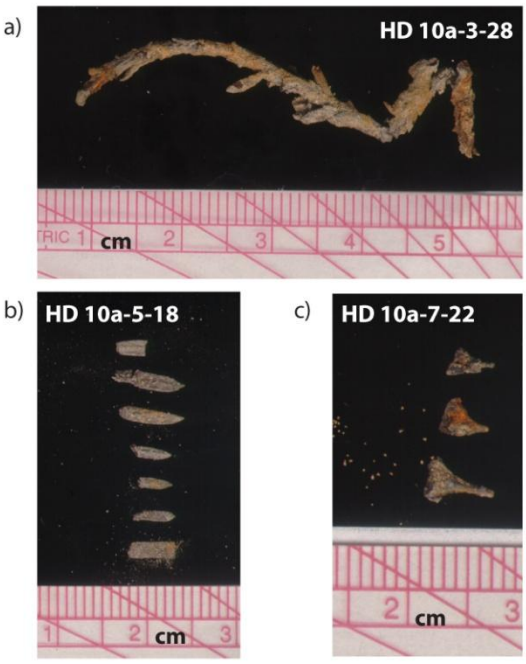

Figure F1. Macro fossils collected from block sediment samples of stratigraphic unit 300. Macro fossils were sampled by abrading sediment and picked using a binocular microscope. a) HD10a-3-28, redwood branch and needles; b) HD10a-5-18, redwood needles; c) HD10a-7-22 redwood cone fragments.

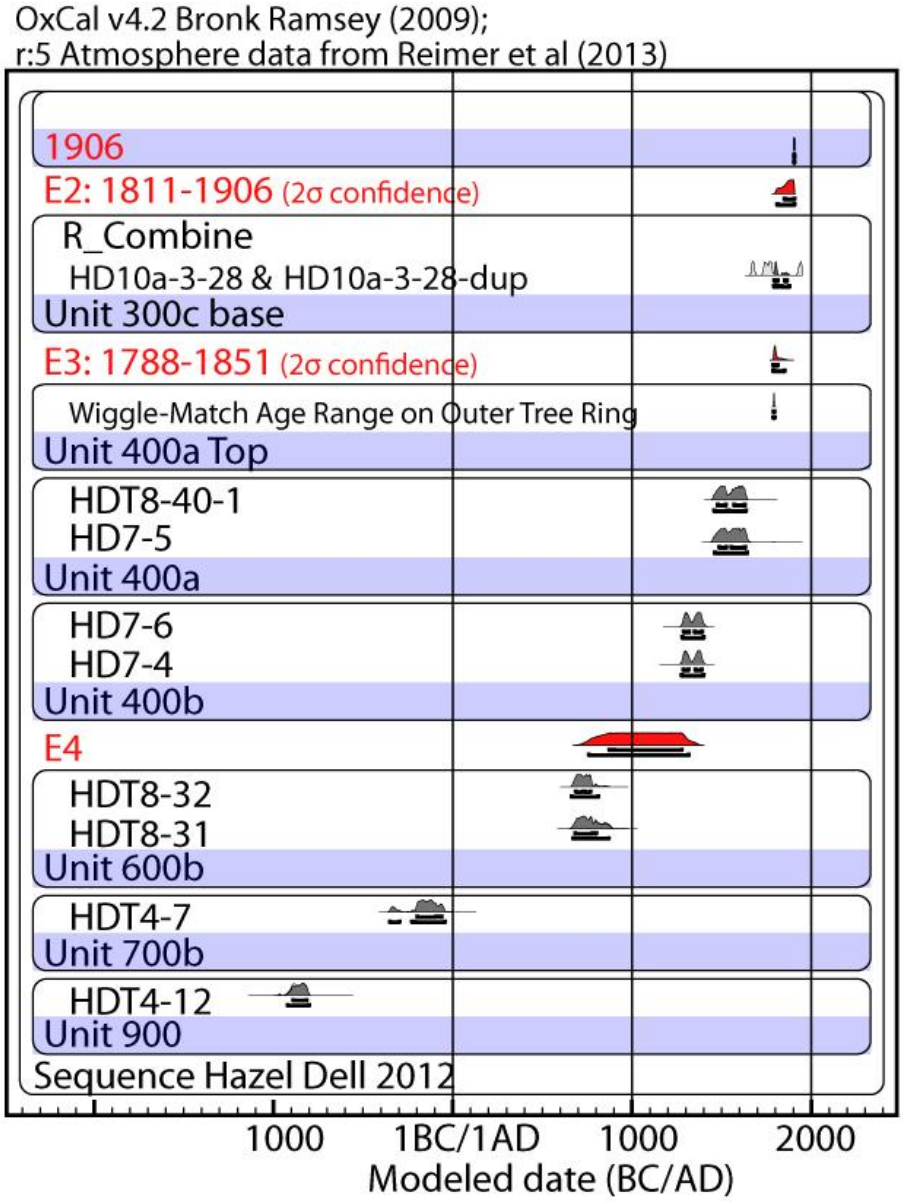

Figure F2. Updated OxCal model of stratigraphic units and earthquake age estimates for the Hazel Dell site. Prior Probability distribution functions (pdf's) for calibrated radiocarbon samples shown in light gray, posterior pdf's determined using ordering information shown in dark gray. Unit numbers are shown on the shaded bars. Modeled earthquake ages are labeled by event name. Note – inconsistent samples removed, see Appendix E for a complete list of samples.

Table F1. Table Results from the Updated Hazel Dell Site OxCal Model
Calibrated unmodeled and modeled age ranges are shown as both 68.2% (1σ) and 95.4% (2σ).

Name	Unmodelled (BC/AD)						Modelled (BC/AD)						Indicies
	from	to	%	from	to	%	from	to	%	from	to	%	C
1906													
Boundary E1	1905	1906	68.2	1905	1906	95.4	1905	1906	68.2	1905	1906	95.4	100
E2							1852	1906	68.2	1811	1906	95.4	99.9
R_Combine HD10a-3-28	1668	1948	68.2	1664	...	95.4	1795	1865	68.2	1793	1878	95.4	99.8
Phase 300c middle-top													
E3							1789	1814	68.2	1788	1851	95.4	99.9
C_Date Wiggle-Match Age Range on Outer Tree Ring	1790	1795	68.2	1789	1797	95.4	1790	1794	68.2	1788	1796	95.4	99.9
Phase 400a top													
R_Date HDT8-40-1	1481	1630	68.2	1458	1635	95.4	1478	1630	68.2	1460	1636	95.4	99.8
R_Date HD7-5	1485	1634	68.2	1462	1642	95.4	1488	1632	68.2	1462	1642	95.4	99.7
Phase 400 upper													
R_Date HD7-6	1290	1390	68.2	1281	1400	95.4	1290	1391	68.2	1282	1400	95.4	99.9
R_Date HD7-4	1286	1389	68.2	1277	1399	95.4	1287	1389	68.2	1278	1399	95.4	99.7
Phase 400 lower													
E4							875	1276	68.2	755	1316	95.4	99.8
R_Date HDT8-32	687	768	68.2	663	859	95.4	687	767	68.2	662	856	95.4	99.8
R_Date HDT8-31	681	855	68.2	672	879	95.4	680	800	68.2	671	875	95.4	99.8
Phase 600b													
R_Date HDT4-7	-200	-61	68.2	-352	-43	95.5	-200	-61	68.2	-353	-43	95.4	99.7
Phase 700b-lower													
R_Date HDT4-12	-896	-821	68.2	-930	-802	95.4	-887	-816	68.2	-923	-802	95.4	99.7
Phase 900?													
Boundary base							-1156	-834	68.2	-1687	-809	95.4	97.2
Sequence Hazel_Dell_2012													
Bronk Ramsey, C., 2013, OxCal Program, v.4.2: Radiocarbon Accelerator Unit, University of Oxford,https://c14.arch.ox.ac.uk/oxcal.html (last accessed 2 October, 2013).													

APPENDIX G

OXCAL DENDROCHRONOLOGIC WIGGLE MATCH

FOR GROWTH RINGS SAMPLED FROM

A BURIED REDWOOD TREE STUMP

AT THE HAZEL DELL SITE

Table G1. Table Results from OxCal Dendrochronologic Wiggle Match Model

Calibrated modeled age ranges are shown as both 68.2% (1σ) and 95.4% (2σ). Gaps represent the number of annual growth rings (years) between samples.

Tree Ring Sample & Interval	OxCal Modelled Ages (BC/AD)			
	68.20%		95.40%	
	from	to	from	to
Boundary E1 - 1906				
Outer Growth Ring - Ring 274	1791	1795	1789	1797
Gap 34 years				
R_Combine S240	1757	1761	1755	1763
Gap 70 years				
R_Date HD-2013-S170dup	1687	1691	1685	1693
Gap 20 years				
R_Combine S150	1667	1671	1665	1673
Gap 20 years				
R_Date HD-2013-S130	1647	1651	1645	1653
Gap 20 years				
R_Date HD-2013-S100	1617	1621	1615	1623
Gap 10 years				
R_Date HD-2013-S90	1607	1611	1605	1613
Gap 10 years				
R_Date HD-2013-S80	1597	1601	1595	1603
Gap 10 years				
R_Date HD-2013-S70	1587	1591	1585	1593
Gap 10 years				
R_Combine S60	1577	1581	1575	1583
Gap 10 years				
R_Combine S50	1567	1571	1565	1573
Gap 10 years				
R_Date HD-2013-S40	1557	1561	1555	1563
Gap 40 years				
R_Combine S1	1517	1521	1515	1523
D_Sequence Wiggle-match stump				

APPENDIX H

NON-NATIVE POLLEN ANALYSIS

FOR THE HAZEL DELL SITE

This appendix includes locations and results from pollen analysis at Hazel Dell (Figure H1). Table H1 presents pollen concentrations for three pollen samples shown in Figure H1. Pollen concentrations are generally less than 500 grains/cm3, so it is not possible to conduct pollen analysis. Standard samples have at least 10,000 grains per cm3. The soil sampled in the Hazel Dell trenches is generally "sterile" of pollen.

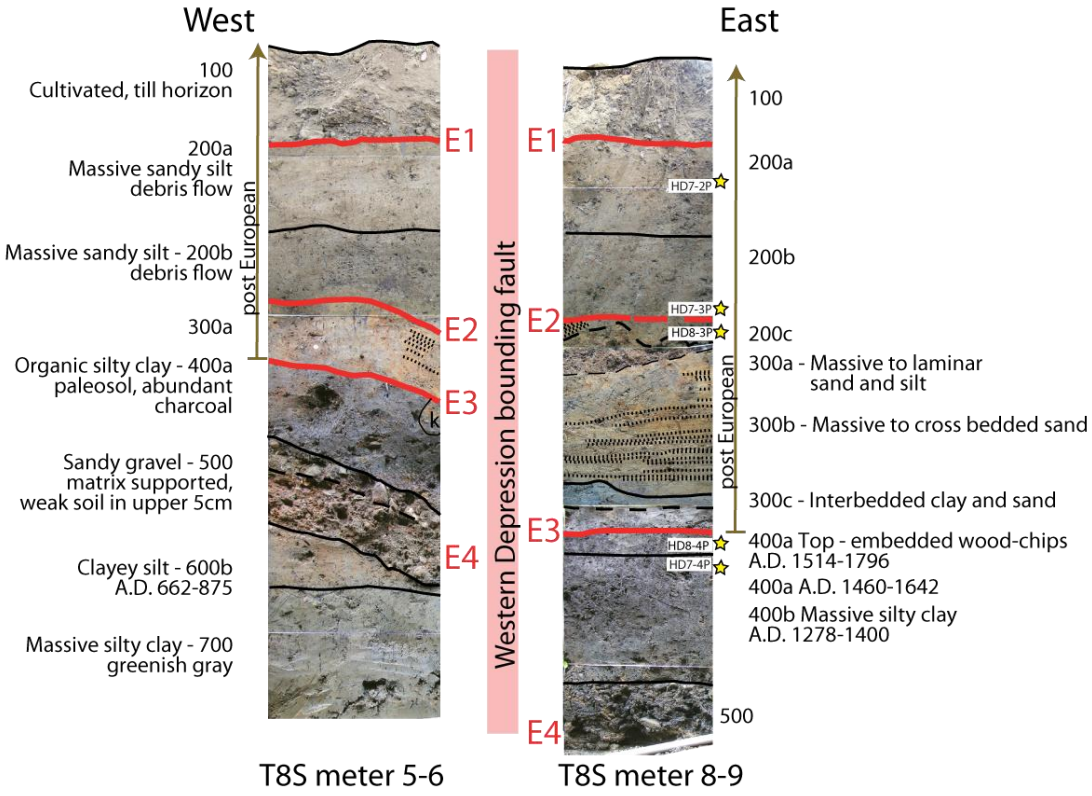

Figure H1. Photomosaic stratigraphic columns correlated between East and West sides of the primary Western depression bounding fault. Black lines are unit contacts, shaded lines labeled E1 through E3 are earthquake horizons. Yellow stars show units sampled for non-native pollen analysis, sample name (eg. HD8-3P) denotes study site (HD), Trench number (8), and pollen sample number in that trench (3). Trench locations and photomosaic logs are included in Chapter II, Appendix A and Plate 1A. Two sigma modeled age ranges for units shown in years A.D.

Table H1. Results from Hazel Dell Pollen Analysis

Hazel Dell Pollen samples			
	HD7-2P	**HDT8-3P**	**HD7-4P**
Date counted	4-Feb-14	4-Feb-14	17-Feb-14
Pollen			
Cyperaceae	1	2	
Pinus		1	1
Poaceae		1	1
Quercus		1	
Sequoia		1	
Pseudotsuga		2	
Cupressaceae		1	
Pollen sum	1	9	2
Spores			
Monolete	5	6	5
Trilete	2		3
Exotic lycopodium	155	80	80
Volume (cm3)	1.23	1.23	1.23
Spores/tablet	13911	13911	13911
Number of tablets	1	1	1
Pollen concentration (grains/cm3)	73	1272	283
Errors are +/- 5%			
Samples analyzed by Dan Gavin, UO			
Samples prepared by Liam Riedy,UCB			

REFERENCES CITED

CHAPTER II

Anderson, K. (2005). Tending the wild : Native American Knowledge and the Management of California's Natural Resources, University of California Press, 558 p.

Bakun, W.H. (1999). Seismic Activity of the San Francisco Bay Region, *Bull. Seism. Soc. Am*, **89**, 764-784.

Biasi, G.P., and R.J. Weldon II (2006). Estimating Surface Rupture Length and Magnitude of Paleoearthquakes from Point Measurements of Rupture Displacement, *Bull. Seism. Soc. Am.*, **96**, 1612-1623.

Biasi, G.P., and R.J. Weldon II (2009). San Andreas Fault Rupture Scenarios from Multiple Paleoseismic Records: Stringing Pearls, *Bull. Seism. Soc. Am.*, **99**, 471-498.

Brabb, E.E. (1989). Geologic map of Santa Cruz County California, scale 1:62,500; *USGS Open-File Report 97-489*, Geologic map of Santa Cruz County California: A digital database prepared by Graham, S., Wentworth, C., Knifong, D., Graymer, R., Blissenbach, J., 1997.

Bronk Ramsey, C., van der Plicht, J., and B. Weninger (2001). 'Wiggle matching' radiocarbon dates. *Radiocarbon*, **43**(2A), 381-389.

Bronk Ramsey, C. (2009). Bayesian analysis of radiocarbon dates. *Radiocarbon*, ***51***(1), 337-360.

Bryant, W.A., and M.M. Lundberg (2002). Fault number 1d, San Andreas fault zone, Santa Cruz Mountains section, in Quaternary fault and fold database of the United States: U.S. Geological Survey website, http://earthquakes.usgs.gov/hazards/qfaults, accessed 07/30/2013 03:47 PM.

Calcote, R. (1995). Pollen source area and pollen productivity: evidence from forest hollows, *Journal of Ecology*, **83**, 591-602.

Ellison, W.H., and F. Price (1953). The Life and Adventures in California of Don Agustin Janssens, 1834-1856, The Hunington Library, 40 – 41.

Freed, A.M. (2005). Earthquake Triggering by Static, Dynamic and Postseismic Stress Transfer, *Annu. Rev. Earth Planet. Sci.*, **33**, p. 335-367, doi:10.1146/annurev.earth.33.092203.12205.

Fumal, T.E. (2012). Timing of Large Earthquakes during the Past 500 Years along the Santa Cruz Mountains Segment of the San Andreas Fault at Mill Canyon, near Watsonville, California, *Bull. Seism. Soc. Am.*, **102**, doi:10.1785/0120110161.

Fumal, T.E., Heingartner, G.F., Dawson, T.E., Flowers, R., Hamiltong, J.C., Kessler, J., Reidy, L.M., Samrad, L., Seitz, G.G., J. Southon (2003a). A 100-Year Average Recurrence Interval for the San Andreas Fault, Southern San Francisco Bay Area, California, (Abstract S12B-0388) *EOS Trans. AGU* **84**, no. 46, Fall Meeting Supplement, F1003.

Fumal, T.E. Heingartner, G.F. Samrad, L., Dawson, T.E., Hamilton, J.C., and J.N. Baldwin, (2003b). Photomosaics and Logs of Trenches on the San Andreas Fault at Arano Flat near Watsonville, California: *U.S. Geological Survey Open-File Report 03-450*, Version 1.0.

Goldfinger, C., Ikeda, Y., Yeats, R., and J. Ren (2013). Superquakes and Supercycles, *Seis. Res. Lett.*, **84**, 24-32, doi: 10.1785/0220110135.

Hall, N.T., Wright, R.H., and K.B. Clahan (1999). Paleoseismic studies of the San Francisco peninsula segment of the San Andreas fault zone near Woodside, California, *J. Geophys. Res.*, **104**, B10, 23,215-23,236.

Hanks, T.C., and W.H. Bakun, 2002, A Bilinear Source-Scaling Model for M-log A Observations of Continental Earthquakes, *Bull. Seism. Soc. Am.*, **92**, 5, 1841-1846.

Hemphill-Haley, M.A., and R.J. Weldon, II (1999). Estimating Prehistoric Earthquake Magnitude from Point Measurements of Surface Rupture, *Bull. Seism. Soc. Am.*, **89**, 1264-1279.

Holden, Edward, S. (1892). Earthquakes in California in 1890 and 1891, *USGS Bulletin No. 95, Washington Government Printing Office*, 31pp.

Jacoby, G. C. (2000). Dendrochronology, in *Quaternary Geochronology: Methods and Applications*, J. S. Noller, J. M. Sowers, and W. R. Lettis (Editors), AGU Ref. Shelf, vol. 4, AGU, Washington, D. C., 11–20, doi:10.1029/RF004.

Johanson, I.A., and R. Bürgmann (2005). Creep and quakes on the northern transition zone of the San Andreas fault from GPS and InSAR data, *Geophys. Res. Lett.*, **32**, L143056, doi: 10.1029/2005GL023150.

Kozacı, Ö. (2012). Dendroseismology on the central North Anatolian fault, Turkey: Documenting three centuries of surface rupture history using tree rings, *J. Geophys. Res.*, **117**, B01405, doi:10.1029/2011JB008795.

Lawson, A.C. (1908). The California earthquake of April 18, 1906, Report of the State Investigation Commission. *Carnegie Institute of Washington, Washington, D.C.*, 451pp.

Lightfoot, K.G., Parrish, O., Panich, L.M., Schneider, T.D., and K.E. Soluri (2009). California Indians and Their Environment: An Introduction, University of California Press, eBook, 493p.

Louderback, G. D. (1947). Central California earthquakes of the 1830's, *Bull. Seism. Soc. Am.*, **37**, 33-74.

Mensing S. and R. Byrne (1998). Pre-mission invasion of Erodium cicutarium in California, *J. of Biogeography*, **25**, 757-762.

Perkins, J.A., Sims, J.D., and S.S. Sturgess (1989). Late Holocene Movement Along the San Andreas Fault at Melendy Ranch: Implications for the Distribution of Fault Slip in Central California, *J. Geophys. Res.*, **94**, 10,217-10,230.

Prentice, C.S., Crosby, C. J., Whitehill, C. S., Arrowsmith, J R., Furlong, K. P., and D. A. Phillips (2009). GeoEarthScope LiDAR illuminates northern California's active faults, *EOS Transactions of the American Geophysical Union*, **90**, no. 7, p. 55.

Prentice, C.S., D. J. Merritts, E. C. Beutner, P. Bodin, A. Schill, and J. R. Muller (1999). Northern San Andreas fault near Shelter Cove, California, *Geol. Soc. Am. Bull. 111*, **4**, 512–523.

Prentice, C.S., and D.J. Ponti (1997). Coseismic deformation of the Wrights tunnel during the 1906 San Francisco earthquake: a key to understanding 1906 fault slip and 1989 surface ruptures in the southern Santa Cruz mountains, California, *J. Geophys. Res.*, **102**, 635-648.

Prentice, C.S., and D.P. Schwartz (1991). Re-Evaluation of 1906 Surface Faulting, Geomorphic Expression, and Seismic Hazard along the San Andreas Fault in the Southern Santa Cruz Mountains, *Bull. Seism. Soc. Am.* **81**, 1424-1479.

Pybrum-Malmin, J (1998). Corralitos, 2nd edition, 302pp.

Reimer, P. J., Baillie, M. G. L., Bard, E., Bayliss, A., Beck, J. W., Bertrand, C. J. H., Blackwell, P. G., Buck, C. E., Burr, G. S., Cutler, K. B., Damon, P. E., Edwards, R. L., Fairbanks, R. G., Friedrich, M., Guilderson, T. P., Hogg, A. G., Hughen, K. A., Kromer, B., McCormac, G., Manning, S., Bronk Ramsey, C., Reimer, R. W., Remmele, S., Southon, J. R., Stuiver, M., Talamo, S., Taylor, F. W., van der Plicht, J., & Weyhenmeyer, C. E. (2004). IntCal04 terrestrial radiocarbon age calibration, 0-26 cal kyr BP. *Radiocarbon, **46***(3), 1029-1058.

Reimer, P. J., Baillie, M. G. L., Bard, E., Bayliss, A., Beck, J. W., Blackwell, P. G., Bronk Ramsey, C., Buck, C. E., Burr, G. S., Edwards, R. L., Friedrich, M., Grootes, P. M., Guilderson, T. P., Hajdas, I., Heaton, T. J., Hogg, A. G., Hughen, K. A., Kaiser, K. F., Kromer, B., McCormac, F. G., Manning, S. W., Reimer, R. W., Richards, D. A., Southon, J. R., Talamo, S., Turney, C. S. M., van der Plicht, J., & C. E. Weyhenmeyer, (2009). IntCal09 and Marine09 radiocarbon age calibration curves, 0-50,000 years cal BP. *Radiocarbon, **51***(4), 1111-1150.

Sarna-Wojcicki, A.M., Pampeyan, E.H., and T.N. Hall (1975). Map showing recently active breaks along the San Andreas fault between the Central Santa Cruz Mountains and the Northern Gablian Range, California: *U.S. Geological Survey Miscellaneous Field Studies Map*, 1:24,000, Map MF-650.

Scharer, K.M., Biasi, G.P., Weldon, R.J., and T.E. Fumal, (2010). Quasi-periodic recurrence of large earthquakes on the southern San Andreas fault, *Geology*, **38**, 555-558, doi: 10.1130/G30746.1.

Scharer, K.M., Weldon, R.J., Fumal, T.E., and G.P. Biasi (2007). Paleoearthquakes on the Southern San Andreas Fault, Wrightwood, California, 3000 to 1500 B.C.: A New Method for Evaluating Paleoseismic Evidence and Earthquake Horizons: *Bull. Seism. Soc. Am.*, **97**, 1054-1093, doi:10.1785/0120060137.

Sieh K., D. H. Natawidjaja, A. J. Meltzner, C. C. Shen, H. Cheng, K. Li, B. W. Suwargadi, J. Galetzka, B. Philibosian and R. L. Edwards (2008). Earthquake Supercycles Inferred from Sea-Level Changes Recorded in the Corals of West Sumatra: *Science*, **322**, p. 1674-1678, doi:10.1126/science.1163589.

Schwartz, D.P., Pantosti, D., Okumura, K., Powers, T., and J. Hamilton (1998). Paleoseismic investigations in the Santa Cruz Mountains: Implications for the recurrence of large magnitude earthquakes on the San Andreas Fault, *J. of Geophys. Res.*, **103**, 17,985-18,001.

Stein, R. (1999). The role of stress transfer in earthquake occurrence, *Nature*, **402**, 605-608.

Thatcher, W., G. Marshall, and M. Lisowski (1997). Resolution of fault slip along the 470-km-long rupture of the great 1906 San Francisco earthquake and its implications, *J. Geophy. Res.*, **102**, B3, 5353–5367.

Toppozada, T.R., and G. Borchardt (1998). Re-evaluation of the 1836 "Hayward fault" and the 1838 San Andreas earthquakes, *Bull. Seism. Soc. Am.*, **88**, 140-159.

Toppozada, T.R., Branum, D.M., Reichle, M.S., and C.L. Hallstrom (2002). San Andreas Fault Zone, California: M ≥ 5.5 Earthquake History, *Bull. Seism. Soc. Am*, **92**, 2555-2601.

Toppozada T.R., Real, C.R., and D.L. Parke (1981). Preparation of isoseismal maps and summaries of reported effects for pre-1900 California earthquakes, *Calif. Div. Mines Geol. Open-File Report 81-11 SAC*, 182 p.

Tuttle, M.P., and L.R. Sykes (1992). Re-evaluation of several large historic earthquakes in the vicinity of the Loma Prieta and Peninsular Segments of the San Andreas fault, California, *Bull. Seism. Soc. Am.*, **82**, 1802-1820.

Wald, D.J., Helmberger, D.V., and T.H. Heaton (1991). Rupture Model of the 1989 Loma Prieta Earthquake from the Inversion of Strong-Motion and Broadband Teleseismic Data, *Bull. Seism. Soc. Am.*, **81**, 5, 1540-1572.

Weldon, R.J., Scharer, K., Fumal, T., and G. Biasi (2004). Wrightwood and the earthquake cycle: What a long recurrence record tells us about how faults work, *GSA Today*, **14**, 4-10, doi: 10.1130/1052-5173(2004)014<4:WATECW>2.0.CO;2

Wells, D.L., and K.J. Coppersmith (1994). New Empirical Relationships among Magnitude, Rupture Length, Rupture Width, Rupture Area and Surface Displacement, *Bull. Seism. Soc. Am.*, **84**, 4, 974-1002.

WGCEP (Working Group on California Earthquake Probabilities) (2007). The Uniform California Earthquake Rupture Forecast, Version 2 (UCERF 2): *U.S. Geological Survey Open-File Report 2007-1437*, 95 p.

WGCEP (Working Group on California Earthquake Probabilities) (2002). Earthquake Probabilities in the San Francisco Bay Region: 2002–2031: *U.S. Geological Survey Open-File Report 03-214*.

WGCEP (Working Group on California Earthquake Probabilities) (1990). Probabilities of large earthquakes in the San Francisco Bay Region, California: *U.S. Geological Survey Circular*, p. 51.

Yu, E., and P. Segall (1996). Slip in the 1868 Hayward earthquake from the analysis of historical triangulation data, *J. Geophy. Res.*, **101**, 16101-16118.

CHAPTER III

Anderson , S., Ejarque, A., Brown, P.M., and Hallett, D.J., 2013, Holocene and historical vegetation change and fire history on the north-central coast of California, USA: The Holocene, v. 23, p. 1797 – 1810, doi:10.1177/0959683613505344

Biasi, G.P., Weldon, R.J., Fumal, T.E., and Sietz, G.P., 2002, Paleoseismic Event Dating and the Conditional Probability of Large Earthquakes on the Southern San Andreas Fault, California: Bulletin of the Seismological Society of America, v. 92, p. 2761-2781.

Biasi, G.P., and Weldon, R.J., 1994, Quantitative Refinement of Calibrated 14C Distributions: Quaternary Research, v. 41, p. 1-18.

Bronk Ramsey, C., van der Plicht, J., and Weninger, B., 2001, 'Wiggle matching' radiocarbon dates: Radiocarbon, v. 43, no. 3, p. 381-389.

Bronk Ramsey, C., 2009, Bayesian analysis of radiocarbon dates: *Radiocarbon, 51*, 1, p. 337-360.

Bronk Ramsey, C., 2013, OxCal Program, v.4.2: Radiocarbon Accelerator Unit, University of Oxford, Oxford, United Kingdom, https://c14.arch.ox.ac.uk/oxcal.html (last accessed 2 October, 2013).

Byrne, R., Reidy, L., Sengupta, D., Watson, B., Schmidt, D., Arthur, A., Kirby, M., Krause, J., Sullivan, J., Borokowski, J., Yiu, A., Menchaca, A., 2005, Recent (1850 - 2005) and Late Holocene (AD 400 – AD 1850) Sedimentation Rates at Bolinas Lagoon, Marin County, California: Report submitted to Marin County Open Space District, 36 p., California Coastal Records Project, www.Californiacoastline.org

Byrne, R. and Reidy, L., 2005, Recent Sedimentation Rates at Watsonville Slough, Santa Cruz County, California: Report submitted to The Watershed Institute, Earth Systems Science and Policy, California State University Monterey Bay, 26 p.

Fritz, E., 1940, Problems in dating rings of California Redwood: Tree-Ring Bulletin, v. 6, n. 3, p. 19 – 21.

Fumal, T.E., 2012, Timing of Large Earthquakes during the Past 500 Years along the Santa Cruz Mountains Segment of the San Andreas Fault at Mill Canyon, near Watsonville, California: Bulletin of Seismological Society of America, v. 102, doi:10.1785/0120110161.

Fumal, T.E., Heingartner, G.F., Samrad, L., Dawson, T.E., Hamilton, J.C., and Baldwin, J.N., 2003, Photomosaics and Logs of Trenches on the San Andreas Fault at Arano Flat near Watsonville, California: U.S. Geological Survey Open-File Report 03-450.

Fumal T.E., Rymer, M.J., and Sietz, G.G., 2002, Timing of Large Earthquakes since A.D. 800 on the San Andreas Fault Zone at Thousand Palms Oasis, near Palm Springs, California: Bulletin of the Seismological Society of America, v. 92, p. 2841-2860.

Hecker, S., Pantosti, D., Schwartz, D., Hamilton, J.C., Reidy, L.M., and Powers, T.J., 2005, The most recent large earthquake on the Rodgers Creek Fault, San Francisco Bay Area: Bulletin of the Seismological Society of America, v. 95, n. 3, p. 844-860.

Hendry, G. W., and Kelley, M. P., 1925, The Plant Content of Adobe Bricks, Formation and Processes of the Archaeobotanical Record: California Historical Society Quarterly, v. 4, p. 361-373.

Leinkaemper, J.J.,and Williams, 2007, A Record of Large Earthquakes on the Southern Hayward Fault for the Past 1800 Years: Bulletin of Seismological Society of America, v. 97, p. 1803-1819, doi:10.1785/0120060258.

Leinkaemper, J.J., Dawson, T.E., Personius, S.F., Seitz, G.G., Reidy, L.M., and Schwartz, D.P., 2002, A Record of Large Earthquakes on the Southern Hayward Fault for the Past 500 Years: Bulletin of Seismological Society of America, v. 92, p. 2637-2658.

Mensing S. and Byrne, R., .1998, Pre-mission invasion of Erodium cicutarium in California: Journal of Biogeography, v. 25, p. 757-762.

Plater, A.J., Boyle, J.F., Mayers, C., Turner, S.D., and Stroud, R.W., 2006, Climate and human impact on lowland lake sedimentation in Central Coastal California: The record from c. 650 AD to present: Regional Environmental Change, v. 6, p. 71-85.

Pybrum-Malmin, J., 1998, Corralitos: Second Ed., Corralitos, California, J.P. Malmin, 302 p.

Reidy, L.M., 2001, Evidence of Environmental change over the last 2000 years at Mountain Lake, in the northern San Francisco Peninsula, California [M.A. Thesis]: University of California, Berkeley, 108 p.

Reimer, P. J., Bard, E., Baillie, M. G. L., Bayliss, A., Beck, J. W., Blackwell, P. G., Bronk Ramsey, C., Buck, C. E., Cheng, H., Edwards, R. L., Friedrich, M., Grootes, P. M., Guilderson, T. P., Haflidason, H., Hajdas, I., Hatté, C., Heaton, T. J., Hoffmann, D., Hogg, A. G., Hughen, K. A., Kaiser, K. F., Kromer, B., Manning, Niu, M., S. W., Reimer, R. W., Richards, D. A., Scott, E.M., Southon, J. R., Staff, R.A., Turney, C. S. M., and van der Plicht, J., 2013, IntCal13 and Marine13 radiocarbon age calibration curves, 0-50,000 years cal BP: *Radiocarbon, v. 55*, n. 4, p. 1869-1887.

Scharer, K.M., Weldon, R.J., Fumal, T.E., and G.P. Biasi, 2007, Paleoearthquakes on the Southern San Andreas Fault, Wrightwood, California, 3000 to 1500 B.C.: A New Method for Evaluating Paleoseismic Evidence and Earthquake Horizons: Bulletin of the Seismological Society of America, v. 97, p. 1054-1093, doi:10.1785/0120060137.

Schwartz, D.P., Pantosti, D., Okumura, K., Powers, T., and Hamilton, J., 1998, Paleoseismic investigations in the Santa Cruz Mountains: Implications for the recurrence of large magnitude earthquakes on the San Andreas Fault: Journal of Geophysical Research, v. 103, p. 17,985-18,001.

Speer, J.H., 2010, Fundamentals of Tree-Ring Research: Tucson, The University of Arizona Press, 333 p.

Streig, A.R., Dawson, T.E., and Weldon, R.J., 2014, Paleoseismic Evidence of the 1890 and 1838 Earthquakes on the Santa Cruz Mountains Section of the San Andreas Fault, near Corralitos, California: Bulletin of the Seismological Society of America, v. 104, p. 285-300, doi: 10.1785/0120130009

CHAPTER IV

Akciz, S.O., Grant Ludwig, L., Arrowsmith, J R., Zielke, O., 2010. Century-long average time intervals between earthquake ruptures of the San Andreas fault in the Carrizo Plain, California. Geology 38, 787-790.

Crowell, J.C., 2003. Tectonics of Ridge Basin region, southern California. In: Crowell, J.C., (Ed.), Evolution of Ridge Basin, Southern California: An Interplay of Sedimentation and Tectonics. GSA Special Paper 367, 157-204.

Crowell, J.C., 1974. Sedimentation along the San Andreas fault, California. Dot, R.H., Shaver, R.H. eds., Modern and Ancient Geosynclinal Sedimentation. Society of Economic Paleontologists and Mineralogists Special Paper, 19, 292-303.

Crowell, J.C., 1952. Geology of the Lebec Quadrangle. California Division of Mines and Geology, Special Report 24, 23pp.

Duebendorfer, E.M., 1979. Geology of the Frazier Park-Cuddy Valley area, California. M.A. Thesis, University of California, Santa Barbara, 123pp.

Frankel, K.L., Dolan, J.F., Finkel, R.C., Owen, L.A., Hoeft, J.S., 2007. Spatial variations in slip rate along the Death Valley-Fish Lake Valley fault system determined from LiDAR topographic data and cosmogenic ^{10}BE geochronology. Geophysical Research Letters, 34, doi:10.1029/2007GL030549.

Guo, J., Zheng, J., Guan, B., Fu, B., Shi, P., Du, J., Xie, C., Liu, L., 2012. Coseismic Surface Rupture Structures Associated with 2010 Ms 7.1 Yushu Earthquake, China. Seismological Research Letters, 83, 109-118, doi:10.1785/gssrl.83.1.109.

Gurbuz, Alper, 2010. Geometric characteristics of pull-apart basins. Lithosphere, 2, 199-206.

Hecker, S.A., Abrahamson, N.A., Woodedell, K.E., 2013. Variability of Displacement at a Point: Implications for Earthquake-Size Distribution and Rupture Hazard on Faults. Bulletin of the Seismological Society of America, 103, 651-674.

Lindvall, S.C., Rockwell, T., Dawson, T., Helms, J., and Bowman, K.W., 2002. Evidence for Two SurfaceRuptures in the Past 500 Years on the San Andreas Fault at Frazier Mountain, California. Bulletin of the Seismological Society of America 92, 2689-2703.

Madden, C., Haddad, D.E., Salisbury, J.B., Zielke, O., Arrowsmith, J.R., Weldon, R.J.II, Colunga, J., 2013. Compilation of Slip-in-the-Last Event Data and Analysis of Last Event, Repeated Slip, and Average Displacement for Recent and Prehistoric Ruptures (UCERF3, Appendix R). U.S. Geological Survey Open-File Report 2013–1165-R, California Geological Survey Special Report 228-R, and Southern California Earthquake Center Publication 1792-R.

McClay, Ken and Tim Dooley, 1995. Analogue models of pull-apart basins. Geology, 23, 711714.

Mitra, Shankar and Debapriya Paul, 2011. Structural geometry and evolution of releasing and restraining bends: Insights from laser-scanned experimental models. AAPG Bulletin, 95, 1147-1180.

Onerdonk N.W., Rockwell, T.K., McGill, S.F., Marliyani, G.I., 2013. Evidence for Seven Surface Ruptures in the Past 1600 Years on the Claremont Fault at Mystic Lake, Northern San Jacinto Fault Zone, California. Bulletin of the Seismological Society of America, 103, 519-541, doi:10.1785/0120120060.

Olsen, R. S., 1988. Using the CPT for dynamic site response characterization. In: Von Thun, J. L. (Ed.), Earthquake Engineering and Soil Dynamics II—Recent Advances in Ground Motion Evaluation. American Society of Civil Engineers Geo-technical Special Publication 20, 374–388.

Scharer, K.M., Fumal, T.E., Weldon, R.J., Streig, A.R., 2014. Photomosaics and event evidence from the Frazier Mountain paleoseismic site, Trench 1, Cuts 1–4, San Andreas Fault Zone, Southern California (2007-2009). U.S. Geological Survey Open-File Report 20141002. 4 sheets, various scales, pamphlet 23 p., http://pubs.usgs.gov/of/2014/1002/.

Scharer, K.M., Weldon, R.J., Fumal, T.E., and Biasi, G.P., 2007. Paleoearthquakes on the southern SanAndreas fault, Wrightwood, CA 3000 to 1500 B.C.: a new method for evaluating paleoseismic evidence and earthquake horizons. Bulletin of the Seismological Society of America 97, 1054-1093.

Sieh, K.E., 1978. Prehistoric large earthquakes produced by slip on the San Andreas Fault at Pallett Creek, California. Journal of Geophysical Research, 83, 3907-3938.

Sylvester, Arthur, 1988. Strike-slip faults. Geological Society of America Bull., 100, 1666-1703.

Weldon, R.J., Fumal, T.E., Powers, T.J., Pezzopane, S.K., Scharer, K.M., and Hamilton, J.C., 2002. Structure and Earthquake Offsets on the San Andreas Fault at the Wrightwood, California, Paleoseismic Site. Bulletin of the Seismological Society of America, 92, 2704-2725.

Wu, J.E., McClay, K., Whitehouse, P., and T. Dooley, 2009. 4D analogue modeling of transtensional pull-apart basins. Marine and Petroleum Geology, 26, 1608-1623.

CHAPTER V

Biasi, G.P., Weldon, R.J., Dawson, T.E., 2013. Distribution of Slip in Ruptures (UCERF3, Appendix F), U.S. Geological Survey Open-File Report 2013–1165-R, California Geological Survey Special Report 228-R, and Southern California Earthquake Center Publication 1792-R.

King, G.C., Wesnousky, S.G., 2007. Scaling of Fault Parameters for Continental Strike-Slip Earthquakes. Bulletin of the Seismological Society of America, 97, pp.1833-1840, doi: 10.1785/0120070048.

Scharer, K.M., Fumal, T.E., Weldon, R.J., Streig, A.R., 2014. Photomosaics and event evidence from the Frazier Mountain paleoseismic site, Trench 1, Cuts 1–4, San Andreas Fault Zone, Southern California (2007-2009). U.S. Geological Survey Open-File Report 20141002. 4 sheets, various scales, pamphlet 23 p., http://pubs.usgs.gov/of/2014/1002/.

Scholz, C.H., 2008. The Mechanics of Earthquakes and Faulting. Cambridge University Press, 2002, Second Edition, 471 p.

Schwartz, D.P., Coppersmith, K.J.,1984. Fault Behavior and Characteristic Earthquakes: Examples From the Wasatch and San Andreas Fault Zones. Journal of Geophysical Research, 89, 5681-5698.

Sieh, K.E., 1978. Prehistoric large earthquakes produced by slip on the San Andreas Fault at Pallett Creek, California. Journal of Geophysical Research, 83, 3907-3938.

Sieh, K.E.,1981. A review of geological evidence for recurrence times of large earthquakes. In Earthquake Prediction: an International Review, eds. D. Simpson and P.G. Richards. Washington, DC: American Geophysical Union, pp. 209-216.

Madden, C., Haddad, D.E., Salisbury, J.B., Zielke, O., Arrowsmith, J.R., Weldon, R.J.II, Colunga, J., 2013. Compilation of Slip-in-the-Last Event Data and Analysis of Last Event, Repeated Slip, and Average Displacement for Recent and Prehistoric Ruptures (UCERF3, Appendix R). U.S. Geological Survey Open-File Report 2013–1165-R, California Geological Survey Special Report 228-R, and Southern California Earthquake Center Publication 1792-R.